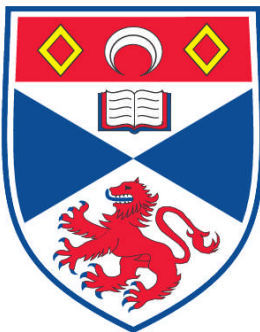


**SOLID OXIDE STEAM ELECTROLYSIS FOR HIGH
TEMPERATURE HYDROGEN PRODUCTION**

Kelcey L. Eccleston

**A Thesis Submitted for the Degree of PhD
at the
University of St. Andrews**



2007

**Full metadata for this item is available in
Research@StAndrews:FullText
at:
<http://research-repository.st-andrews.ac.uk/>**

**Please use this identifier to cite or link to this item:
<http://hdl.handle.net/10023/322>**

This item is protected by original copyright

**This item is licensed under a
Creative Commons License**

Solid Oxide Steam Electrolysis for High Temperature Hydrogen Production

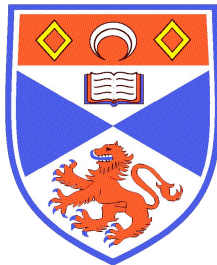
A thesis submitted for the degree of Ph.D.

by

Kelcey Lynne Eccleston

University of St. Andrews

Supervised by Prof. John T. S. Irvine



Submitted July 2006

Declarations

I, Kelcey Lynne Eccleston, hereby certify that this thesis, which is approximately.....words in length, has been written by me, that it is the record of work carried out by me and that it has not been submitted in any previous application for a higher degree.

Date signature of candidate

I was admitted as a research student in October 2002 and as a candidate for the degree of Ph.D in October 2003; the higher study for which this is a record was carried out in the University of St Andrews between 2002 and 2005.

Date signature of candidate

I hereby certify that the candidate has fulfilled the conditions of the Resolution and Regulations appropriate for the degree of Doctor of Philosophy in the University of St Andrews and that the candidate is qualified to submit this thesis in application for that degree.

Date signature of supervisor

In submitting this thesis to the University of St Andrews, I understand that I am giving permission for it to be available for use in accordance with the regulations of the University Library for the time being in force, subject to any copyright vested in the work not being affected thereby. I also understand that the title and abstract will be published, and that a copy of the work may be made and supplied by any bona fide library or research worker.

Date signature of candidate

Acknowledgements

This work is dedicated to Luis, *mi amor*, nothing is harder than having you heart 4,406 miles away, but without you there waiting for me I never would have made it. To my parents whose love and support has made this all possible, not to mention the power my mom's the liquid-cooled red pen To Eric, the Big B., whose brotherly advice on life, the universe, and engineering is always welcome.

Sincere thanks go to my supervisor, John Irvine, who gave me the opportunity to work with him. His help, encouragement and understanding kept me going while so far from home. A special thanks goes to George Anthony, Sylvia Williamson, Bobby Cathcart, Ross Blacklely, Brian Walker and Colin Smith for their technical advice and help.

To all of the JTSI group, past and present, my fellow sardines have always made life more interesting if nothing else. Special thanks go to Angela Kruth for her help with all things electrolysis; Fran Jones, the tape casting wizard, for help with tapes, tubes, and just about everything; Julie Nairn, for far too many things to list on just one page; Cristian Savaniu for help with sol-gel powders; Maarten Verbraeken, for AC impedance tips; and Paul Connor for buying a car that could withstand his unique driving skills. Also to the JTSI pub quiz team, for the beers and the laughs.

Thanks to my friends here in St Andrews, especially Juliet, Rachel and Fran, because there is nothing in life that can't be fixed with a bottle of wine and a good (or bad) movie. Thanks, also to the gang back in Golden and Friday nights at the GCB.

ABSTRACT

This study has focused on solid oxide electrolyser cells for high temperature steam electrolysis. Solid oxide electrolysis is the reverse operation of solid oxide fuel cells (SOFC), so many of the same component materials may be used. However, other electrode materials are of interest to improve performance and efficiency.

In this work anode materials were investigated for use in solid oxide electrolysers. Perovskite materials of the form $L_{1-x}Sr_xMO_3$, where M is Mn, Co, or Fe. LSM is a well understood electrode material for the SOFC. Under electrolysis operation LSM performed well and no interface reactions were observed between the anode and YSZ electrolyte. LSM has a relatively low conductivity and the electrode reaction is limited to the triple phase boundary regions. Mixed ionic-electronic conductors of LSCo and LSF were investigated, with these materials the anode reaction is not limited to triple phase boundaries. The LSCo anode had adherence problems in the electrolysis cells due to the thermal expansion coefficient mismatch with the YSZ electrolyte. The LSCo reacted with the YSZ at the anode/electrolyte interface forming insulating zirconate phases. Due to these issues the LSCo anode cells performed the poorest of the three. The performance of electrolysis cells with LSF anode exceeded both LSM and LSCo, particularly under steam operation, although an interface reaction between the LSF anode and YSZ electrolyte was observed.

In addition to the anode material studies this work included the development of solid oxide electrolyser tubes from tape cast precursor materials. Tape casting is a cheap processing method, which allows for co-firing of all ceramic components. The design development resulted in a solid design, which can be fabricated reliably, and balances strength with performance. The design used LSM anode, YSZ electrolyte, and Ni-YSZ cathode materials but could easily be adapted for the use of other component materials. Proper sintering rates, cathode tape formulation, tube length, tape thickness, and electrolyte thickness were factors explored in this work to improve the electrolyser tubes.

Table of Contents

Chapter 1: Introduction

1.1 Hydrogen.....	3
1.1.1 History.....	3
1.1.2 Hydrogen economy	4
1.1.3 Hydrogen fuel.....	5
1.1.4 Hydrogen safety	6
1.2 Hydrogen Production	10
1.2.1 Fossil fuels	12
1.2.1.1 Steam reforming.....	12
1.2.1.2 Partial oxidation of heavy hydrocarbons.....	12
1.2.1.3 Gasification of coal	13
1.2.2 Biomass.....	13
1.2.2.1 Steam gasification of biomass.....	13
1.2.2.2 Fermentation of biomass.....	14
1.2.2.3 Biological production.....	14
1.2.3 Electrochemical.....	14
1.2.3.1 Photoelectrolysis	14
1.2.3.2 Thermochemical water splitting.....	15
1.3 Electrolysis	15
1.3.1 Alkaline water electrolysis	17
1.3.2 Proton exchange membrane water electrolysis	18
1.3.3 Advantages and Disadvantages of conventional electrolyzers.....	19
References	20

Chapter 2: Solid Oxide Steam Electrolysis Background and Theory

2.1 Solid oxide steam electrolysis	25
2.1.1 Thermodynamics of electrolysis	27
2.1.2 Equilibrium Nernst potential.....	28
2.1.3 Operating cell polarisation	29
2.1.3.1 Ohmic losses	30
2.1.3.2 Concentration polarisation	30
2.1.3.3 Activation polarisation	31
2.1.4 Electrolysis efficiency	32
2.2 Component materials.....	32
2.2.1 Electrolyte	33
2.2.2 Cathode	33
2.2.3 Anode	33

2.3 Previous work	34
2.3.1 Hot Elly	34
2.3.2 Westinghouse electrolyser	36
2.3.3 INEEL Electrolyser	36
2.3.4 JAERI high temperature electrolyser system	37
2.3.5 Natural gas assisted electrolyser	38
2.3.6 Proton conductor electrolyser	39
2.3.6.1 Proton conductor background	40
2.3.6.2 Solid Protonic Steam Electrolysis.....	41
References	43

Chapter 3: Experimental

3.1 Materials Synthesis and Processing.....	47
3.1.1 Solid State Powder Preparation.....	47
3.1.2 Sol Gel Synthesis	47
3.1.3 Pellet Preparation	50
3.1.4 Screen Printing	50
3.1.5 Spin-coating	52
3.1.6 Tape Casting	52
3.1.7 Electrolysis Tube Fabrication	55
3.2 Electrochemical Testing.....	57
3.2.1 Electrolysis pellet cell testing.....	57
3.2.2 Electrolysis tube cell testing	59
3.2.3 Oxygen sensor	61
3.3 AC Impedance Spectroscopy	62
3.3.1 Theory	63
3.3.2 Equivalent circuits.....	65
3.4 Electron Microscopy	68
3.4.1 Scanning Electron Microscopy (SEM)	68
3.4.2 Electron Dispersive Spectroscopy (EDS)	71
3.4.3 Characteristic X-Ray Spectrum.....	71
3.4.4 Bragg's Law	75
3.4.5 Sample preparation.....	77
3.5 X-Ray Diffraction.....	78
3.5.1 Powder Diffraction.....	78
3.5.2 Sample Preparation	79
3.6 Dilatometry	79
References	81

Chapter 4: Anode Material Studies

4.1 Electrolyser Anode Materials.....	87
4.1.1 Introduction	87
4.1.2 Structure of anode materials.....	88

4.2 SEM and EDS Materials Analysis.....	91
4.2.1 LSM	91
4.2.2 LSCo	93
4.2.3 Ceria interlayer.....	99
4.2.4 LSF.....	101
5.1 Electrolysis Performance.....	103
5.1.1 Electrolysis testing	103
5.1.2 AC impedance	105
5.2 LSM anode.....	106
5.3 LSCo anode.....	110
5.4 LSF anode	114
5.5 Anode material comparison	120
References	124

Chapter 5: Electrolyser Tube Development

5.1 Introduction	129
5.1.1 Closed-end tape cast electrolysis tubes	129
5.2 Tube Development	131
5.2.1 SEM characterisation	131
5.2.2 Initial tube configuration.....	134
5.2.3 Tube flaws.....	134
5.2.4 Cathode formulation.....	136
5.2.5 Sinter rate	136
5.2.6 Thin tapes	137
5.2.7 Electrolyte thickness	139
5.2.8 Tube length	140
5.2.9 Isostatic pressing	141
5.3 Manganese Deficiency.....	142
5.4 Dilatometry	146
5.1 Electrolysis Testing	148
5.2 Performance of Electrolysis Tubes.....	151
5.3 Tube Comparison.....	153
References	156

Chapter 6: Discussion.....	157
Chapter 7: Conclusions	163
Chapter 8: Future Work	167

Chapter 1: Introduction

1.1 Hydrogen.....	3
1.1.1 History	3
1.1.2 Hydrogen economy	4
1.1.3 Hydrogen fuel	5
1.1.4 Hydrogen safety	6
1.2 Hydrogen Production.....	10
1.2.1 Fossil fuels	12
1.2.1.1 Steam reforming	12
1.2.1.2 Partial oxidation of heavy hydrocarbons	12
1.2.1.3 Gasification of coal	13
1.2.2 Biomass.....	13
1.2.2.1 Steam gasification of biomass	13
1.2.2.2 Fermentation of biomass	14
1.2.2.3 Biological production.....	14
1.2.3 Electrochemical.....	14
1.2.3.1 Photoelectrolysis	14
1.2.3.2 Thermochemical water splitting.....	15
1.3 Electrolysis	15
1.3.1 Alkaline water electrolysis.....	17
1.3.2 Proton exchange membrane water electrolysis	18
1.3.3 Advantages and Disadvantages of conventional electrolyzers	19
References	20

1.1 Hydrogen

1.1.1 History

The Renaissance alchemist Paracelsus (1493-1541) is credited with the discovery of hydrogen. He observed a flammable gas produced when dilute acids reacted with metals. Henry Cavendish (1731-1810) is given credit for recognising hydrogen as an element in 1766. Cavendish described it as "inflammable air from metals". He accurately described many properties of hydrogen but thought that the gas originated from the metal rather than from the acid. Antoine Lavoisier (1743-1794) proved that water was made of hydrogen and oxygen and named hydrogen from the Greek words *hydros* (water) and *gennao* (procreate). ^[1]

The English scientists William Nicholson and Sir Anthony Carlisle discovered that hydrogen and oxygen gases are produced when an electric current is applied to water—the process of electrolysis. In 1845, working from earlier experiments of Christian Schoenbein, Sir William Robert Grove carried out experiments on the reverse of electrolysis, generating electricity from the reaction of oxygen with hydrogen. In his experiments, he sealed platinum electrodes in separate bottles containing hydrogen and oxygen, respectively. When the containers were immersed in dilute sulphuric acid, a current flowed between the two electrodes, and water was formed in the gas bottles. Grove linked several of these devices in series to increase the voltage produced and named the device a *gas battery*^[2]. Later, chemists Ludwig Mond and Charles Langer, who conducted similar experiments, referred to the system a *fuel cell*. From 1932-1959, Dr Francis Thomas Bacon made improvements on the fuel cell designs of Mond and Langer by replacing the expensive platinum electrodes with nickel gauze and replacing the sulphuric acid electrolyte with potassium hydroxide. This *Bacon Cell* was the first alkaline fuel cell. By 1959, the Bacon Cell had been improved such that it could produce 5 kW of power. The first fuel cell powered vehicle was demonstrated shortly after. ^[1,3,4]

1.1.2 Hydrogen economy

In 1923, J.B.S. Haldane introduced the concept of renewable hydrogen. Haldane stated that if hydrogen derived from wind power via electrolysis were liquefied and stored it would be the ideal fuel of the future.^[5]

The depletion of fossil fuel resources and the need to reduce climate-affecting emissions (also known as green house gases) has driven the search for alternative energy sources. Hydrogen is a leading candidate as an alternative to hydrocarbon fossil fuels. Hydrogen can have the advantages of renewable production from carbon-free sources, which result in emission levels far below existing emission standards. Hydrogen can be derived from a diverse range of sources offering a variety of production methods best suited to a particular area or situation.^[6]

Hydrogen has long been used as a fuel. The gas supply in the early part of the 20th century consisted almost entirely of a coal gas comprised of more than 50% hydrogen, along with methane, carbon monoxide, and carbon dioxide, known as “town gas”. Town gas was eventually replaced by oil and natural gas but is still used safely in some parts of the world. The unique properties of hydrogen fuel led to its use providing lift for early dirigibles and later as a propellant for spacecraft.

Hydrogen is an energy carrier like electricity or gasoline, and it has potential for energy storage and transportation and as a fuel for electricity generation and powering motor vehicles. Hydrogen is a high-quality form of energy that can be readily converted to electricity and back again to hydrogen

Hydrogen can either be burned as a fuel in a combustion engine or electrochemically converted to electricity directly in fuel cells. Burning hydrogen is not particularly energy efficient because much of the energy is lost as heat. The key benefits of hydrogen-powered fuel cells are the high efficiency, particularly when used as part of a combined heat and power system, little to no emissions of pollutants and greenhouse gases, low operating noise, and the potential for application in distributed electricity generation. An

illustration of the possible hydrogen economy scheme, including primary energy source, production, storage and end use, is presented in Figure 1.1.

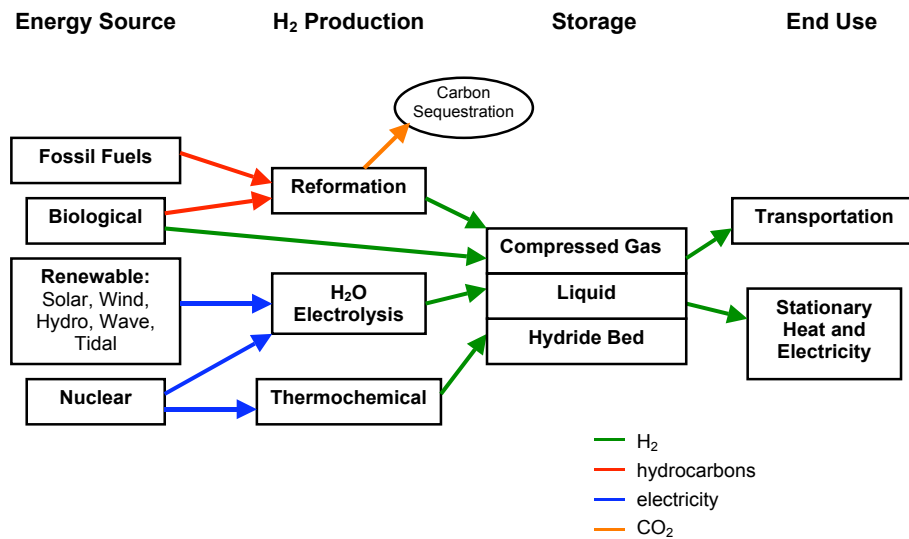


Figure 1.1: Hydrogen economy scheme

1.1.3 Hydrogen fuel

Hydrogen differs from other fuels in many important aspects. Hydrogen has a density of 0.089 g/l. This is 14 times less dense than air, which has a density of 1.19 g/l. Liquid hydrogen has a density of 70.99 g/l. Hydrogen has the highest energy to weight ratio of any fuel. A single kilogram of hydrogen contains the same amount of energy as 2.1 kg of methane or 2.8 kg of gasoline. Due to its low density, however, hydrogen has a poor energy to volume ratio, about 1/3 of that for methane. The energy densities of several energy carriers can be seen in Table 1.1.

Table 1.1: Energy Densities for Energy Carriers

Energy carrier	Form of Storage	Energy density	
		by weight (kWh/kg)	by volume (kWh/l)
Hydrogen	gas (20 MPa)	33.3	0.53
	liquid (-253 °C)	33.3	2.36
	metal hydride	0.58	3.18
Methane	gas (20 MPa)	13.9	2.58
	liquid (-162 °C)	13.9	5.8
Propane	liquid	12.9	7.5
Methanol	liquid	5.6	4.42
Gasoline	liquid	12.7	8.76
Diesel	liquid	11.6	9.7
Electricity	Pb battery (chemical)	0.03	0.09
	Li-ion battery	0.15-0.2	0.25-0.53

Adapted from Zittel and Wurster.^[7]

The energy content of fuel gases is expressed as higher heating value (HHV) or lower heating value (LHV). The HHV measures the energy per unit volume of gas completely combusted, where the water produced condenses to a liquid. The LHV is the energy per unit volume of gas completely combusted, where the water remains as a vapour. Condensation releases energy, so the LHV is lower than the HHV. For most fuel the difference is minor; but in the case of hydrogen, the difference is almost 16%. This is significant because fuel cells can capture only the LHV value of hydrogen.

1.1.4 Hydrogen safety

Hydrogen is routinely transported safely both in liquid and compressed gaseous form by rail, barge, truck, and pipeline for use in the aerospace, food, petrochemical, and semiconductor industries. These industries have an excellent safety record with regard to hydrogen. Understanding the specific risks associated with hydrogen fuel is the key to safe use and transport. All fuels are dangerous under certain conditions; hydrogen is no exception. Due to its unique physical properties, the hazards associated with hydrogen are markedly different to those of hydrocarbon fuels. Some of these differences provide safety benefits when compared to other fuels. Hydrogen can be less hazardous than

conventional fuels in some situations and more hazardous in other situations. When considering the safety of hydrogen in relation to other fuels the particular circumstances of its accidental release must be evaluated carefully. The combustion properties of hydrogen and various other fuels are listed in Table 1.2.

Table 1.2: Combustion Properties of Fuel Gases

		Hydrogen (H ₂)	Methane (CH ₄)	Propane (C ₃ H ₈)	Gasoline (C ₄ to C ₁₂)
Lower heating value	MJ/kg	120	50	46.4	44.5
	kWh/kg	33.33	13.90	12.88	12.36
Higher heating value	MJ/kg	142	55.5	50.4	47.4
	kWh/kg	39.41	15.42	14.00	13.16
Density	kg/m ³	0.08988	0.7175	2.011	
Gas constant	J/kgK	4124	518.8	188.5	
Diffusion coefficient in air	cm ² /s	0.61	0.16	0.12	0.05
Self ignition temperature	°C	585	537	487	228-471
Ignition temp. in air	°C	530	645	510	280
Ignition limit in air	vol-%				
Lower limit		4.1	5.1	2.1	1.4
Upper limit		72.5	15	9.5	7.8
Maximum flame velocity	cm/s	346	43	47	40
Detonation limit	vol-%				
Lower limit		11-18	6.3	3.1	1.1
Upper limit		59	13.5	7	3.3
Minimum ignition energy	mJ (mWs)	0.02	0.29	0.26	0.24
Stoichiometric air/fuel ratio	vol-%	27.2	17.2	15.6	14.6
Flame temp. in air	°C	2045	1885	1922	2197
Thermal energy radiated from flames *	%	5-10	10-33	10-50	10-50

*For hydrocarbon flames the majority of radiation is due to soot formation and emission and is therefore highly dependent on the combustion efficiency. The values quoted cover the range of combustion efficiencies. Adapted from Zittel and Wurster^[7] Adamson et al^[8] and from Alcock et al.^[9]

To ignite hydrogen an ignition source and the proper amount of oxidizer must be present. The density, diffusivity, and small molecular size of hydrogen make it difficult to contain a combustible situation. Hydrogen is about 14 times less dense than air; natural gas is only 1.7 times less dense. Hydrogen rapidly diffuses in air, about 4 times faster than methane and 12 times faster than gasoline fumes. As a result, leaking hydrogen rapidly dissipates away from the source of the leak and quickly disperses to concentrations below the ignition limit. This means that in general the flammable hazard for hydrogen is of a

shorter duration. The only exception is in cryogenic leaks of hydrogen in which the extremely cold vapour cloud initially formed can be denser than the surrounding air.

The hydrogen ignition limit in air, also called the flammability range, is much wider than that of methane or gasoline fumes. This means that hydrogen will ignite over a wider range of concentrations in air. However, the lower ignition limits of hydrogen and methane are very similar, and those of propane and gasoline are even lower. In many situations, the lower limit is more important because ignition sources are often already present in fuel-air mixtures once a flammable concentration has been reached. Also, in some circumstances the dispersion characteristics of hydrogen make it less likely that a flammable mixture will form than for methane, propane, or gasoline. Furthermore, a significantly richer mixture of hydrogen will burn, which means that cloud of hydrogen will be consumed quicker than a methane cloud of similar concentration.

The minimum ignition energy of hydrogen is an order of magnitude less than that of the other fuels. However, this may not be as significant as it seems. The minimum ignition energy for fuel/air mixtures is usually at or near a stoichiometric composition, which is 29 vol.% for hydrogen. At the lower ignition limit for hydrogen the ignition energy is similar to that of methane, approximately 10 mJ, as shown in Figure 1.2. An electrostatic spark often occurs at a higher energy than is required to ignite methane, propane, or gasoline.

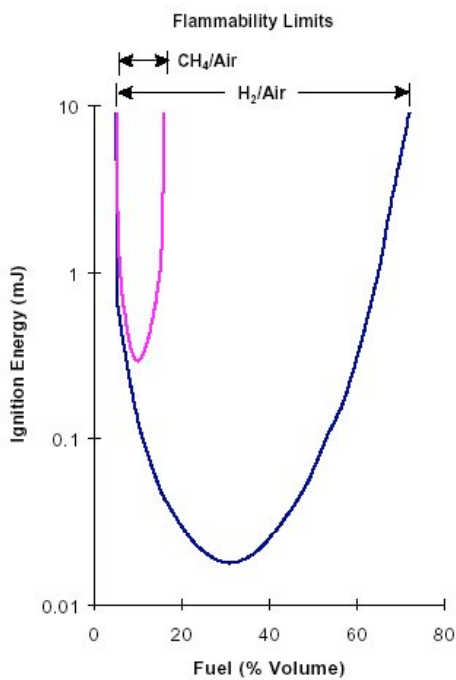


Figure 1.2 Flammability limits for hydrogen and methane ^[10]

The large difference in lower ignition limit, 4%, and the lower detonation limit, 18% for hydrogen, means that it is far more likely to burn than to explode. This is not necessarily the case for the other fuels whose lower ignition and detonation limits are quite similar. Although its detonation limits are large, it is difficult to ignite hydrogen in air if it is unconfined. A hydrogen explosion usually requires turbulence and a restricted volume, such as an enclosed area or a tube.

Hydrogen flames are smokeless, with little to no soot formation, and almost invisible. The flame itself can have temperature of over 2000 °C, but a hydrogen flame emits only one-tenth the radiant heat of a hydrocarbon fire. This is due to the presence of water vapour created by combustion of hydrogen and the absence of carbon.

1.2 Hydrogen Production

Although hydrogen is the most abundant element in nature, it is almost exclusively found as a compound with other elements. Before hydrogen can be used as a fuel it must first be released from these compounds. Hydrogen production always requires energy and can be

segregated into two categories: those using a primary energy carrier and those using a secondary energy carrier. Primary energy production is at present limited to hydrogen production from fossil fuels. Other processes currently under development include reforming and pyrolysis using biomass and other carbon waste, as well as direct methanol reforming. The only secondary energy carrier used to produce hydrogen is electricity, specifically by the electrolysis of water. Hydrogen is also produced as a by-product in the chlorine-alkaline electrolysis process.

Hydrogen has been produced on an industrial scale for more than 100 years. Modern hydrogen production is closely tied to the oil and chemical industries. Hydrogen is used in petroleum refineries to convert crude oil into useful fuels such as diesel and gasoline. Hydrogen is used in chemical plants in the manufacture of ammonia (NH_3) and other nitrogen based fertilizers. Nearly all of the world's hydrogen supply is produced from fossil fuels, most of which is produced by steam reforming of natural gas. Annual global production of hydrogen is about 45 billion kilograms (kg) or 500 billion normal cubic meters (Nm^3). A normal cubic meter refers to one cubic meter at one atmosphere and 0 °C. Table 1.3 shows the annual amount of hydrogen produced worldwide by the various methods.

Table 1.3: Global Hydrogen Production

Origin	Amount (billions of Nm^3/year)	Percent
Natural gas	240	48
Oil	150	30
Coal	90	18
Electrolysis	20	4
Total	500	100

Source United States Department of Energy [11]

1.2.1 Fossil fuels

1.2.1.1 Steam reforming

Most of the present industrial-scale hydrogen production uses the process of steam reforming. Steam reforming is an endothermic, catalytic conversion of light hydrocarbons, such as methane, with water vapour. Steam reforming uses thermal energy to help separate hydrogen from the carbon components in methane and involves the reaction of the fuel with steam on catalytic surfaces. The first step in the reaction decomposes the fuel into hydrogen and carbon monoxide (1.1) usually at temperatures between 750-1000 °C and pressures on the order of 2.5 MPa. The catalyst in the reaction is typically nickel. The general reaction is expressed as:



and specifically for methane:



The second step in the process is a shift reaction of the carbon monoxide and water that produces carbon dioxide and hydrogen (1.3). This reaction is generally carried out at temperatures between 200-475 °C.



The gas leaving the shift reactor is roughly 80% hydrogen, with CO₂, CH₄, CO, and water vapour. The carbon dioxide is removed from the gas mixture by absorption or membrane separation. The gas is then further cleaned to remove the other components, leaving pure hydrogen. The residual components cleaned from the hydrogen still contain some combustible gases, and are recycled back into the reformer along with the primary gas (CH₄) [12].

1.2.1.2 Partial oxidation of heavy hydrocarbons

Heavy hydrocarbons, such as crude oil, have a low volatility and often a high sulphur content. This prevents the use of steam reforming for hydrogen production. Instead, the oil is treated in a combustion reactor fed with steam and oxygen at temperatures between 1300-1500 °C. The oxygen to steam ratio is controlled so that the gasification continues without the use of additional energy. This process is often called gasification. There is no

simple chemical formula for crude oil, because it is made up of various heavy hydrocarbons; however, the net reaction for the partial oxidation reaction can be represented as follows:



This reaction is then followed by the shift reaction, (1.3) to further oxidize the CO and produce more hydrogen.^[13]

1.2.1.3 Gasification of coal

Gasification of coal is the oldest hydrogen production method. Of all fossil fuels coal has the lowest hydrogen to carbon ratio, thus more CO₂ is produced per mole of H₂. With coal gasification, however, high purity hydrogen can be produced with low emissions with CO₂ separation and capture. Generally, coal is heated to 900 °C with a catalyser in the absence of air. A more advanced method of gasifying coal uses a similar technique to achieve partial oxidation of coal using steam and oxygen at temperatures over 1400 °C. The coal must first be ground to a fine powder and mixed with water to produce a 50–75% solid content suspension, which is fed into the reactor. This process results in H₂, CO, and CO₂, and some sulphur and nitrogen.^[14,15,16]

1.2.2 Biomass

Hydrogen production from biomass can be separated into several categories. The primary methods include production by steam gasification of solid biomass, fermentation of liquid waste, and biological hydrogen production.

1.2.2.1 Steam gasification of biomass

Hydrogen can be produced by thermal gasification of biomass. Solid biomass can be produced from a variety of sources: pellets derived from dedicated energy crops, forestry waste products, straw, or solid organic waste. In the first stage, known as pyrolysis, the solid biomass is heated and broken down into coke, condensates, and gasses. In the second stage, the products are combined with oxygen and steam. The resulting gas consists mainly of H₂, CO, and CH₄. Steam is then applied to reform the methane into hydrogen and CO. The CO is then recycled into the process to increase the yield of hydrogen.^[17]

1.2.2.2 Fermentation of biomass

This process uses high moisture content biomass or liquid manure. A gas, termed biogas, is produced via methane fermentation. Biogas is composed primarily of CO and CH₄; a small amount of H₂ is produced during the fermentation. The biogas can then be processed further, via steam reforming, to extract the H₂ or used directly in fuel cells that allow for internal reforming, such as molten carbonate or solid oxide fuel cells.^[18]

1.2.2.3 Biological production

Blue-green algae, green algae, and some bacteria can be used for the production of hydrogen. Biological electrolysis is the first step in photosynthesis, where enzymes use sunlight to break water down into hydrogen and oxygen. In most plants, the hydrogen is then combined with carbon dioxide to form carbohydrate. Certain microorganisms, however, release hydrogen instead of carbohydrate under photosynthesis. The yield and efficiency for biological production is low, but further genetic research is currently being conducted to improve the process.^[19,20]

1.2.3 Electrochemical

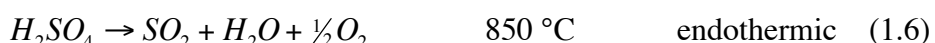
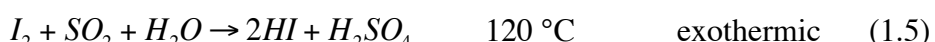
There are several hydrogen production methods that can be categorized generally as electrochemical processes. Photoelectrochemical hydrogen production (also known as photoelectrolysis), thermochemical water splitting, and water electrolysis are the main processes. Of these, only water electrolysis is currently commercially available.

1.2.3.1 Photoelectrolysis

Photoelectrolysis of water uses sunlight to directly split water into hydrogen and oxygen. The process requires a photosensitive semiconductor device, similar to a photovoltaic solar cell, in conjunction with water-splitting catalysts. The wet semiconductor surface absorbs solar energy and acts as an electrode for dissociation of water. This technique eliminates the need for separate power generation and electrolysis systems; however, the yield and efficiency are quite low.^[21,22]

1.2.3.2 Thermochemical water splitting

Thermochemical water splitting is the conversion of water into hydrogen and oxygen by a series of chemical reactions. Energy, as heat, is input to a thermochemical cycle via one or more high-temperature endothermic reactions. Excess heat is given off via one or more low temperature exothermic reactions. Water must be injected to maintain the reactions; all the other reactants are regenerated and recycled. The sulphur-iodine system is an example of a thermochemical cycle. It consists of three chemical reactions (1.5), (1.6), and (1.7), with the net reaction (1.8) the dissociation of water.



Sulphuric acid and hydrogen iodide are formed in the exothermic reaction of H_2O , SO_2 and I_2 (1.5). The sulphuric acid is dissociated in reaction (1.6), which consumes the greatest part of the heat input. The hydrogen is generated in the decomposition of hydrogen iodide (1.8). Since hydrogen and oxygen are derived in different steps, the need for high-temperature gas separation is eliminated.^[23]

1.3 Electrolysis

Hydrogen production by the electrolytic decomposition of water is simple, reliable, clean, and produces high purity hydrogen. First demonstrated by Nicholson and Carlisle in 1800, electrolysis was not used commercially to produce hydrogen from water until 1902 by the Oerlikon Engineering Company. In the 1930's electrolyzers developed from filter-press operations to large tank-type electrolyzers. By the 1950's pressurised electrolyzers were developed. The next major advancements have been the development of new solid electrode materials, both polymer and solid oxide.^[24]

Electrolysis is an electrochemical process in which electrical energy is the driving force for the dissociation of water. Electrolysis separates the water into its constituent elements, hydrogen, and oxygen. The electric current causes the positively charged hydrogen ions

to migrate to the negatively charged cathode, where a reduction reaction takes place to form hydrogen gas. Simultaneously the oxygen ions migrate to the positively charged anode, where an oxidation reaction forms oxygen gas. The water decomposition takes place in two partial reactions at two electrodes, which are separated by an ion-conducting electrolyte.^[25] The different types of electrolysis are characterised by the electrolyte used, for example, aqueous alkaline, polymer membranes, or solid oxide electrolytes. The three types of electrolyzers are summarised in

Table 1.4. A voltage of 1.24 volts is necessary to separate hydrogen from oxygen in pure water at 25 °C and 1.03 kg/cm² pressure. This voltage requirement increases or decreases with changes in temperature and pressure.^[26]

Table 1.4: Comparison of three types of water electrolyzers

	Alkaline	Solid polymer	High temperature solid oxide
Electrolyte	KOH	polymer membrane	solid oxide
Charge carrier(s)	OH ⁻ , K ⁺	H ⁺	O ²⁻
H₂O input	high purity water	high purity water	steam
Temperature (°C)	80	100	800-900

Because hydrogen generated by electrolysis uses electric power this process is generally only economically viable in those regions of the world where electric power can be generated very cheaply. This is currently the case almost exclusively in large-scale hydroelectric plants, for example in Egypt, Iceland, and Norway. This process also holds potential for use in areas where it could be combined with other forms of renewable energy. A combined fuel cell/ electrolyser system coupled with wind or wave power could help eliminate the problems associated with the intermittency of these renewable energy sources.

Making hydrogen from water by electrolysis is the most energy-intensive way to produce the fuel. However, it is also a clean process provided the electricity comes from a clean source. Less energy is needed to convert a hydrogen-rich energy carrier like methane (CH₄) or methanol (CH₃OH) into hydrogen by steam reforming, but the energy invested

always exceeds the energy contained in the hydrogen. Efficient and economical electrolysis of water to hydrogen and oxygen gases is of significant importance to renewable hydrogen energy programs. In addition, fuel cell/electrolyser systems offer the potential for efficient energy storage and conversion.

1.3.1 Alkaline water electrolysis

Alkaline electrolysis has been in commercial use for over 80 years, mainly in conjunction with hydropower. This process employs an aqueous alkaline electrolyte, such as potassium hydroxide (KOH), at low pressures between 0.2-0.5 MPa. It is important to use inert electrical conductors for the electrodes to prevent unwanted reactions. Cathode materials are usually a low-carbon steel of the type SAE 1020. The anode is commonly a so-called dimensionally stable alloy, of titanium with a metal oxide active layer. A micro-porous ion-conducting diaphragm separates the cathode and anode chambers. This diaphragm prevents mixing of the oxygen and hydrogen product gases. A schematic of the alkaline electrolysis cell is shown in Figure 1.3

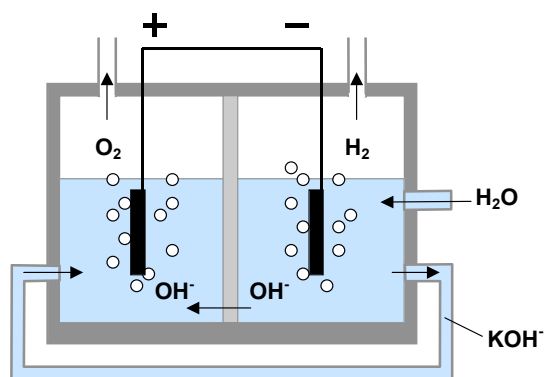


Figure 1.3: Alkaline electrolysis process

Two water molecules are reduced to one molecule of hydrogen and two hydroxyl ions at the cathode (1.9). Two hydrogen ions recombine as hydrogen gas and escape from the surface of the cathode. The hydroxyl ions migrate under the influence of the electrical field between the cathode and anode through the porous diaphragm to the anode, where they are discharged to 1/2 molecule of oxygen and one molecule of water. (1.10) The

oxygen recombines at the anode surface and escapes as a gas. The energy for this process is supplied by electricity alone.



Improvements on the alkaline electrolysis process have led to high-pressure electrolyzers. High-pressure electrolysis allows production of hydrogen at output pressures up to 5 MPa. These electrolyzers have an improved performance and allow for a fluctuating current supply as is typical with wind or wave power.^[27]

1.3.2 Proton exchange membrane water electrolysis

Proton exchange membrane (PEM), sometimes referred to as solid polymer electrolyte (SPE), water electrolysis is based on the use of a polymeric proton exchange membrane as the solid electrolyte. Ultra pure water is fed to the anode structure of the electrolysis cell composed of porous titanium and activated by a mixed noble metal oxide catalyst. The membrane conducts hydrated protons from the anode to the cathode side.

Appropriate swelling procedures have led to low ohmic resistances enabling high current density of the cells. The standard membrane material used in PEM water electrolysis units is a perflourosulfonic acid polymer called Nafion™ 117, (DuPont). The cathode of such an electrolyser consists of a porous graphite current collector with either Pt or a mixed oxide as electrocatalyst. Individual cells are stacked into bipolar modules with graphite based separator plates providing the structure for water feed and product gas evacuation. The operation of the cells leads to electro osmotic water transport through the membrane from the anode to the cathode side.^[28] Commercial PEM electrolyzers are currently available such as the Hogen® PEM electrolyser (Proton Energy Systems). There are several advantages of polymer electrolyte technology over alkaline systems. Greater safety and reliability is expected, since no caustic electrolyte is circulated in the cell stack. PEM electrolyzers are able to operate with the variable power input from renewable energy sources. Some PEM materials are able to sustain high differential pressure without damage and have proven efficient in preventing gas mixing.^[29]

1.3.3 Advantages and Disadvantages of conventional electrolyzers

Current alkaline and polymer membrane-based electrolysis systems suffer several disadvantages. The hydrogen product gas is saturated with water vapour; the gas must be dried before the hydrogen can be stored in a hydride bed. Both technologies require high loading of precious metal catalysts to reduce the overpotential losses. Neither technology is amenable to high-pressure operation. Polymer membrane cells allow high crossover rates of gases across the membranes at elevated pressures. Long-term stability and contamination is a problem with both alkaline and PEM electrolytes.

Contamination is also a problem for both types of electrolyser. Alkaline electrolytes adsorb carbon dioxide readily and form carbonates. Polymer membrane systems must employ very pure de-ionised water or they will accumulate cations that displace protons and increase the cell resistance over time. High-pressure operation of PEM electrolyser can result in losses due to hydrogen permeation through the membrane.

The main advantage of alkaline and polymer electrolyzers comes from the low operating temperature. Both systems operate at or near room temperature; therefore, no additional heating equipment is required. In addition, alkaline electrolysis is a well-proven technology with several manufacturers offering commercially available units.

References

- ¹ Lide, D., *CRC Handbook of Chemistry and Physics*, 76th Edition, Boca Raton, Florida: CRC Press Inc, 1995.
- ². Webb, R. K., "Sir William Robert Grove (1811–1896) and the origins of the Fuel Cell", *Journal of the Royal Institute of Chemistry*, 85 (1961), 291. Grove's papers on this subject appeared in *Phil. Mag.*, Feb. 1839 and Dec. 1842, and *Phil. Trans.*, 1843
- ³ National Hydrogen Association, U. S. D. o. E. History of Hydrogen. from www.eere.energy.gov/hydrogenandfuelcells/
- ⁴ Romm, J. *The Hype About Hydrogen: Fact and Fiction in the Road to Save the Climate.* Washington D.C.: Island Press, 2004.
- ⁵ Haldane, J.B.S., "Daedalus; or Science and the future," paper read to the Heretics, Cambridge, Feb. 4th, 1923
- ⁶ Barreto, L., Makihira, A., and K Raihi. "The Hydrogen Economy in the 21St Century: a Sustainable Development Scenario." *International Journal of Hydrogen Energy* 28 (2003): 267-84.
- ⁷ Zittel, W. and Wurster, R. "Hydrogen in the Energy Sector." www.hyweb.de Ludwig-Bölkow-Systemtechnik GmbH
- ⁸ Adamson, K., and Pearson, P. "Hydrogen and Methanol: a Comparison of Safety, Economics, Efficiencies and Emissions." *Journal of Power Sources* 86 (2000): 548-55.
- ⁹ Alcock, J.L., L.C. Shirvill, and R.F. Cracknell. "Compilation of Existing Safety Data on Hydrogen and Comparative Fuels." European Integrated Hydrogen Project (EIHP 2) (2001):
- ¹⁰ PlugPower Inc. (2005). "Hydrogen: the Fuel of the Future." from www.pluginpower.com
- ¹¹ United States Department of Energy (DOE), National H₂ Energy Roadmap. www.eere.energy.gov Washington D.C.
- ¹² Kermode, R.I. "Hydrogen From Fossil Fuels." In *Hydrogen: Its Technology and Implications Vol. 1 Hydrogen Production Technology*, edited by K Cox, and K.D. Williamson, 3-41. Cleveland: CRC Press, 1977.
- ¹³ Van der Berg, G. J., Dammers, W. R., and TeriHarr, L.W. "Hydrocarbon Gasification Process." In *Journal of Advances in Petroleum Chemistry and Refining*, Vol. 10, New York: Interscience, 1965.
- ¹⁴ Shoko, E., McLellan, B., Dicks, A.L., and Diniz da Costa, J.C. "Hydrogen From Coal: Production and Utilisation Technologies." *International Journal of Coal Geology* 65 (2006): 213-22.
- ¹⁵ Damen, K., M. van Troost, A. Faaij, and W. Turkenburg. "A Compariston of Electricity and Hydrogen Production Systems With CO₂ Capture and Storage. Part a: Review of Selection of Promising Conversion and Capture Technologies." *Progress in Energy and Combustion Science* In Press

- ¹⁶ Billings, R. *Hydrogen From Coal*. Tulsa: PennWell Publishing Co, 1983.
- ¹⁷ Czernik, S., R. French, C. Feik, and E. Chornet. "Production of Hydrogen From Biomass By Pyrolysis/Steam Reforming." In *Advances in Hydrogen Energy*, edited by C. Gregoire-Padro, and F Lau, 87-92. New York: Klewer Academic, 2000.
- ¹⁸ Ni, M., D. Leung, M. Leung, and K. Sumathy. "An Overview of Hydrogen Production From Biomass." *Fuel Processing Technology* In Press
- ¹⁹ Ghirari, M.L., Zhang, L., Lee, J.W., Flynn, T., Seibert, M., Greenbaum, E., and Melis, A. "Microalgae: a Green Source of Renewable H₂," *Trends in Biotechnology* 18 (2000): 506-11.
- ²⁰ Levin, D., Pitt, L., and Love, M. "Biohydrogen Production: Prospects and Limitations to Practical Application." *International Journal of Hydrogen Energy* 29 (2004): 173-85.
- ²¹ Fujishima, A., and Honda, K. "Electrochemical Photolysis of Water At a Semiconductor Electrode." *Nature* 238 (1972): 37-38.
- ²² Rocheleau, R., Miller, E., and Misra, A. "High-Efficiency Photoelectrochemical Hydrogen Production Using Multijunction Amorphous Silicon Photoelectrodes." *Energy Fuels* 12 (1998): 3-10.
- ²³ Kubo, S., Nakajima, H., Seiji, K., Higashi, S., Masaki, T., Hiroyoshi, A., and Onuki, K. "A Demonstration Study on Closed-Cycle Hydrogen Production By the Thermochemical Water-Splitting Iodine-Sulphur Process." *Nuclear Engineering and Design* 233 (2004): 347-54.
- ²⁴ Fickett, A. P., and F.R. Kalhammer. "Water Electrolysis." In *Hydrogen: Its Technology and Implications Vol. 1 Hydrogen Production Technology*, edited by K Cox, and K.D. Williamson, 3-41. Cleveland: CRC Press, 1977.
- ²⁵ Kreuter, W., and H. Hofmann. "Electrolysis: the Important Energy Transformer in a World of Sustainable Energy." *International Journal of Hydrogen Energy* 23 (1998): 661-66.
- ²⁶ Donitz, W., E. Erdle, and R. Streicher. "Chapter 2: High Temperature Electrochemical Technology for Hydrogen Production and Power Generation." In *Electrochemical Hydrogen Technologies: Electrochemical Production and Combustion of Hydrogen*, edited by H. Wendt, Amsterdam: Elsevier Science Ltd, 1990.
- ²⁷ Onda, K., Kyakuno, T., Hattori, K., and K. Ito. "Prediction of Production Power for High-Pressure Hydrogen By High-Pressure Water Electrolysis." *Journal of Power Sources* 132 (2004): 64-70.
- ²⁸ Grigoriev, S.A., Poremsky, V.I., and Fateev, V.N. "Pure hydrogen production by PEM electrolysis for hydrogen energy." *International Journal of Hydrogen Energy* 31 (2006): 171-175
- ²⁹ Barbir, F. "PEM Electrolysis for Production of Hydrogen From Renewable Energy Sources," *Solar Energy* 78 (2005): 661-69.

Chapter 2: Solid Oxide Steam Electrolysis

Background and Theory

2.1	Solid oxide steam electrolysis.....	25
2.1.1	Thermodynamics of electrolysis.....	26
2.1.2	Equilibrium Nernst potential	28
2.1.3	Operating cell polarisation	29
2.1.3.1	Ohmic losses	30
2.1.3.2	Concentration polarisation	30
2.1.3.3	Activation polarisation.....	31
2.1.4	Electrolysis efficiency	32
2.2	Component materials	32
2.2.1	Electrolyte	33
2.2.2	Cathode.....	33
2.2.3	Anode	33
2.3	Previous work	34
2.3.1	Hot Elly	34
2.3.2	Westinghouse electrolyser.....	35
2.3.3	INEEL Electrolyser	36
2.3.4	JAERI high temperature electrolyser system	37
2.3.5	Natural gas assisted electrolyser.....	38
2.3.6	Proton conductor electrolyser.....	39
2.3.6.1	Proton conductor background	40
2.3.6.2	Solid Protonic Steam Electrolysis.....	41
References		42

2.1 *Solid oxide steam electrolysis*

Solid oxide electrolyzers are solid-state devices without sensitive electrode electrochemistry, and they are well suited to operate at elevated pressures. These devices use steam and do not require the expensive cation removal from the water or carbon dioxide removal from the gas. The solid oxide cells operate at temperatures ranging from 750-1000 °C and thus at a lower thermodynamic potential than the low-temperature systems. The elevated operating temperatures enable the use of non-precious metal electrodes, and electrode reaction kinetics may also be faster at these elevated temperatures. Temperatures in this range are directly compatible with solar furnace or advanced thermonuclear operating temperatures, offering the potential for integrated electrical/hydrogen generation systems.^[1,2]

The process of the solid oxide high-temperature electrolysis of steam is a reverse reaction of a solid oxide fuel cell (SOFC). An oxygen ion conductor is used as a solid electrolyte. At elevated temperatures, certain ceramic materials, such as yttria-stabilised zirconia (YSZ) and doped ceria, become oxygen ion conductors. The configuration of a solid oxide electrolysis cell is shown in Figure 2.1. The cell is comprised of a thin, dense disk of YSZ between two porous electrodes. The porous electrodes facilitate the formation of three-phase boundaries, which are the interfaces between the electrolyte, electrode, and gas. The electrodes must be porous enough to allow the gas to diffuse easily, but not so porous as to become poor electrical conductors.

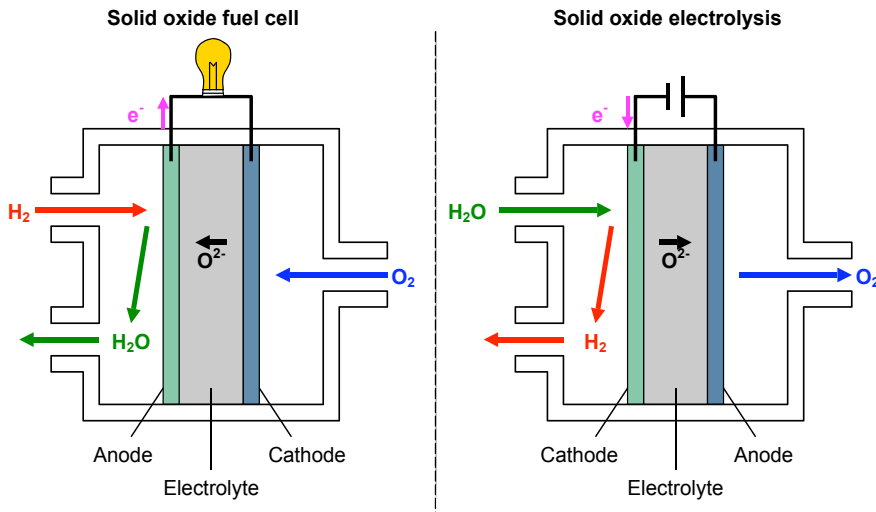


Figure 2.1 Solid oxide fuel cell (SOFC) and solid oxide electrolysis processes

For hydrogen production, steam is fed into the cathode side. The steam is dissociated with electrons from externally provided electricity on the surface of the cathode according to the following reaction:



An oxygen atom is liberated from the H_2O molecule and picks up two electrons from the cathode to become an oxygen ion. The oxygen ion is then transported through the electrolyte by means of oxygen ion vacancies in the crystal lattice of the electrolyte. At the anode-electrolyte interface, the oxygen ion transfers its charge to the anode, combines with another oxygen atom to form O_2 gas, and diffuses out of the anode. This anode reaction is represented as follows:



The hydrogen ions remaining at the cathode combine with electrons to form H_2 gas. The products, hydrogen and oxygen, are separated by the gastight electrolyte.

2.1.1 Thermodynamics of electrolysis

The formation or splitting of water (liquid or gaseous phase) proceeds according to the following reaction:



The energy change of the process is given by

$$\Delta H = \Delta G + T\Delta S \quad (2.4)$$

Where T is the absolute temperature; ΔH is the enthalpy change; ΔS is the change in entropy; and ΔG is the Gibb's Free Energy, the maximum work for formation of water, or specifically the minimum work required to split water. The term $T\Delta S_{\text{split}}$ can be viewed as the amount of thermal energy required to split water with the minimum of electrical energy. A plot showing the thermodynamic equations associated with electrolysis can be seen in Figure 2.2.

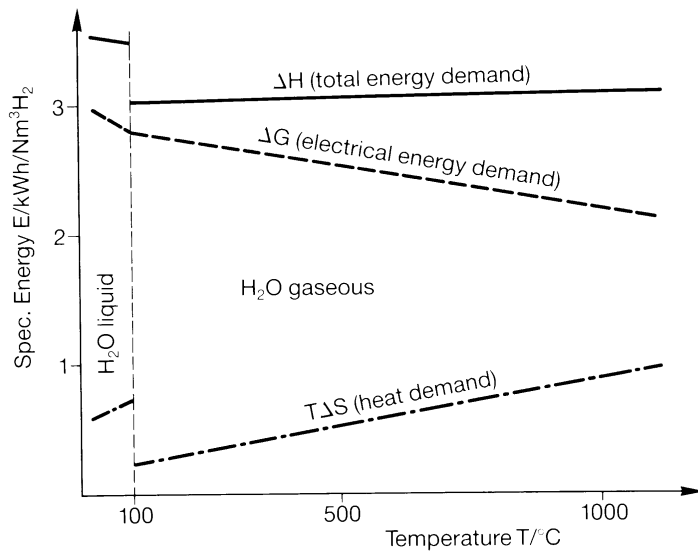


Figure 2.2 Thermodynamics of electrolysis [2]

There are several advantages to high-temperature electrolysis. The total energy demand, ΔH_{split} , is lower in the vapour phase than in the liquid phase. The minimum demand for electrical energy, ΔG_{split} , needed for electrolysis decreases with increasing temperature. A portion of the splitting energy is provided by thermal energy rather than electrical energy, thus achieving higher total electrical efficiency. High operating temperature generally improves electrode reaction kinetics.^[3,4]

2.1.2 Equilibrium Nernst potential

The net reaction for solid oxide steam electrolysis is given by:



The Gibb's free energy change, ΔG , for this reaction is given by the following expression:

$$\Delta G = \Delta G^\circ + RT \ln \left(\frac{a_{H_2} a_{O_2}^{1/2}}{a_{H_2O}} \right) \quad (2.6)$$

where ΔG° is the standard Gibb's free energy change per mole for reaction (2.5) at a temperature T in Kelvin. R is the gas constant (8.3147 J/K·mol). a_{H_2} , a_{O_2} and a_{H_2O} are the activities of H₂, O₂ and H₂O in the reaction. Reaction (2.5) proceeds entirely in the gas phase so the activities can be expressed as partial pressures for an ideal gas in (2.6).

$$\Delta G = \Delta G^\circ + RT \ln \left(\frac{P_{H_2} P_{O_2}^{1/2}}{P_{H_2O}} \right) \quad (2.7)$$

For electrolysis the potential difference, E , in the electrolysis cell is related to the Gibb's free energy by the following:

$$E = \frac{\Delta G}{zF} \quad (2.8)$$

where F is the Faraday constant (96,487 C/mol) and n denotes the number of electrons participating in the reaction, in the case for steam electrolysis, $z=2$. The electromotive force (EMF) at standard pressure, E° , is similarly related to the standard Gibb's free energy, thus:

$$E^\circ = \frac{\Delta G^\circ}{zF} \quad (2.9)$$

Equation (2.7) may be rewritten using (2.8) and (2.9) as,

$$E = E^\circ + \frac{RT}{2F} \ln \left(\frac{P_{H_2} P_{O_2}^{1/2}}{P_{H_2O}} \right) \quad (2.10)$$

Equations such as (2.10), which give a potential in terms of product and reactant activity or partial pressure are known as Nernst equations, and the potential calculated is called

the Nernst potential. The Nernst potential, also called open circuit voltage (OCV), is the reversible cell voltage that would exist at a given temperature and partial pressure. Open-circuit voltage is produced by the difference in oxygen partial pressure from one side of the cell to the other. The open-circuit voltage depends on the temperature, the gas concentration ratio H_2/H_2O in the cathode compartment and the oxygen partial pressure at the anode. [5,6]

2.1.3 Operating cell polarisation

The open-circuit voltage is a reversible phenomenon that occurs with no external potential load. In an operating cell with an applied potential the system becomes irreversible. This voltage loss is a function of current density and is known as *polarisation* or *overpotential*. The terms polarisation and overpotential are often used interchangeably in literature. Total cell polarisation, η , is comprised of the ohmic losses, η_{ohm} , concentration polarisation, η_{conc} and activation polarisation, η_{act} . The concentration and activation polarisations each have a separate contribution from the cathode and anode portion of the cell. [5,7] The total polarisation for the cell is obtained by the summing the individual polarisation contributions, as given by:

$$\eta = \eta_{ohm} + \eta_{conc} + \eta_{act} \quad (2.11)$$

A schematic plot of voltage versus current density showing the different types of polarisation responses is presented in Figure 2.3. Activation polarisation is usually non-linear and is dominant at low current densities. The concentration polarisation also usually non-linear and is dominant at high current densities. The ohmic losses are seen as a deviation from the open circuit voltage, and are represented in the cell current as the slope of the linear region.

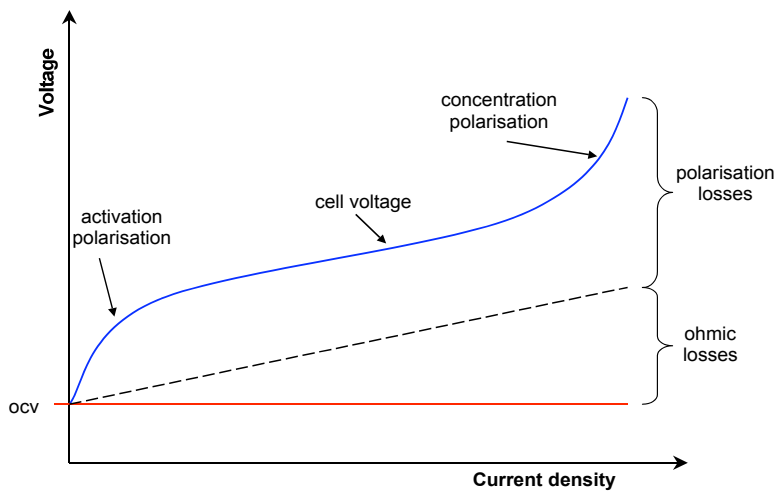


Figure 2.3 Voltage versus current density plot illustrating the different types of polarisations in the operating electrolysis cell.

2.1.3.1 Ohmic losses

The ohmic losses are due to electrical resistances of the electrical contacts, interconnections, lead wires, and electrodes, as well as the ionic resistance of the electrolyte, the ohmic losses are sometimes termed the *resistance polarisation*, and are dependent on the electrolysis cell materials and geometry. The largest contribution to the ohmic losses is often due to the electrolyte, since the ionic resistivity of the electrolyte is much greater than the electronic resistivities of the cathode and anode. The ohmic polarisation is proportional to the current density and has a linear response. A general expression to describe the ohmic losses is given by:

$$\eta_{ohm} = ir \quad (2.12)$$

where, i is the cell current density and r is the area specific resistance of the cell.^[5,7]

2.1.3.2 Concentration polarisation

The reacting species in the electrolysis cell are all gaseous, so the cathode and anode reaction rate depends on the gas transport through the porous electrode materials. The physical resistance to the transport of the gases through the electrodes at a given current density is reflected in the cell performance as an electrical voltage loss. This loss is the concentration polarisation. The concentration polarisation is mainly caused by a low steam concentration at the cathode. The concentration polarisation is a function of the

diffusivities of the gas species, the electrode microstructure, the partial pressures of the gases and the current density and has a non-linear response. A general expression for the concentration polarisation is given by:

$$\eta_{conc} = \frac{RT}{zF} \ln\left(1 - \frac{i}{i_l}\right) \quad (2.13)$$

where i_l is the limiting current density at which the steam is used up at a rate equal to its maximum supply speed and is a function of the diffusivity of the gas and the partial pressure. The expression (2.13) is only valid for current densities such that $i < i_l$.^[5,7]

2.1.3.3 Activation polarisation

The activation polarisation is defined as the external energy required to overcome the maximum activation energy barrier in order to maintain the electrode reaction. This irreversible polarisation is associated with the electrode reactions involving charge transfer where the neutral species is converted to an ion or an ion converted to a neutral species. It is highly dependent on the charge transfer mechanism and electrocatalysis at the three-phase boundaries. The electrode reaction can involve many steps, for example:

- 1) surface adsorption of gaseous species
- 2) dissociation of adsorbed molecules to adsorbed atoms
- 3) surface diffusion to three-phase boundaries
- 4) formation of ions by electron transfer and incorporation of ions into electrolyte

Any of the above steps could be the slowest, therefore the rate-determining step. The rate of the electrode reaction is proportional to the current density. The activation polarisation is a function of material properties and microstructure, temperature, atmosphere, and current density. A general expression for the activation polarisation, η_{act} is given by:

$$\eta_{act} = \frac{RT}{z\alpha F} \ln\left(\frac{i}{i_o}\right) \quad (2.14)$$

where α is the charge transfer coefficient for the electrode material, and i_o is the exchange current density. Equation (2.14) is known as the Tafel equation, and can be expressed in many forms. In the case of steam electrolysis, equation (2.14) is only valid at cell current densities such that $i > i_o$.^[5,7]

2.1.4 Electrolysis efficiency

The electrolysis cell efficiency can be estimated from the applied voltage, applied current and hydrogen production rate. The Faraday efficiency, ε_f is the ratio of theoretical electrical power needed for electrolysis and the practical applied power to the cell. It can be calculated from of Gibbs's free energy change and applied power by the following expression:

$$\varepsilon_f = \frac{2F(E - \eta)Q}{IE} \quad (2.15)$$

where E is the applied voltage, η is the cell polarisation, Q is the hydrogen production rate in mol/s, and I is the current.

The energy efficiency, ε_e , is the ratio of the energy content of the produced hydrogen to the applied power. The energy content of the hydrogen can be approximated using the heat of combustion for hydrogen at the lower heating value for the electrolysis net reaction (2.5). The energy efficiency is given by the following expression:

$$\varepsilon_e = \frac{\Delta H_c Q}{IE} \quad (2.16)$$

Note that the hydrogen production rates for both efficiency expressions are in units of cm³/min, so the value must be divided by the standard volume of one mole of an ideal gas at room temperature, which is 26 litres/mol.^[5,7,8]

2.2 Component materials

Electrolysis cell components are exposed to strong reducing and oxidising atmospheres at high temperatures, so materials selection and optimisation are critical. The electrolyte membrane should be gastight to prevent mixing of product gases, and the membrane should be as thin as possible to minimize the voltage drop across the cell. Electrodes must be chemically stable in their respective atmosphere and be good electronic conductors. Electrode materials must have porosity sufficient to allow for gases to reach and leave the reaction sites at the three phase boundaries. The thermal expansion coefficients of all component materials must be close to that of the electrolyte. Interconnect materials must

be stable in both reducing and oxidising conditions. Also, good adhesion must exist between all components, with no reactions between the materials.^[2,9]

2.2.1 Electrolyte

Oxygen-ion conducting ceramics are used as the electrolyte; ZrO_2 doped with 8% Y_2O_3 , called yttria-stabilised zirconia (YSZ), is commonly used. Doping with yttrium, which has a lower valence (+3) compared to zirconium (+4), produces oxygen vacancies in the crystal lattice. This allows oxygen ion conductivity. Zirconia is also stabilised by this additive in its cubic phase.

2.2.2 Cathode

The cathode of a high temperature electrolysis cell is operating in a reducing atmosphere. Inexpensive transition metals (Ni, Co) with a melting point above 1000 °C can be used, typically mixed with YSZ to form a porous cermet. Mixing with the ceramic provides stability and gives a suitable porous morphology.

2.2.3 Anode

The anode operates in an oxidising environment. Noble metals, such as platinum, work well but must be ruled out because of their high cost. Electronically conducting mixed oxides of the ABO_3 perovskite type structure, such as those based on LaMnO_3 or LaCoO_3 , also work well.

2.3 Previous work

2.3.1 Hot Elly

The Hot Elly (High Operating Temperature Electrolysis) system developed by Dornier GmbH, Lurgi GmbH and Robert Bosch GmbH, included electrolysis cell research and pilot plant tests. The Hot Elly electrolysis system consisted of ring cells connected in series to form self-supported tubes. The ring cells were fabricated from a cylindrical electrolyte with porous thin-layer electrodes on the inner and outer surface. The cells were connected in series by an interconnect material. Table 2.1 gives the Hot Elly electrolysis cell details. The tubular cell geometry is favoured over planar cell geometry with respect to steam and gas routing as well as for separating the product gases. The steam enters the tube at one end and a mixture of about 80% hydrogen and 20% steam exits at the other end. The electrolysis requires high temperature steam at 1000 °C, some of which is generated utilising heat recovered from the product gases. Experimental results from a 10-cell tube, a 5-tube stack, and a 100-tube module are given in Table 2.2.

[1,2]

Table 2.1 Hot Elly electrolysis cell specifications

Component	Material	Dimensions
Electrolyte	YSZ (8-12 mol% Y_2O_3)	0.3 mm thick
Anode	LSM	0.25 mm thick
Cathode	Ni-YSZ cermet	0.1 mm thick
Interconnect	Mg-, Ca- or Sr-doped LaCrO_3	not available
Complete Electrolysis cell		10 mm long 14 mm outer diameter

Table 2.2 Hot Elly experimental results

	Temperature (°C)	Current (A)	Voltage (V)	H_2 production rate (NI/hr)	H_2 production (NI/W•hr)
10-cell tube	997	0.37	13.2	6.78	1.39
5-tube stack	996	1.4	13.2	31.5	1.70
100-tube module	1000	14	13.2	600	3.24

The Hot Elly system can be operated in either endothermic or exothermic mode. The operating mean cell voltage for the system is 1.3V, which corresponds to the total water dissociation enthalpy demand. At this voltage the electrolyser is thermodynamically self-sustaining provided the inlet steam is heated to the operating temperature before entering the cell. The electrolyser can be operated in endothermic or exothermic mode, as shown in Figure 2.4. This operation requires less electricity, and has a high overall efficiency, but the inlet gas must be preheated to operation temperature. Also the size of the electrolyser must increase because of the lower current densities. In exothermic mode, the cells are operated above the thermoneutral voltage. More electricity is required, but the electrolyser produces excess heat which can be used to heat the inlet gas without the need for additional equipment.^[2]

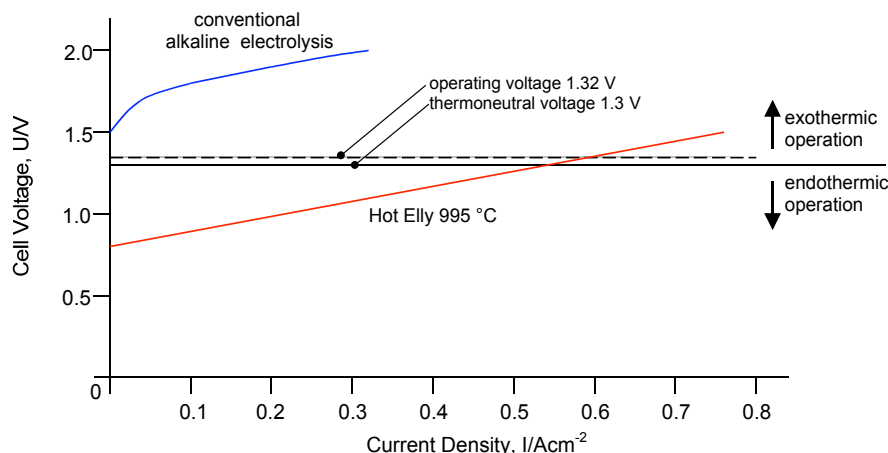


Figure 2.4 Current voltage characteristics of the Hot Elly electrolysis cell and the operation possibilities^[2]

Westinghouse electrolyser

Westinghouse Electric Co. developed an electrolyser tube cell based on a design originally used for solid oxide fuel cells. The design consisted of a porous calcia-stabilised zirconia (CSZ) tube, closed at one end with the anode, electrolyte and cathode material layers deposited on the support. Table 2.3 gives the details of the Westinghouse electrolyser design. The experimental performance of the Westinghouse design is presented in Table 2.4.^[10]

Table 2.3 Westinghouse electrolyser tube specifications

Component	Material	Dimensions
Support tube	CSZ	1000mm long 13 mm inner diameter 1-1.5 mm thick
Anode	LSM	1.4 mm thick
Electrolyte	YSZ (10 mol% Y_2O_3)	0.04 mm thick
Cathode	Ni-YSZ cermet	0.1 mm thick

Table 2.4 Westinghouse electrolyser tube performance

	Temperature (°C)	Current (A)	Voltage (V)	H_2 production rate (NI/hr)	H_2 production (NI/W•hr)
Single cell tube	1000	0.4	1.23	17.6	35.8

2.3.2 INEEL Electrolyser

The Idaho National Engineering and Environmental Laboratory (INEEL) and Ceramatec, Inc., developed a reversible high-temperature electrolysis system. Unlike most other designs the INEEL electrolyser used planar cell geometry. The details of the planar cell are given in Table 2.5. Several electrolyte materials were investigated for this system including YSZ, scandia-stabilised zirconia (ScSZ), and lanthanum strontium gallium magnesium oxide (LSGM). The experimental performance of two single cell electrolyzers and a 6-cell stack, made from planar cells connected in series, are presented in Table 2.6. The INEEL design was tested in both electrolyser and fuel cell modes to assess the possibility of a reversible fuel cell/electrolyser system.^[11,12]

Table 2.5 INEEL electrolyser specifications

Component	Material	Electrolyte supported dimensions	Cathode supported dimensions
Anode	LSM	0.05 mm thick	0.05 mm thick
Electrolyte	YSZ, ScSZ, LSGM	0.10 mm thick	0.01 mm thick
Cathode	Ni-YSZ	0.05 mm thick	1.5 mm thick
Interconnect	Ferritic stainless steel	1-2.5 mm thick	1-2.5 mm thick
Planar cell		64 cm ² area	64 cm ² area

Table 2.6 INEEL electrolyser system performance

	Temperature (°C)	Current (A)	Voltage (V)	H2 production rate (Nm³/hr)
LSGM single cell	800	0.9	1.4	----
ScSZ single cell	850	0.2	1.3	----
6-cell stack	850	0.22	-----	32

2.3.3 JAERI high temperature electrolyser system

Japan Atomic Energy Research Institute (JAERI) conducted electrolysis testing using a high-temperature engineering nuclear test reactor to provide the necessary heat and electricity.^[13] JAERI tested both electrolysis tubes and a self-supporting planar electrolyser. The electrolysis tube consisted of 12 individual cells connected in series on a single porous support tube. The cell materials were layered on the support tube by means of a plasma spray technique. The self-supporting planar design used YSZ plates with plasma-sprayed electrodes on either side contained in a metal housing. The details of the JAERI electrolyser can be found in Table 2.7, and the system performances in Table 2.8. After testing, the JAERI electrolyser tubes exhibited considerable anode degradation. The LaCoO₃ anode material was not properly bonded to the electrolyte and thus decreased the performance of the tubes. An advanced spray technique such as vacuum plasma spraying was suggested to overcome the bonding problem.

Table 2.7: JAERI electrolyser specifications

Component	Material	Tube dimensions	Planar cell dimensions
Anode	LSCo(tube); LSM (planar)	19 mm long 0.1-0.25 mm thick	80 mm ² area 0.03 mm thick
Electrolyte	YSZ	19 mm long 0.1-0.25 mm thick	100 mm ² area 0.3 mm thick
Cathode	Ni-YSZ	19 mm long 0.1-0.25 mm thick	80 mm ² area 0.03 mm thick
Interconnect (planar)	Pt mesh	-----	0.01 thick
Support (tube)	CSZ	710 mm long 22 mm diameter 3 mm thick 38%porosity	-----

Table 2.8: JAERI electrolyser system performance

	Temperature (°C)	Current (A)	Voltage (V)	H ₂ production rate (NI/hr)	H ₂ production (NI/W•hr)
12-cell tube	850	1.42	15.7	3.8	0.17
12-cell tube	900	1.38	16.3	4.3	0.19
12-cell tube	950	1.72	15.6	6.9	0.26
planar	850	3.72	2.68	2.4	0.24

2.3.4 Natural gas assisted electrolyser

In most steam electrolyzers the gas supplied to the cathode is usually a mixture of steam and hydrogen, while the gas supplied to the anode is usually air or oxygen. To electrolyse water, a voltage that opposes and is higher than the open circuit voltage must be applied to pump oxygen from the steam side to the air side. Much of the electricity used, 60 to 70% of the total electrical power, is employed in forcing the electrolyser to operate against the high chemical potential gradient for oxygen.^[14]

One approach to reduce the electricity consumption in electrolyzers is by using natural gas on the anode side to reduce the chemical potential difference across the electrolyser cell. The concept is called Natural-Gas-Assisted-Steam Electrolysis (NGASE)^[15] and is

being developed at the Lawrence Livermore National Laboratory. In this technology, the air in the anode side is replaced with natural gas to lower the open circuit voltage and, thereby, the electricity consumption. The reducing character of natural gas helps to lower the chemical potential difference between the two sides of the electrolyser. The main drawback of the NGASE is that it is not a carbon free process.

The NGASE electrolyser uses porous Ni-YSZ cermet anode support tubes with the electrolyte and anode thin film layers deposited by colloidal spray deposition. The electrolyte material used is YSZ. Further details of the NGASE fabrication and cathode materials are not available at this time. The experimental performance of the NGASE electrolyser single tube and 4-tube stack^[14] are presented in Table 2.9. The performance at 900 °C is significantly better than at 700 °C, but operation at 900 °C is not ideal. Steam needs to be introduced into the natural gas inlet to avoid carbon deposition on the anode. The presence of the steam causes steam reforming of the natural gas; this reaction is undesirable as it is highly endothermic. Operation at 700 °C minimizes the amount of steam required on the anode side.

Table 2.9 NGASE electrolyser performance

	Temperature (°C)	Current (A)	Voltage (V)	H ₂ production rate (NI/hr)	H ₂ production (NI/W•hr)
Single tube	700	1.0	0.45	-----	-----
Single tube	900	2.8	0.5	-----	-----
4-tube stack	750	1.0	0.5	39	19.5

2.3.5 Proton conductor electrolyser

A promising alternative to liquid and polymer membrane electrolytes is a proton-conducting ceramic solid electrolyte technology. This technology is intrinsically different from zirconia-based oxygen ion electrolyzers in that the transported species is hydrogen rather than oxygen. The zirconia oxide ion systems produce a wet hydrogen product stream. The proton conducting ceramic electrolyte does not suffer from this disadvantage and produces a hydrogen stream that requires no further purification. The electrolysis of

water vapour on oxygen ion and proton conducting ceramics is illustrated in Figure 2.5. Other possible advantages include better electrode kinetics and reduced ohmic losses.

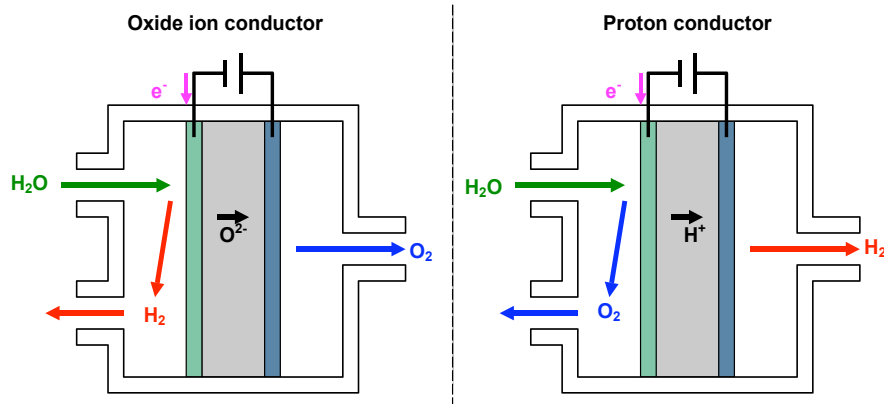


Figure 2.5 Steam electrolysis using oxide ion conducting electrolyte and proton conducting electrolyte.

2.3.5.1 Proton conductor background

A number of perovskite structure ceramic proton separation membranes have been developed as reported by Iwahara.^[16,17] These materials exhibit good stability, high ionic transport rates for protons, and operate in the 600-900 °C temperature range. The materials are also valuable for high temperature fuel cell technologies, isotope separation systems, sensor applications, heterogeneous catalysis, and water electrolysis. The proton conducting materials are rare earth cerate and zirconate ABO_3 formula oxides, e.g., $(\text{Sr},\text{Ba})(\text{Zr},\text{Ce})(\text{B})^{3+}\text{O}_{3-y}$, where $(\text{B})^{3+}$ is a tri-valent yttrium or lanthanide cation. The crystal structures of all of these materials are typically orthorhombic distortions of the cubic perovskite structure, with oxygen ion vacancies introduced by the $(\text{B})^{3+}$ substituting for four valent zirconium or cerium. Exposing these materials to steam at elevated temperatures causes water to hydrolyse and fills the vacancies with oxygen and two mobile protons.

Iwahara and other investigators^[16,17,18,19,20] have studied the ionic and electronic conductivities, conduction mechanism, and thermodynamic stability of these materials. The motivation for most of this work derives from the desire to utilise these materials for high-temperature, hydrogen-fuelled solid oxide fuel cells. In a reverse operation mode, it

is possible to electrolyse water to produce hydrogen. Electrolysis cells can be made of metal or metal oxide electrodes deposited onto a proton conducting material. The application of an electric potential to the electrodes will cause a hydrogen partial pressure difference across the pellet. The difference in hydrogen activity is high enough to decompose water at elevated temperatures.

The Sr and Ba-doped cerate electrolytes exhibit the highest proton conductivities; however, recent reports question the thermodynamic stability of the Ba compounds at intermediate temperatures and in the presence of high partial pressures of CO₂ and H₂O. It is unclear whether this will present a problem for electrolysis applications. Ceramics processing also plays an important role in determining the conductivities of these materials

2.3.5.2 Solid Protonic Steam Electrolysis

Matsumoto et al. investigated steam electrolysis using a proton-conducting electrolyte material SrCe_{0.95}Yb_{0.05}O_{3- α} .^[18] Test cell specifications and experimental performance are shown in Table 2.11, respectively.

Table 2.10 Proton conductor electrolysis cell specifications

Component	Material	Dimensions
Electrolyte	SrCe _{0.95} Yb _{0.05} O _{3-α}	6 mm thick 13mm diamter
Cathode and anode	Pt	0.5 mm thick

Table 2.11 Proton conductor electrolysis experimental performance

	Temperature (°C)	Current (A)	Voltage (V)	H ₂ production rate (NI/hr)
Single cell	800	0.6	-----	80

References

- ¹ Quandt, K.H. and Streicher R. "Concept and Design of a 3.5 MW Pilot Plant for High Temperature Electrolysis of Water Vapor." *International Journal of Hydrogen Energy* 11 (1986): 309-15.
- ² Donitz, W., E. Erdle, and R. Streicher. "Chapter 2: High Temperature Electrochemical Technology for Hydrogen Production and Power Generation." In *Electrochemical Hydrogen Technologies: Electrochemical Production and Combustion of Hydrogen*, edited by H. Wendt, Amsterdam: Elsevier Science Ltd, 1990.
- ³ Momma, A., T. Kato, Y. Kaga, and S. Nagata. "Polarization Behaviour of High Temperature Solid Oxide Electrolysis Cells." *Journal of the Ceramic Society of Japan* 105 (1997): 398-402.
- ⁴ Eguchi, K., T. Hatagishi, and H. Arai. "Power Generation and Steam Electrolysis Characteristics of an Electrochemical Cell With Zirconia-Or Ceria-Based Electrolyte." *Solid State Ionics* 86-88 (1996): 1245-49.
- ⁵ Larminie, J. and A. Dicks. *Fuel Cell Systems Explained*. Chichester: John Wiley and Sons, Ltd, 2000.
- ⁶ Bockris, J. and A. K. N. Reddy. *Modern Electrochemistry: Electrodics in Chemistry, Engineering, Biology, and Environmental Science*. New York: Kluwer Academic/Plenum Publishers, 2000.
- ⁷ Ivers-Tiffée, E., and A. Virkar. "Electrode Polarisations." In *High Temperature Solid Oxide Fuel Cells: Fundamentals, Design and Applications*, edited by S. Singhal, and K. Kendall, 231-88. Oxford: Elsevier Ltd, 2003.
- ⁸ Hino, R., K. Haga, H. Aita, and K. Sekita. "R&D on Hydrogen Production By High-Temperature Electrolysis of Steam." *Nuclear Engineering and Design* 233 (2004): 363-75.
- ⁹ Fleig, J., K.D. Kreuer, and J. Maier. "Ceramic Fuel Cells." In *Handbook of Advanced Ceramics Vol. 2*, edited by S. Somiya, F. Aldinger, N. Claussen, R.M. Spriggs, K. Uchino, K. Koumoto, and M. Kaneno, 59-105. San Diego: Elsevier Inc, 2003.
- ¹⁰ Maskalick, N.J. "High Temperature Electrolysis Cell Performance Characterization." *International Journal of Hydrogen Energy* 11 (1986): 563-70.
- ¹¹ Herring, J.S., P.A. Lessing, J.E. O'Brien, and C. Stoots. "High-Temperature Solid-Oxide Electrolyzer System." *DOE Hydrogen Program* (2004):
- ¹² Herring, J.S., J.E. O'Brien, C. Stoots, P.A. Lessing, and R. Anderson. "High-Temperature Solid Oxide Electrolyser System." *DOE Hydrogen, Fuel Cells, and Infrastructure Technologies* (2003):
- ¹³ Hino, R., K. Haga, H. Aita, and K. Sekita. "R&D on Hydrogen Production By High-Temperature Electrolysis of Steam." *Nuclear Engineering and Design* 233 (2004): 363-75.

¹⁴ Martinez-Frias, J. , A-Q Pham, and S. Aceves. "A Natural Gas-Assisted Steam Electrolyzer for High-Efficiency Production of Hydrogen." *International Journal of Hydrogen Energy* 28 (2003): 483-90.

¹⁵ Pham, A-Q, Wallman, H., and Glass, R.S., US patent no 6051125, April 2000.

¹⁶ Iwahara, Hiroyasu. "Hydrogen Pumps Using Proton-Conducting Ceramics and Their Applications." *Solid State Ionics* 125 (1999): 271-78.

¹⁷ Iwahara, H. , H. Matsumoto, and K. Takeuchi. "Electrochemical Dehumidification Using Proton Conducting Ceramics." *Solid State Ionics* 136-137 (2000): 133-38.

¹⁸ Matsumoto, H., M. Okubo, S. Hamajima, K. Katahira, and H. Iwahara. "Extraction and Production of Hydrogen Using High-Temperature Proton Conductor." *Solid State Ionics* 152-153 (2002): 715-20.

¹⁹ Kobayashi, T., K. Abe, Y. Ukyo, and H. Matsumoto. "Reduction of Nitrogen Oxide By Steam Electrolysis Cell Using a Protonic Conductor $\text{SrZr}_{0.9}\text{Yb}_{0.1}\text{O}_{3-\alpha}$ and the Catalyst $\text{Sr}/\text{Al}_2\text{O}_3$." *Solid State Ionics* 134 (2000): 241-47.

²⁰ Kobayashi, T., K. Abe, Y. Ukyo, and H. Matsumoto. "Study on Current Efficiency of Steam Electrolysis Using a Partial Protonic Conductor $\text{SrZr}_{0.9}\text{Yb}_{0.1}\text{O}_{3-\alpha}$." *Solid State Ionics* 138 (2001): 243-51.

Chapter 3: Experimental

3.1 Materials Synthesis and Processing.....	47
3.1.1 Solid State Powder Preparation.....	47
3.1.2 Sol Gel Synthesis	47
3.1.3 Pellet Preparation	50
3.1.4 Screen Printing.....	50
3.1.5 Spin-coating	52
3.1.6 Tape Casting	52
3.1.7 Electrolysis Tube Fabrication	55
3.2 Electrochemical Testing.....	57
3.2.1 Electrolysis pellet cell testing.....	57
3.2.2 Electrolysis tube cell testing.....	59
3.2.3 Oxygen sensor.....	61
3.3 AC Impedance Spectroscopy.....	64
3.3.1 Theory	64
3.3.2 Equivalent circuits.....	66
3.4 Electron Microscopy	69
3.4.1 Scanning Electron Microscopy (SEM)	69
3.4.2 Electron Dispersive Spectroscopy (EDS)	72
3.4.3 Characteristic X-Ray Spectrum.....	72
3.4.4 Bragg's Law.....	76
3.4.5 Sample preparation	78
3.5 X-Ray Diffraction	79
3.5.1 Powder Diffraction.....	79
3.5.2 Sample Preparation	80
3.6 Dilatometry	80
References	82

3.1 Materials Synthesis and Processing

3.1.1 Solid State Powder Preparation

LaCoO₃ powder was prepared from dried La₂O₃ and CoCO₃ precursor powders. The powders were weighed in the appropriate stoichiometric ratios to make a 5g batch on electronic scales, $\pm 0.1\text{mg}$. The powders were mixed in an agate mortar and pestle with acetone for approximately 20 minutes. The mixed powders were then heat treated in a platinum crucible from room temperature up to 1000 °C and held for 8 hours in ambient atmosphere in a muffle furnace. The resulting calcined powder was then analysed with X-ray diffraction to determine the phases present.^[1]

3.1.2 Sol Gel Synthesis

3.1.2.1 Process description

Sol-gel processing is a versatile method for making ceramic and glass materials at temperatures below 1000 °C. This process allows for the synthesis of multi-element ceramic powders, films, ceramic fibres, microporous membranes, porous aerogels, and dense ceramic materials at temperature far below those required for solid-state synthesis (generally greater than 1000 °C).

The precursors used for synthesizing the sol are inorganic metal salts or metal organic compounds such as metal alkoxides. In a typical sol-gel process, the precursor is subjected to a series of hydrolysis reactions, followed by water, and alcohol condensation reactions. The particles in the sol then combine to form a gel network. By changing reaction variables such as pH, temperature, catalyst addition, and concentrations, the structure and properties of the sol, gel, and ultimately the final product can be carefully controlled.^[2]

Various processing routes lead to the fabrication of different forms of ceramic materials. Ultra-fine and uniform ceramic powders are formed by precipitation or spray pyrolysis,

followed by heat treatment. Spin-coating or dip-coating the sol material on a substrate will form thin films. Casting a sol into a mould will form a wet gel, which can then be dried to form a xerogel and heat treated to produce a dense ceramic. Removing the liquid in a wet gel under special conditions can make a highly porous and extremely low-density material called aerogel. Ceramic fibres can be drawn if the viscosity of the sol is carefully controlled. The sol-gel process involves the transition of a colloidal suspension, or *sol*, to an inorganic liquid network phase, or *gel*. An overview of the sol-gel process is presented in Figure 3.1.

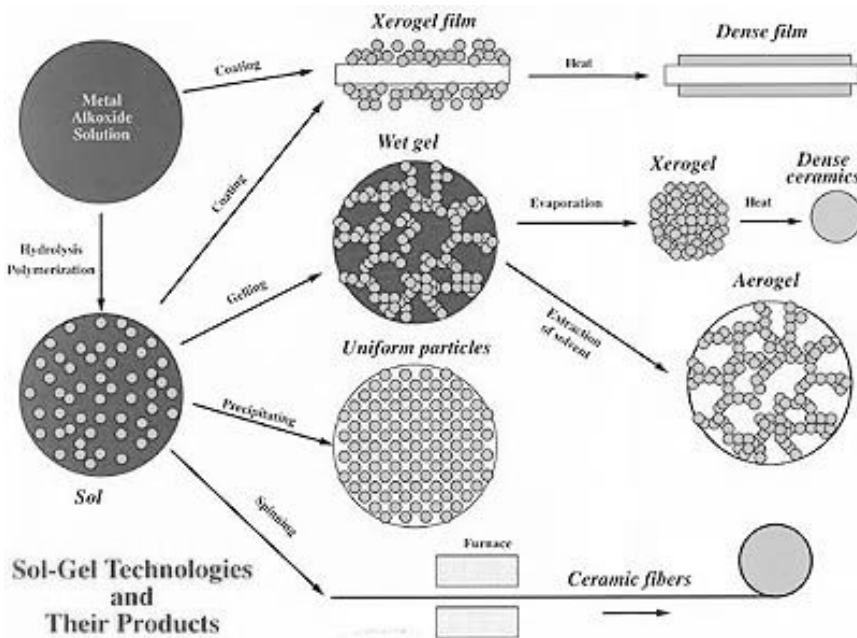


Figure: Sol gel processing and products ^[3]

For metal nitrate precursor materials, the Pechini method is used.^[4] In this method, an aqueous solution is prepared in citric acid. The ratio of metal ions can be precisely controlled to obtain the desired mixed oxide material. The acid complexes with the metal ions. Ethylene glycol is added and the solution is heated to 150-250 °C to remove excess water resulting in a cross-linked polymer gel. The cross-linked polymer mass is then heated further and forms a hard cross-linked polymeric solid. The polymeric solid is then charred at around 400 °C. The temperature is increased to 500-900 °C to form crystallites of the mixed oxide composition. The crystallites are typically 20-50 nm and clustered into agglomerates.

3.1.2.2 Sol gel synthesis of LSC

$(La_{0.8} Sr_{0.2})CoO_3$ (LSC) powder was synthesised via a sol-gel process based on the Pechini method.^[4] Lanthanum nitrate ($La(NO_3)_3 \cdot 6H_2O$), strontium nitrate ($Sr(NO_3)_2$), and cobalt nitrate ($Co(NO_3)_3 \cdot 6H_2O$) precursors were used. The precursors were weighed out in the appropriate stoichiometric ratios on electronic scales and then dissolved in distilled water at 90 °C. Once the nitrate materials had completely dissolved, citric acid and ethylene glycol were added to act as complexing agents. The solution was refluxed for 24 hours at 90-100 °C. After refluxing, the solution was dried at 150 °C for 6 hours, resulting in a fine powder. The powder was ground using an agate mortar and pestle, to break up any agglomerates, and then further heat-treated in an alumina crucible. The heat treatment after drying was carried out in a muffle furnace ramping from 50→1000 °C, with 2-hour dwells at 600 °C, 800 °C, and 1000 °C. Small samples were taken at each dwell temperature for X-Ray analysis. Figure 3.2 shows the flow diagram for the sol-gel synthesis of LSCo powder. After cooling, the heat-treated powder was ground in a mortar and pestle for approximately 20 minutes to break up agglomerates and to refine the powder size.

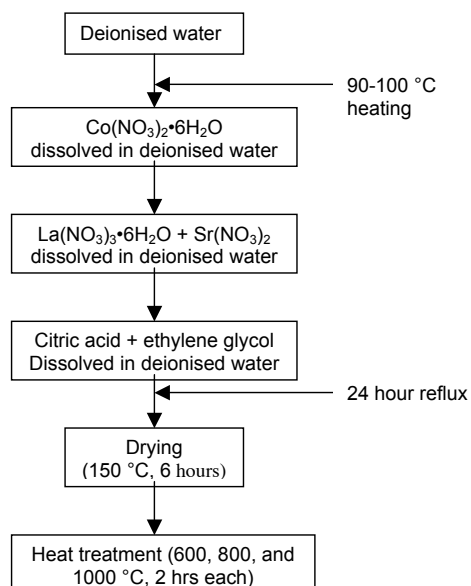


Figure 3.2: Flow chart of the sol-gel powder synthesis route

3.1.3 Pellet Preparation

YSZ powder was uniaxially pressed at a pressure of approximately 2 tons/cm², using 23-mm discs in stainless steel pellet dies to form pellets. The appropriate mass of powder was weighed out on an electronic balance and placed in the die. A small depression in the centre of the powder was formed prior to pressing to avoid uneven compaction due to friction between the powder and the die walls. Uneven compaction of the powder can cause cracks and internal fracture in the sintered pellet. The pellets were placed on a flat alumina support plate and then sintered in a muffle furnace at 1500 °C for 6-12 hours to form dense discs.^[5]

3.1.4 Screen Printing

3.1.4.1 Process description

Screen printing is a thick film technique for applying a material in a pattern on a flat substrate. The material to be printed is ground and sieved to a fine powder and then suspended in an ink vehicle. Powders are typically finer than 10 µm. Powder-ink mixtures must be well milled and mixed to produce a homogeneous dispersion. A fine mesh attached under tension is coated with an emulsion, masking out the image to be printed. A flexible blade is then drawn across the mesh, forcing the ink through the open areas of the emulsion, creating an image on the substrate. The printed substrate is then dried followed by heat treatment to burn out the organic solvents leaving a ceramic particle network, which can then be sintered to the desired density. Prior to heat treatment, further layers may be printed to achieve a thicker final film. Each layer must be dried before the next layer is added to prevent smearing the image.^[2]

3.1.4.2 Screen printed electrode films

The sol-gel prepared LSC powder and commercial powders of LSM and LSF were screen-printed on YSZ electrode discs. The powder was ground by hand in a mortar and pestle with acetone for 30 minutes. The powder was then wet sieved through a 10 µm nylon mesh with acetone. The oversized material was reground and sieved again. The <10 µm powder was combined with an ink vehicle, turpentine, and acetone in a ratio of

70/30/30 wt % and mixed by hand. The mixture was allowed to sit while the acetone evaporated. The prepared ink was then printed on YSZ substrate through a nylon printing screen. The printed sample discs were allowed to air dry for 20 minutes and then placed in a drying oven at 80 °C for 3 hours. The dried samples were then heat treated to remove the organic material. This heat treatment consisted of heating from 50→1000 °C at a rate of 1 °C/min., then holding at 1000 °C for 3 hours, and cooling to 50 °C at a rate of 5 °C/min. The samples were then fired at high temperature for 3-5 hours to sinter the electrode layer. The sintering temperature was between 1150 °C and 1250 °C depending on the electrode material. Figure 3.3 shows the processing route for screen-printing of electrode material on YSZ.

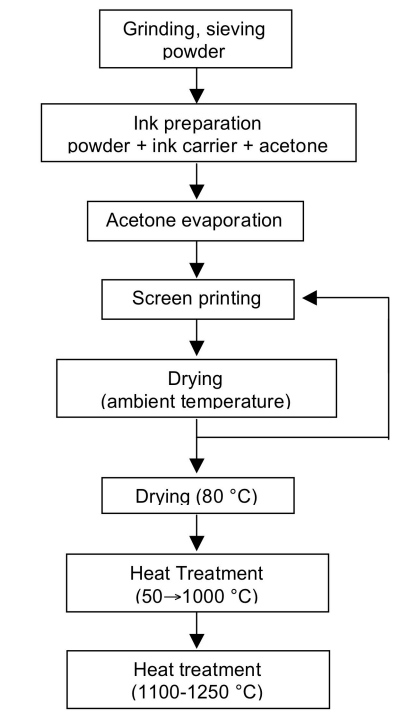


Figure 3.3: Flow chart for the screen-printing of thick film electrode materials

3.1.5 Spin-coating

Spin coating is a common chemical solution deposition (CSD) technique. A suitable coating solution is prepared from precursors according to the desired film composition. The coating solution is deposited onto a substrate fixed to a spinning plate, followed by heat treatment.^[6] A protective ceria layer was deposited onto YSZ electrolyte discs to prevent interface reactions between the YSZ and the screen printed anode materials. The ceria coating was an acid solution consisting of acetic acid and Ce 2-ethylhexanoate. The solution was mixed for 2 hours at 80 °C prior to spin coating at 3000 rpm for 20 sec. The coated substrate was dried at 100 °C for 20 minutes then heat-treated at 650 °C for 2 hours. The spin coating, drying, and heat treatment steps were repeated six times to build up the coating. The coated substrate had a final heat treatment at 1300 °C for 6 hours to sinter the ceria layer.

3.1.6 Tape Casting

3.1.6.1 Process description

Tape casting, also known as doctor blading, is used in many materials industries, such as ceramics, paper, plastics, and paint manufacture. The technique produces thin, flat ceramic parts with a large surface area. These parts would be impossible to press using standard ceramic pressing techniques and would be difficult to extrude. Tape casting allows for the fabrication of complex flat parts, because holes and slots are easily punched out from the green (unfired) tape. Tape dimensions are generally large in the x and y directions, on the order of centimetres to meters thick, and very thin in the z direction, on the order of microns to millimetres thick. The basic tape casting system is comprised of three components: a stationary doctor blade, a moving carrier surface, and a drying zone. A general schematic of a tape casting system is shown in Figure 3.4. The slip or slurry is a fluid suspension of ceramic, metallic, or composite particles suspended in a solvent. The carrier is generally a polymer film, but can also be made of metal, glass, or stone. The doctor blade scrapes the excess material from the moving carrier surface and can be fabricated in a variety of shapes and sizes to control the final product. The slurry is poured into the reservoir behind the doctor blade, and then the carrier is set in

motion. The slurry is spread on the carrier surface and dried to form a green tape. The main process parameters that can be controlled include doctor blade gap, reservoir depth, carrier speed, slurry viscosity, and doctor blade shape. The doctor blade gap is the space between the blade and the carrier surface.^[7]

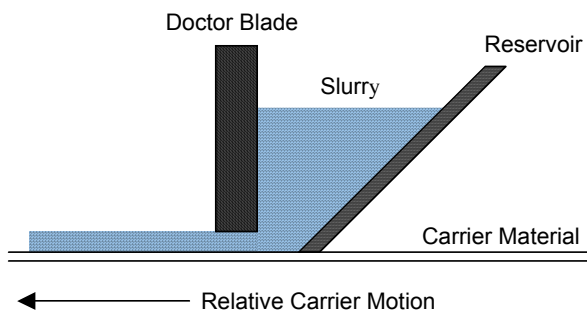


Figure 3.4: Schematic of the tape casting process

The slurry composition is a critical parameter in the final product. The slurry is comprised of ceramic, metal, or composite powder, along with solvent(s), dispersants, binders, and plasticizers. These ingredients are added to make a slurry recipe appropriate for the fabrication of the desired shape and green density of the final part. The solvent, sometimes called the vehicle, can be one or more solvent in which the powder is suspended. The solvent(s) must distribute the powder and additives uniformly, dissolve the other ingredients, and evaporate quickly. Ethanol, toluene, and methyl ethyl ketone are all examples of typical solvents used in tape casting. The dispersant is used to keep the particles apart and increase the solids loading in the suspension. Dispersants also decrease the amount of solvent needed to ensure the slip dries faster with less shrinkage. Some typical dispersants used are citric acid, stearic acid, and linoleic acid. The binder is the polymer matrix that holds the ceramic powers, and this binder can be vinyl, acrylics, or cellulose. Plasticizers increase the flexibility and plasticity of the green tape to allow the tape to be rolled and to enable parts to be stamped out of the tape without breakage. Typical plasticizers are phthalates or glycols.^[7]

3.1.6.2 Tape cast tube processing

The electrolysis tubes were made from tape cast materials with subsequent fabrication and forming into tubes followed by heat treatment and sintering.^[8] The tapes used in the tubes were made with a laboratory scale tape caster (Mistler, Inc. TTC-1000). The green tapes of YSZ electrolyte, LSM anode current collector, LSM+YSZ active anode, and NiO+YSZ active cathode materials were made from slurry with around 57% solids loading and a viscosity at 20 rpm of 3000-3250 centipoise. The components of the slurries were as follows:

Ceramic powders:	YSZ, LSM, LSM+YSZ, NiO+YSZ
Solvents:	Methyl ethyl ketone, ethanol
Dispersant:	Trinton
Plasticizers:	Di-n-butyl phthalate, polyethylene glycol
Binder:	Butvar

Each slurry was thoroughly mixed in a ball mill for a total of 36 hours. The tapes were then cast individually, allowing for ample drying time. The green tape thicknesses for each material are presented in Table 3.1. Some tapes were made at roughly half the thickness of the standard tapes, these tape thicknesses are also included in Table 3.1. The purpose of the thin tapes will be discussed further in section 5.2.5.

Table 3.1: Green tape thicknesses for tube component materials

Material	Standard tape thickness (mm)	Thin tape thickness (mm)
LSM	0.6	0.3
LSM+YSZ	0.7	0.3
YSZ	0.7	0.35
NiO+YSZ	0.7	0.3

3.1.7 Electrolysis Tube Fabrication

3.1.7.1 Rolling

Green tapes were prepared for tube fabrication. The tapes were cut to the appropriate size as follows:

LSM:	5 cm x 14 cm
LSM+YSZ:	5 cm x 2.2 cm
YSZ:	5.5 cm x 6 cm
NiO+YSZ:	4.5 cm x 2.5 cm

The cut tapes were then rolled using a brass rod as a former. Figure 3.5 shows a schematic of the green tapes and a rolled tube.

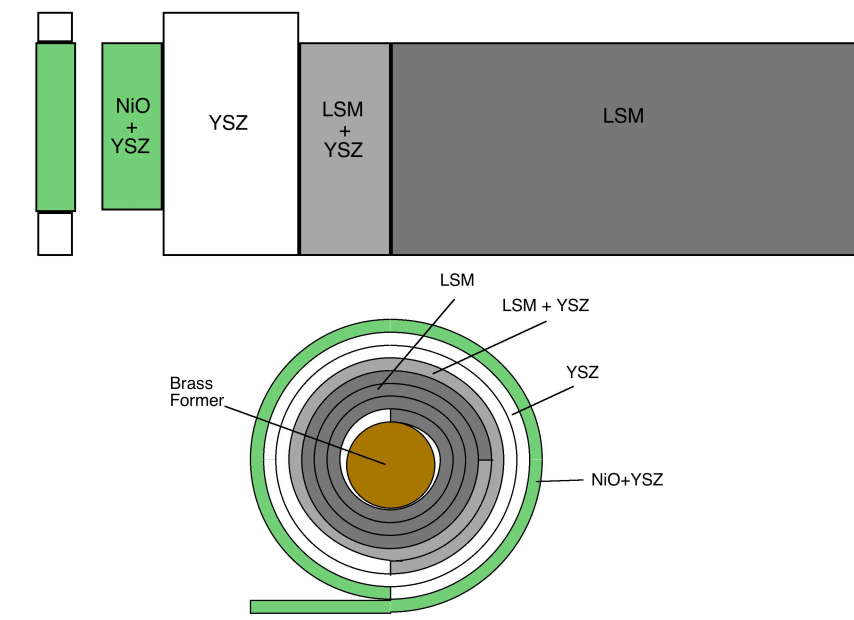


Figure 3.5: Tube cell fabrication from green tapes

3.1.7.2 Cold isostatic pressing

Cold isostatic pressing (CIP) uses the hydrodynamic forces through a liquid media to apply stress to a green ceramic form in all directions.^[9] For tube fabrication, the pressure vessel is filled with oil, the tube is placed inside, and the vessel is pressurized to 235 MPa. This step compacts the tape layers in the green tube and relieves stresses found at

the seams between tapes. CIP also seemed to aid in densification of the YSZ electrolyte layer.

3.1.7.3 Heat treatment and sintering

The green tubes were heat treated with binder burnout and sintering steps according to the following:

	Heating rate:	Temperature:	Dwell time:
Binder burnout (fast):	0.5 °C/min	1000 °C	5 hours
Binder burnout (slow):	0.1 °C/min	1000 °C	2 hours
Sintering:	5 °C/min	1350 °C	5 hours

The final dimensions of a sintered tube are approximately 9 mm long, 5.4 mm outside diameter, and 3.4 mm inside diameter.

3.2 Electrochemical Testing

3.2.1 Electrolysis pellet cell testing

Three-probe pellet cells were prepared for impedance measurement and electrolysis tests. The YSZ pellets were prepared as described in section 3.1.3, and subsequently screen-printed with the electrode material as described in section 3.4.1. The prepared pellets then had a thin platinum layer added onto each side to provide electrical contact for the working, counter and reference electrodes as shown in Figure 3.6. Each side of the pellet was coated with platinum paste and dried in an oven at 80 °C for 2 hours. After drying the pellets were heat treated to remove the organic binder from the paste. The heat treatment consisted of heating from 50→900 °C at a rate of 5 °C/min., holding at 900 °C for 1 hour, and then cooling back down to 50 °C

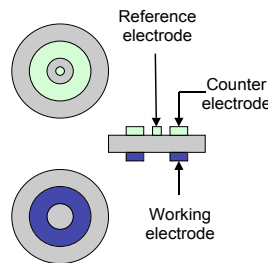


Figure 3.6: Electrode configuration on YSZ electrolysis pellets

It was necessary to design and fabricate an apparatus for the electrolysis measurements as well as AC impedance on the pellet samples. The testing required controlled atmospheres at both electrode surfaces and temperatures up to 950 °C. The apparatus or test jig was constructed out of custom-made alumina cylinders (CoorsTek, Inc.) with boreholes for gas circulation and electrode access. The reference and counter electrodes were fabricated from single-bore alumina tubing with Pt wire contact material. The working electrode was fabricated from 4-bore alumina tubing with Pt-wire electrical contact as well as a Pt/Rh thermocouple wire to allow for temperature measurement as close to the electrolysis cell as possible. Figure 3.7 shows schematically the electrolysis test apparatus. The gas inlet for the cathode side of the reaction was routed through a steam generator to control the gas atmosphere. The steam generator consisted of a gas bubbler

in water surrounded by a heating mantle set at the temperature required for the desired amount of steam, generally room temperature for 3%steam, and 80 °C for 50% steam in the gas inlet. The gas for the anode side of the reaction was first dried in a drying column filled with silica gel, then bubbled through an ice bath maintained at 0 °C. Bubbling through the ice bath maintained a known amount of oxygen present in inlet gas. At 0°C the water vapour pressure is 0.006 atm. The oxygen partial pressure was required for the calculations used with the oxygen sensor connected to the gas outlet of the anode side. The outlet from the cathode side was not collected or analysed, as the required equipment for gas analysis was not available to measure the amount of hydrogen produced during electrolysis. Instead, the amount of oxygen produced was measured on the anode side by means of an oxygen sensor. The prepared electrolysis pellet was then sealed in the testing jig with gold rings. The electrodes were connected to a Solartron SI 1287 Electrochemical Interface for electrolysis performance measurements and a Solartron SI 1255 Frequency Response Analyser for impedance measurements.

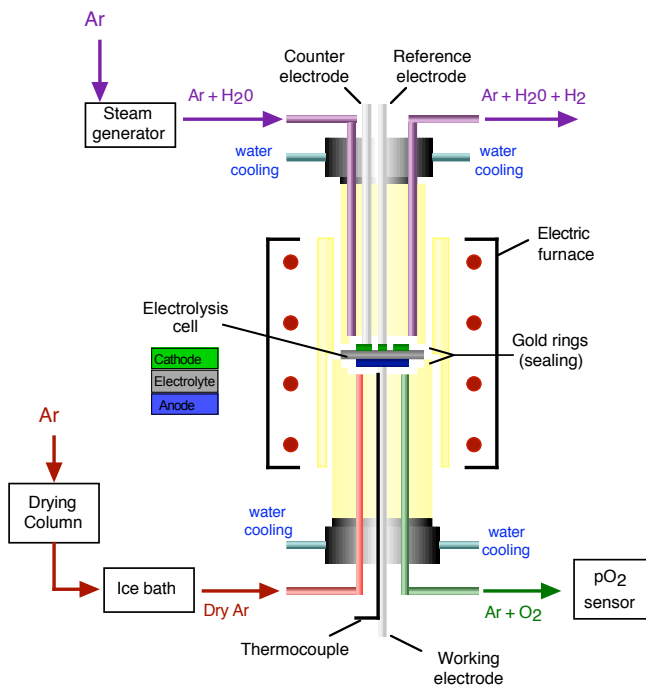


Figure 3.7: Electrolysis cell test apparatus for pellet cells

3.2.2 Electrolysis tube cell testing

The electrolysis tubes were prepared for testing by attaching and sealing to a 3 mm-diameter steel tube used as a gas inlet as well as the anode electrical contact. Silver paste was painted on the outer surface of the end of the steel tube, approximately 5 mm from the end. The steel tube was then carefully inserted into the electrolysis tube to a distance of approximately 5 mm. Attention was paid to ensure the silver paint did not leak out to the outer surface of the electrolysis tube. The tube assembly was then heat treated to 200 °C to cure the silver paint and remove the organics. Several layers of YSZ slurry was then applied to the join between the electrolysis tube and the steel tube, allowing for air-drying between layers. A final coat of ceramic cement (Ceramabond 552) was applied over the dried YSZ slurry to provide mechanical support. The tube assembly was then heat treated to 700 C to cure the YSZ slurry and the ceramic cement. After sealing the tube assembly was attached to a compressed air tap then submersed in water to check the seal and the tube itself for cracks. Ni mesh (United Wire) was wrapped around the ceramic tube and connected to the alligator clip with Ni wire for the cathode electrical contact. A cannular

tube was inserted inside the steel tube to provide proper gas flow. The tube assembly was placed in the test apparatus as illustrated in Figure 3.8. The test apparatus for tube testing was fabricated from a quartz tube with Teflon end caps. The tube assembly, as well as gas inlets and outlets, and a K-type thermocouple were fixed into the end caps. The thermocouple was placed as close to the electrolysis tube as possible. The gas streams for the tube testing were routed exactly as for the pellet testing.

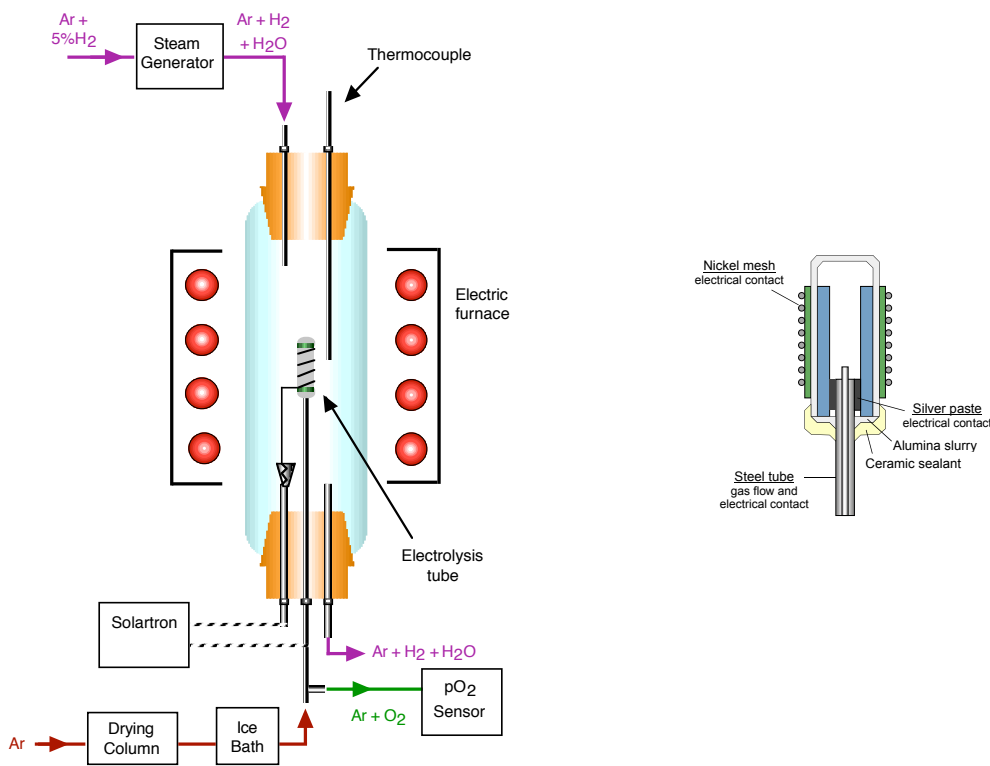


Figure 3.8: Electrolysis tube test apparatus and detail of the tube assembly

An alternate tube assembly was fabricated out of a 4-bore alumina tube with an outside diameter of 3 mm. The alumina tube replaced the stainless steel tube shown in Figure 3.8. This alternate assembly, shown in Figure 3.9, was used to try to eliminate some of the problems found in using stainless steel. A platinum wire was threaded through one of the boreholes in the alumina tube and then wrapped around the top to serve as electrical contact with the electrolysis tube. A brass manifold was machined and glued into place connecting to one borehole for a gas inlet. The gas outlet manifold connected to the remaining two boreholes. The gas inlet and outlet manifolds had brass metal fittings to

allow easy connection to lab gas supply. The alumina tube was inserted into the end of the electrolysis tube; using a small amount of platinum paste to ensure good contact with the platinum wire. The alumina tube assembly was sealed in the same manner as the standard steel tube assembly, omitting the silver paste.

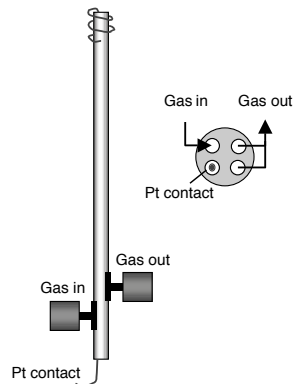


Figure 3.9: Alternate tube assembly; 4-bore alumina tube with Pt contact and brass manifold for gas inlet and outlet

3.2.3 Oxygen sensor

The oxygen sensor consists of a YSZ ceramic tube closed on one end, with porous platinum electrodes, coated on both the inner and outer surfaces of the closed end. The tube is held in a quartz tube inside an electric furnace. Figure 3.10 shows a schematic of the oxygen sensor.

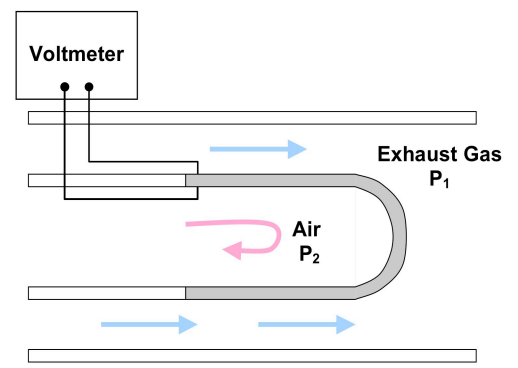


Figure 3.10: Schematic of a YSZ oxygen sensor

As the sensor is heated to a high temperature, above 600 °C, it becomes permeable to oxygen ions and vacancies in its crystal lattice permit the mobility of oxygen ions. The platinum electrodes on each side of the sensor provide a catalytic surface for the change of oxygen molecules to oxygen ions and oxygen ions to oxygen molecules. Oxygen molecules, on the high concentration reference gas side of the cell, gain electrons to become ions that enter the electrolyte. Simultaneously, at the other electrode, oxygen ions lose electrons and are released from the surface of the electrode as oxygen molecules. When the concentration of oxygen is different on each side of the cell, oxygen ions will migrate from the high oxygen concentration side to the low oxygen concentration side. This ion flow produces an electronic imbalance that results in a voltage potential between electrodes that is a function of the temperature of the cell and the ratio of oxygen partial pressures on each side of the cell. The relationships between the oxygen concentration of the unknown gas, the oxygen concentration of the reference gas (typically air, at 20.95% oxygen by volume), and the temperature, voltage output, and cell constant of the fuel cell sensor is defined by the Nernst Equation, as given by the following:

$$E = \frac{RT}{nF} \ln\left(\frac{P_1}{P_2}\right) \quad (3.25)$$

where E is the sensor voltage, R is the gas constant, T is the temperature of the sensor, n is the number of charges ($n=4$ for oxygen), F is the Faraday constant, and P_1 and P_2 are the oxygen partial pressures on the inner and outer side of the sensor. In this case P_1 refers to ambient air, and P_2 is the unknown oxygen partial pressure from the electrolysis cell outlet.^[10] The sensor temperature for all experiments was 800 °C. Table 3.2 gives examples of oxygen sensor voltage for various exhaust gases, P_2 , versus air, P_1 , at a sensor temperature of 800 °C.

Table 3.2: Oxygen sensor voltage for various gases according to the Nernst equation.

Gas	Partial pressure of O ₂ in gas	Voltage (mV)
Air	0.209	0
Oxygen	1.0	-37
Argon	3.65x10 ⁻⁵	200
5% H ₂ in Argon	2.57x10 ⁻¹⁸	900

3.3 AC Impedance Spectroscopy

AC impedance spectroscopy is a powerful method for characterization of the electrical properties of materials and interfaces. This method can be used to investigate the dynamics of charge movement in the bulk and interfacial regions of any kind of solid or liquid material: ionic, semiconducting, mixed electronic-ionic, and insulators. AC impedance spectroscopy is a common method for characterizing the polycrystalline materials used in solid oxide fuel cells.

3.3.1 Theory

When a current, I , with potential, V , is applied across a material in a DC circuit, the resistance to the flow of electrical current, R , follows Ohm's law as given by:

$$R = \frac{V}{I} \quad (3.4)$$

In an AC circuit, the voltage and current follow a sinusoidal path with respect to time. The voltage and current signals as a function of time can be expressed as the following:

$$V = V_o \sin \omega t \quad (3.5)$$

and

$$I = I_o \sin \omega t \quad (3.6)$$

where V_o and I_o are the amplitudes of the two signals. The angular frequency, ω , is the frequency of the applied alternating current; t is the time for one cycle of the sinusoidal oscillation of the applied current. Angular frequency, with the units of radians/second, is related to frequency, f , in hertz by the following:

$$\omega = 2\pi f \quad (3.7)$$

In AC circuits, the total resistance to current flow is described as impedance, Z . For metallic materials, the voltage and current are in phase, and impedance is proportional to the resistance. However, in polycrystalline solids such as metal oxides, the impedance has resistive as well as capacitive elements. The current flow in the system depends on the ohmic resistance of the electrodes, electrolyte, and the electrode-electrolyte interface; the

flow can be further impeded by grain boundaries, second phases, and defects in the bulk materials. The oscillation of the voltage in an AC circuit allows the elements that make up the total impedance to be separated and measured.

The impedance of a polycrystalline sample varies with the applied voltage frequency. To analyse the impedance complex numbers can be used. Complex numbers consist of a real and an imaginary term. The complex number a can be expressed as the following:

$$a = x + iy \quad (\text{Cartesian}) \quad (3.8)$$

$$a = r(\cos \theta + i \sin \theta) \quad (\text{Polar}) \quad (3.9)$$

where x and $r \cos \theta$ represent the real terms; y and $r \sin \theta$ are the imaginary terms respectively; and i is $\sqrt{-1}$. From deMoirre's theorem, the polar form may be written as an exponential term as follows:

$$a = re^{i\theta} \quad (3.10)$$

The complex number, a , is represented graphically in Figure 3.11.

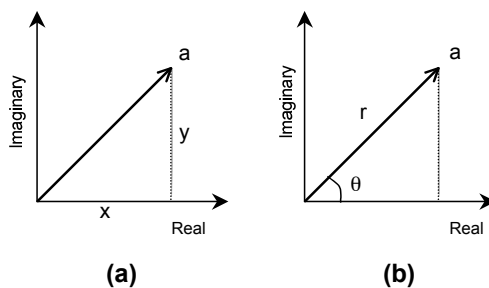


Figure 3.11: Complex number in (a) Cartesian and (b) polar coordinate systems.

Impedance can be expressed in complex form as the following:

$$Z^* = Z' + iZ'' \quad (3.11)$$

Z^* is referred to as the *complex impedance*, Z' is the real impedance, and Z'' is the imaginary impedance. The real impedance represents the component in phase with the applied sinusoidal voltage and can be associated with resistive behaviour of the current in

the circuit. The imaginary impedance represents the component 90° out of phase with the voltage and can be associated with capacitive behaviour of the current.

There are several ways to evaluate impedance of an electrochemical circuit. The impedance as a function of frequency is resolved into its component real and imaginary components, Z' and Z'' . A plot of Z' against $\log \omega$ or Z'' against $\log \omega$, known as Bode plots, may be constructed. Each of the plots will have a characteristic shape that can be related to different electrochemical aspects of the sample. Another useful plot is the Cole-Cole plot, which is a plot of Z' against Z'' at each measured frequency. A more detailed description of Cole-Cole plots can be found in the following section. ^[11,12,13]

3.3.2 Equivalent circuits

The individual elements that comprise the total impedance for a sample can be approximated by the use of an equivalent circuit. The resistive (real) and capacitive (imaginary) elements can be thought of as a resistor and capacitor connected in parallel, as illustrated in Figure 3.12.

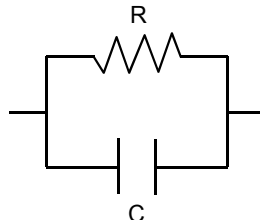


Figure 3.12: Resistor and capacitor in parallel

The impedance of a resistor is simply the resistance, thus:

$$Z' = R \quad (3.12)$$

Unlike a resistor, which simply resists the flow of current, a capacitor is a charge storage device. In the presence of an electric field, ionic solids will undergo a polarisation, which will make the material store a charge, Q , in the same manner as a capacitor. The capacitance, C , is given by the following relationship:

$$C = \frac{Q}{V} \quad (3.13)$$

Current is the derivative of charge with respect to time:

$$I = \frac{dQ}{dt} \quad (3.14)$$

thus the current becomes:

$$I = \omega CV_o \cos \omega t \quad (3.15)$$

For a capacitor the impedance then becomes:

$$Z'' = \frac{V_o \sin \omega t}{\omega CV_o \cos \omega t} \quad (3.16)$$

Using the relationship (3.11), equation (3.16) can be rewritten as the following:

$$Z'' = \frac{1}{i\omega C} \quad (3.17)$$

The total impedance response of a material is a function of the applied frequency. At high frequency, the resistive impedance dominates; and at low frequency, the capacitive impedance dominates. At intermediate frequencies, the behaviour will be a mixture of resistive and capacitive, and the current will be out of phase with the voltage by a value between 0 and $\pi/2$ radians (90°), known as the phase angle, ϕ . The phase angle depends on the frequency, as $\omega \rightarrow 0$, then $\phi \rightarrow \pi/2$ radians, and as $\omega \rightarrow \infty$, then $\phi \rightarrow 0$.

With the use of a frequency response analyser, the change in phase angle with frequency can be measured. This allows the real and imaginary terms of the impedance to be determined through a range of frequencies. A complex impedance or Cole-Cole plot can be constructed from the resulting data. Z^* is resolved into two components measured at each frequency, with Z' as the ordinate and Z'' as abscissa. The plot generally takes the shape of a semicircle, as shown in Figure 3.13. The semicircle plots provide estimates of resistive and capacitive parameters of the sample, which can then lead to estimates of the conductivity. Measured data rarely give a full semicircle with its centre on the real axis, often there will be some deviation from the perfect semicircle. These deviations provide information concerning the electrode processes

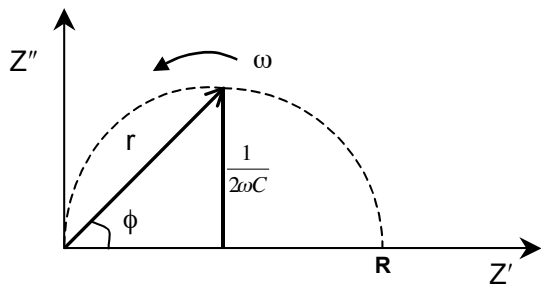


Figure 3.13: Complex impedance plot

To analyse and interpret impedance data, it is essential to have a model equivalent circuit that provides a realistic representation of the electrical properties. A polycrystalline ceramic material will contain several components, such as bulk and grain boundary regions; each of these components may be represented by a resistor and a capacitor placed in parallel, and, depending on the properties of the material, different combinations will apply. Additional features, such as surface layers, can be described in most cases by placing additional RC elements in series.

An equivalent circuit described by parallel RC elements connected in series leads to a complex impedance diagram generally composed of several capacitive arcs. A complex impedance plot and the equivalent circuit associated with the bulk and grain boundary regions of a polycrystalline ceramic are shown in Figure 3.14.

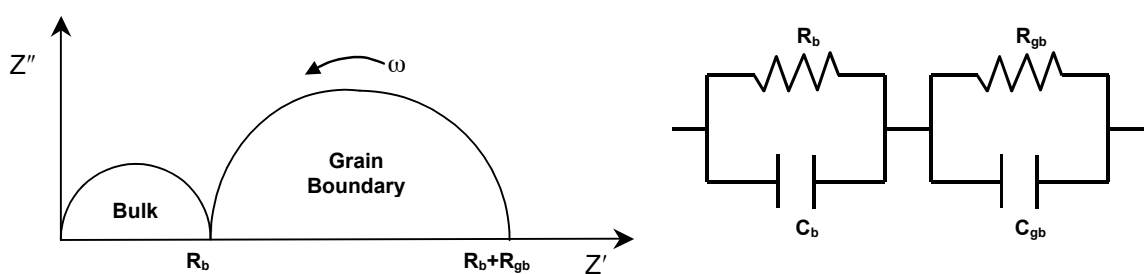


Figure 3.14: Complex impedance plot and equivalent circuit diagram of bulk and grain boundary response

The total complex impedance is given by:

$$Z' = \frac{R}{1 + (\omega RC)^2} \quad \text{and} \quad Z'' = \frac{R(\omega RC)}{1 + (\omega RC)^2} \quad (3.18) \quad (3.19)$$

When $\omega RC = 1$, a maximum in Z'' is obtained and at this point $Z' = Z'' = R/2$. The resistance and capacitance of the unknown component can be determined. The capacitance is calculated from the equation:

$$C = \frac{1}{\omega_o R} \quad (3.20)$$

where ω_o is the angular frequency at the maximum Z'' . The angular frequency at which Z' is equal to Z'' allows the capacitance of each element to be determined and assigned to the different regions of the sample.^[11,11]

3.4 Electron Microscopy

3.4.1 Scanning Electron Microscopy (SEM)

Scanning electron microscopy (SEM) is a surface technique for analysing the topography, morphology, and composition of bulk samples. An SEM consists of a vacuum chamber with an electron gun, several electromagnetic lenses, sample chamber and one or more electron detectors. Figure 3.15 shows a schematic of a typical SEM. The filament in the electron gun produces an electron beam, which is focused through a series of condenser and objective lenses into a spot less than 4 nm on the sample. The beam is scanned in a rectangular raster over the sample. When the incident electron beam strikes the sample several interactions take place. Some examples of these interactions are illustrated in Figure 3.16.^[14]

The various electron beam interactions with the sample have different uses. For SEM the secondary electrons are used for imaging. When an incident electron passes near an atom in the sample, this causes a slight energy loss and path change in the incident electron and the ionization of an electron (usually from the K shell) in the sample atom. The ionized electron leaves the atom with a very small energy (5 eV) this is a secondary electron. A detector collects the secondary electrons, and then the signal is amplified to cause the brightness of the electron beam in a cathode ray tube (CRT) to vary. Both the incident beam and the CRT are scanned at the same rate so there is a one to one relationship between each point on the CRT and on the sample, thus an image is built up. Due to their low energy only secondary electrons very near the surface (<10nm) can exit the sample.

Any changes in topography in the sample that are larger than this sampling depth will change the yield of secondary electrons, which corresponds to surface roughness viewed on the image. The ratio of the size of the viewing screen to the area scanned on the sample is the magnification. Increasing the magnification is achieved by reducing the size of the area scanned.

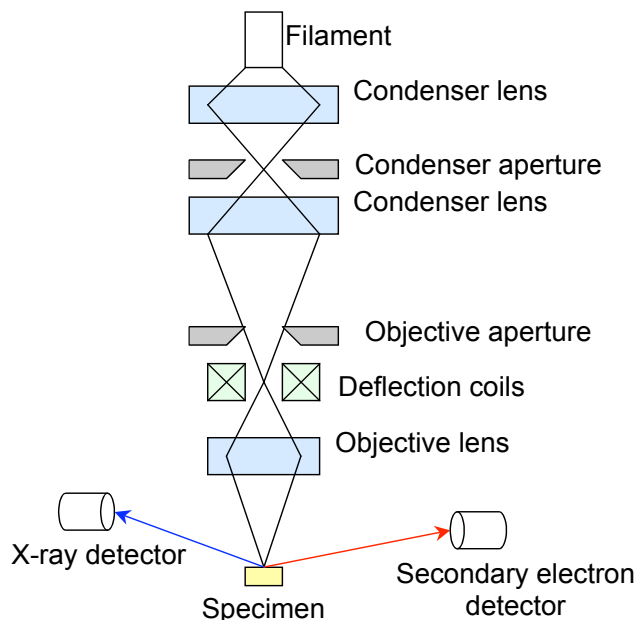


Figure 3.15: Schematic of a typical SEM. The incident electron beam is shown in black, secondary electrons in red, and x-rays in blue.

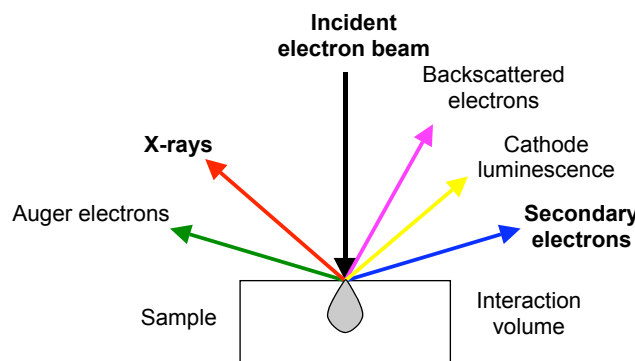


Figure 3.16: Bulk sample interactions from incident electron beam.

Back-scattered electrons are produced when an incident electron collides with an atom in the sample and is scattered back 180 degrees. The production of backscattered electrons varies directly with the atomic number of the elements in the sample. The differing production rates cause higher atomic number elements appear brighter than lower atomic number elements in the corresponding SEM image.

Auger electrons are caused when a secondary electron is produced. When the secondary electron is emitted from the atom at a low shell, a vacancy is left. A higher energy electron from the atom drops to a lower energy, filling the vacancy. This creates an energy surplus in the atom, which is corrected by the emission of an Auger electron. Auger electrons have a low energy and are only emitted from the sample from a depth of less than 3 nm. Auger electrons have a characteristic energy, unique to each element and can give compositional information about the sample.

The interaction volume is the volume inside the sample in which interactions from the electron beam occur. Figure 3.17 shows a schematic of the interaction volume for the various electron beam-specimen interactions. This volume depends on several factors. In general the higher atomic number materials absorb more electrons so have a smaller interaction volume. Higher accelerating voltages used in the SEM penetrate further into the sample and generate a larger interaction volume. The angle at which the electron beam strikes the sample will cause a smaller interaction volume as it deviates from perpendicular. Beam electrons lose energy as they traverse the sample due to interactions with the sample and if too much energy is required to produce an effect, it will not be possible to produce the effect from deeper portions of the volume. The degree to which an effect, once produced, can be observed is controlled by how strongly the effect is diminished by absorption and scattering in the sample.

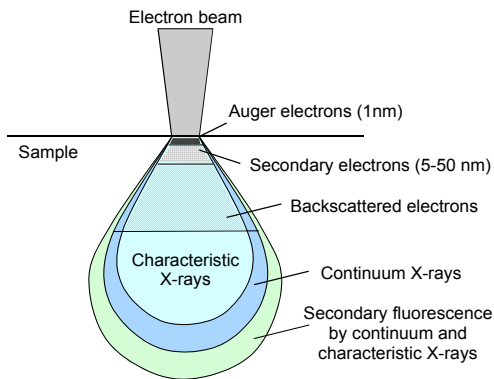


Figure 3.17: Illustration of interaction volumes for various electron-specimen interactions ^[14]

3.4.2 Electron Dispersive Spectroscopy (EDS)

An electron beam will interact with a material and cause the emission of characteristic x-rays from the sample. These x-rays are collected by a detector and sorted to yield compositional information about the sample. This technique is called Electron Dispersive Spectroscopy (EDS) or Energy Dispersive X-ray (EDX). EDS allows element maps to be constructed of selected areas on the sample surface. The element maps show the distribution of specific elements in the sample region scanned. This is especially useful when analysing interfaces and multiple-phase regions.

3.4.3 Characteristic X-Ray Spectrum

X-rays have wavelengths from approximately 0.1 to 100 Å. Because the wavelength of x-rays is comparable to the size of atoms, they are ideally suited for investigating the structural arrangement of atoms and molecules in a wide range of materials. The wavelengths used in crystallography range between 0.5 and 2.5 Å, which is of the order of magnitude of interatomic distances observed in most materials. X-rays are generated from the impact of high-energy electrons with a metal target, or anode. The electron beam ejects an electron from one of the metal core orbitals. An electron from a higher energy orbital in the metal will replace the ejected electron and emit radiation. A schematic of a typical x-ray emission spectrum is shown in Figure 3.18.

The x-ray spectrum consists of several intense peaks, referred to as characteristic peaks, and a continuous background, known as white radiation or *bremssstrahlung*. The background is generated by the deceleration of the incident electrons and is generally undesirable for the analysis of x-ray diffraction data. The characteristic peaks result from the transitions of upper level electrons to vacancy left by the ejected electron in lower energy levels. The characteristic peaks correspond to the energy of the various transitions and are element-specific; therefore, each element emits a characteristic distribution of wavelengths. The characteristic peaks are labelled with respect to the electron shells involved in producing the x-ray. Transitions from *L* and *M* shells to the *K* shell are designated $K\alpha$ and $K\beta$, respectively. The transition from the *M* shell to the *L* shell is designated $L\alpha$. *K* corresponds to the electron shell with principle quantum number $n = 1$, *L* to $n = 2$, and *M* to $n = 3$. These transitions are illustrated in Figure 3.19.

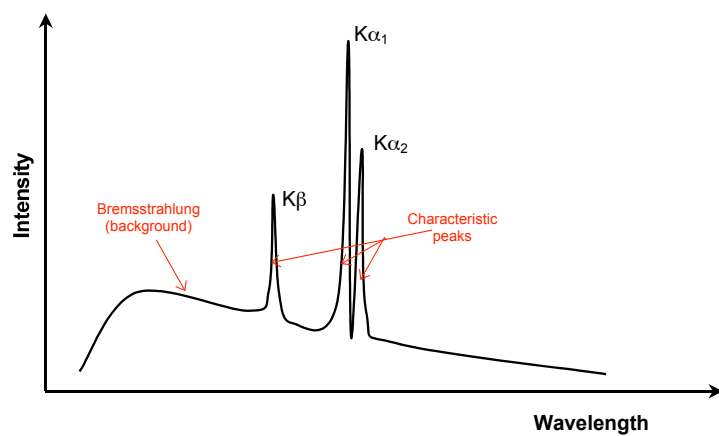


Figure 3.18: Typical x-ray emission spectrum schematic

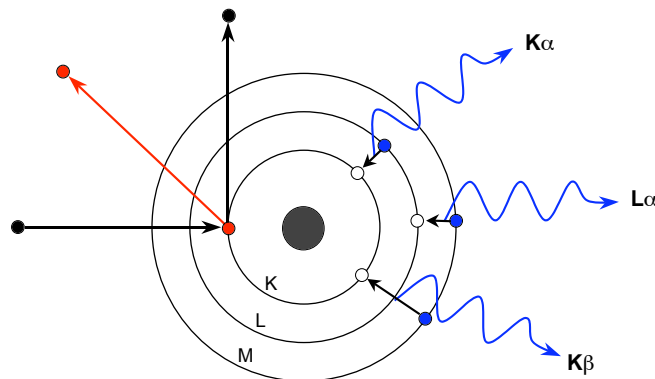


Figure 3.19: Schematic showing an incident electron (black) ejecting a core electron (red) and the electron decay (blue) from higher energy levels to fill the vacancy in the lower energy level and the corresponding characteristic x-rays produced.

The $K\alpha$ component consists of two peaks, designated $K\alpha_1$ and $K\alpha_2$, which correspond to $2p_{1/2} \rightarrow 1s$ and $2p_{3/2} \rightarrow 1s$ transitions, respectively. The terms s and p refer to the corresponding orbitals, and the subscripts 1/2 and 3/2 are the total angular momentum quantum number. Figure 3.20 illustrates these transitions schematically. The $K\beta$ component also consists of two peaks, $K\beta_1$ and $K\beta_2$; they are quite close to one another and are generally not distinguished from one another. Additional characteristic peaks exist in the emission spectrum, $L\alpha-\gamma$ and $M\alpha-\xi$; these peaks are practically indistinguishable in the x-ray spectra of many anode materials.

For diffraction a single x-ray wavelength is desired. Additional characteristic wavelengths and the background radiation are undesirable because they increase the noise in the data. A monochromatic x-ray beam is obtained by reducing the intensity of the background and eliminating the unwanted peaks. The most common method for monochromatization of x-ray beams is using a filter, which absorbs the unwanted peaks. The filter material selectively absorbs the $K\beta$ radiation and transmits the $K\alpha$ parts of the x-ray spectrum, as shown in Figure 3.21, where the shaded area represents the wavelengths absorbed by the so-called β -filter. The material chosen as a β -filter has an absorption edge below the wavelength of the $K\alpha$ characteristic peak and just above the wavelength of the $K\beta$ peak. Some common anodes and associated β -filter materials are presented in Table 3.3.

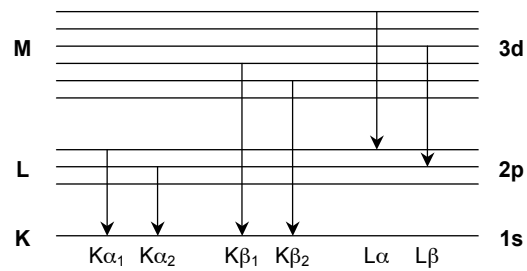


Figure 3.20: Electron orbital schematic showing the characteristic x-ray transitions.

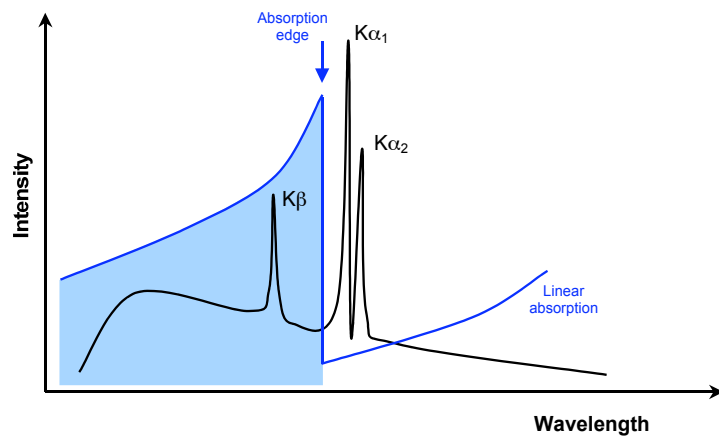


Figure 3.21: X-ray emission spectrum schematic overlaid with the linear absorption function of the β -filter

Table 3.3: Characteristic wavelengths of some common anode materials and the β -filter materials ^[15]

Anode		Wavelength (Å)	β -filter	Absorption edge (Å)
Mo	$K\alpha_1$:	0.70926	Zr	0.68896
	$K\alpha_2$:	0.71354	Nb	0.65313
	$K\beta$:	0.63225		
Cu	$K\alpha_1$:	1.5405	Ni	1.48814
	$K\alpha_2$:	1.54434		
	$K\beta$:	1.39217		
Co	$K\alpha_1$:	1.78890	Fe	1.74362
	$K\alpha_2$:	1.79279		
	$K\beta$:	1.62073		
Fe	$K\alpha_1$:	1.93597	Mn	1.896459
	$K\alpha_2$:	1.93991		
	$K\beta$:	1.75654		

3.4.4 Bragg's Law

When an incident x-ray beam strikes a polycrystalline sample, the beam becomes scattered. The beam is diffracted from the parallel lattice planes in the crystalline material at an angle that is dependent upon the spacing of the lattice. A crystalline material has an infinite number of lattice planes of differing Miller indices. All lattice planes with identical Miller indices are parallel to one another and are equally spaced, at an interplanar distance of d_{hkl} , where the subscript hkl refer to the Miller indices of the plane. The interplanar distance is often referred to as the *d-spacing*. The Miller indices refer to the family of crystallographic planes in the crystalline system. There are a number of expressions for the d-spacing corresponding to the different crystal systems, including cubic, monoclinic, hexagonal, etc.^[16] Each plane is considered a separate scattering object, and diffraction is only possible at specific angles, θ , as established from Bragg's law. Bragg's law is illustrated geometrically in Figure 3.22.

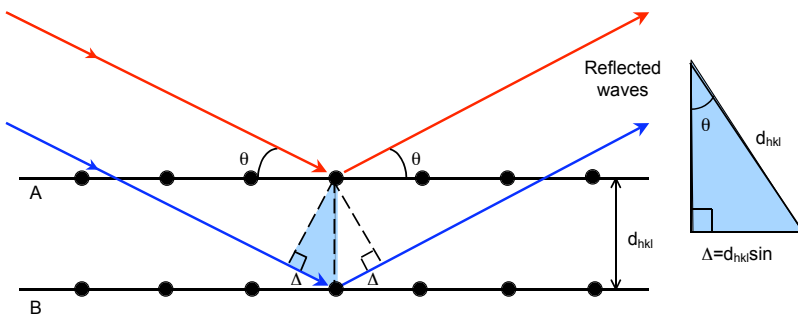


Figure 3.22: Geometric derivation of Bragg's law

Parallel incident waves, red and blue, with a wavelength, λ , are in phase and form an angle, θ , with planes A and B . The reflected waves will be parallel and have the same angle with the planes. The blue wave travels an additional distance an integral number of wavelengths, $n\lambda$. The path difference, 2Δ , between the red and blue waves is related to the interplanar distance by the following:

$$2\Delta = d_{hkl} \sin \theta \quad (3.21)$$

Constructive interference is observed when the total path difference, 2Δ , is equal to $n\lambda$, so equation (3.21) becomes the more common expression of Bragg's law as follows:

$$n\lambda = 2d_{hkl} \sin \theta \quad (\text{Bragg's Law}) \quad (3.22)$$

Structural information can be obtained from crystalline materials using Bragg's law. Crystalline materials have many lattice planes with differing Miller indices, each with a particular interplanar distance. The diffraction of an x-ray beam by the many lattice planes results in diffraction peaks at particular diffraction angles. The peak position can be determined from Bragg's law as a function of wavelength and d-spacing. The d-spacing can be expressed in terms of unit cell dimensions for the crystal system in question. Taking the cubic system as an example the Bragg angles can be found from the following:

$$2\theta = 2 \arcsin \left(\frac{\lambda}{2d_{hkl}} \right) \quad (3.23)$$

where,

$$d_{hkl} = \sqrt{\frac{a^2}{h^2 + k^2 + l^2}} \quad (3.24)$$

and a is the unit cell parameter. The diffraction peaks are generally represented on a plot of intensity versus 2θ .

3.4.5 Sample preparation

Polished sections of electrolysis cells, both tube and pellet cells, were prepared. The samples were placed on edge in a plastic mould. The mould was filled with a two-part epoxy resin, placed into a glass dessicator, and evacuated with a vacuum pump to remove the air from the epoxy and to allow epoxy to fill all open porosity in the sample. The sample was removed from the dessicator and left to cure overnight. The hardened epoxy with the embedded sample was removed from the mould. The epoxy sample was then ground with a 600-grit silicon carbide paper for 10 minutes on a Buehler Metaserv 2000 polishing machine with a pressure of 1.5 psi (10kPa) to expose the electrolysis cell surface. The sample was then ground on a 1200-grit silicon carbide paper for 20 minutes. The sample was thoroughly rinsed and cleaned in an ultrasonic bath prior to polishing with 6- μm diamond paste for 30 minutes, followed by 3- μm and 1- μm polishing in the same manner.

Secondary electron images were obtained on the polished samples with a Jeol 5600 SEM. EDS was performed on the samples and X-ray element maps were made with an Oxford instruments detector fitted to the SEM, and analysed with the Inca software. Prior to SEM experimental analysis the polished samples were sputtered with gold to form a conductive layer. The gold layer prevents charging by the electron beam in the instrument and gives a good yield of secondary electrons, thus a good quality image. The gold layer was approximately 10 nm, this was a sufficient thickness to provide good conduction.

3.5 X-Ray Diffraction

X-ray diffraction is a common technique for the characterization of polycrystalline inorganic solids. This technique has many applications including the identification of unknown solids, determination of sample purity, determination and refinement of lattice parameters and structure, as well as the investigation of phase diagrams, phase changes, and expansion coefficients of materials.

3.5.1 Powder Diffraction

For X-ray diffraction from a polycrystalline material, the powder diffraction method is used. A powder sample is obtained for the material; this powder contains very small particles or crystallites on the order of 10^{-7} to 10^{-4} m in size. These crystallites are randomly distributed in many orientations and will diffract an incident x-ray beam at all possible Bragg angles. A detector is scanned around the sample in a circle to collect the diffracted x-rays, as shown schematically in Figure 3.23.

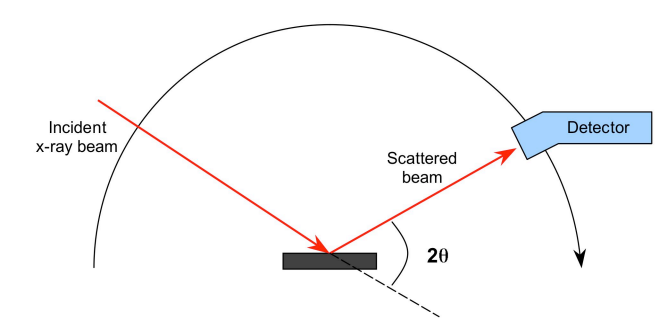


Figure 3.23: Schematic of a powder x-ray diffraction experimental setup.

Most crystalline solids have a unique x-ray diffraction pattern with differing peak positions and intensities. Mixtures of different materials and different crystal phases in the same material will contribute their own unique set of peaks to the total pattern; thus, phase purity can be determined easily. The peak intensities correspond to the amount of each phase or material present.^[16]

3.5.2 Sample Preparation

All x-ray powder diffraction experiments presented in this work were performed on a Philips Xpert PW 3020 diffractometer with a Cu-anode radiation source in reflection mode. An aluminium plate sample holder was used. A typical experiment ranged from a value of 2θ of 10° to 90° lasting approximately 1 hour.

3.6 Dilatometry

A push-rod dilatometer (Netzsch 402 C) was used to measure the thermal expansion of tube cells. A schematic diagram of the push-rod dilatometer is shown in Figure 3.24. The push rod and sample carrier were made of alumina. The sample is placed within the tube between two alumina piston supports were used for centering and to prevent direct contact between sample and carrier, as shown in Figure 3.25. The displacement was detected with a linear variable differential transducer. The temperature of the sample was measured with a Pt-Pt10%Rh thermocouple placed beside the sample. All measurements were carried out under a heating rate of $3\text{ }^\circ\text{C/min}$ with argon gas at a flow rate of 50 ml/min at ambient pressure. The acquisition of temperature and displacement was performed simultaneously by the Netzsch software at an acquisition rate of 6 points per $^\circ\text{C}$ (18 points per min.) from $30\text{ }^\circ\text{C}$ to $1000\text{ }^\circ\text{C}$. The displacement detected includes changes in the length of the parts of the dilatometer (i.e. push rod and sample carrier) as well as the sample. The system must first be calibrated with the use of an alumina reference material of a length similar to the unknown sample to be measured. The displacement data obtained from the dilatometer was analysed using the Proteus software.

[17]

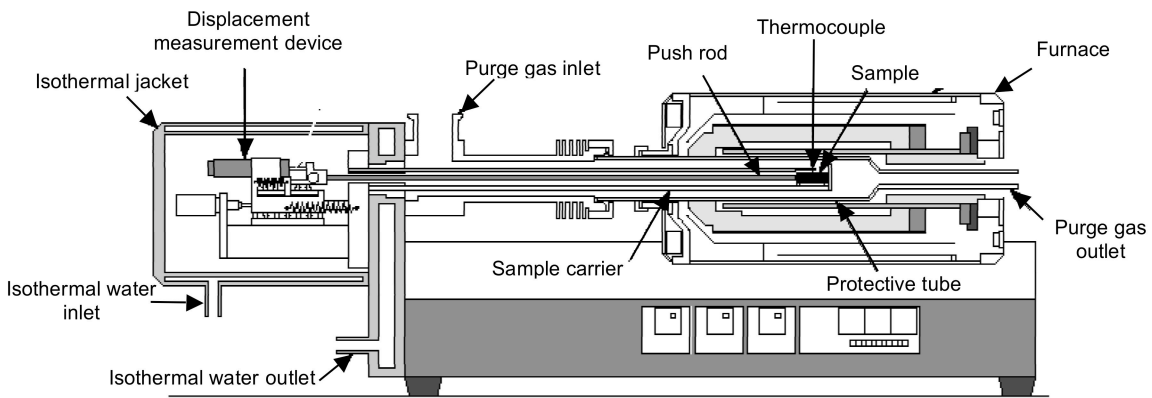


Figure 3.24: Schematic of the Netzsch 402 C push rod dilatometer^[18]

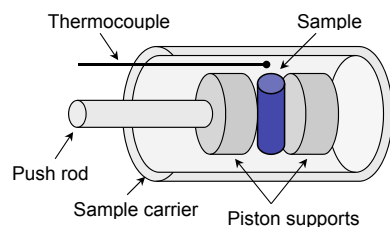


Figure 3.25: Dilatometer sample chamber

References

- ¹ Kellett, B.J., and F.F. Lange, "Advanced processing concepts for increased ceramic reliability." In *Advanced Ceramic Processing*, Advanced Ceramic Processing and Technology, Vol 1, pp 1-39, Ed. by J.P Binner, Noyes Pub., NJ (1990).
- ² Reed, J.S., *Principleps of Ceramics Processing, 2nd Edition*. New York: John Wiley and Sons, Inc., 1995
- ³ Chemat Technology Inc., 2005, www.chemat.com
- ⁴ Richerson, D.W. *Modern Ceramic Engineering: Properties, Processing and Use in Design, 3rd Edition*. Boca Raton: CRC Press, Taylor and Francis Group, 2006.
- ⁵ King, A.G. *Ceramic Technology and Processing*. New York: William Andrews Publishing, 2002.
- ⁶ Ehrhart, P. and R. Waser. "New thin film techniques." In *Handbook of Advanced Ceramics Vol 1: Materials Science*. Edited by S. Somiya et al. San Diego: Elsevier Academic Press, 2003.
- ⁷ Mistler, R., and E. Twiname. *Tape Casting Theory and Practice*. Westerville, OH: The American Ceramic Society, 2000.
- ⁸ Jones, F.G.E. "Tape Casting, Co-Firing and Electrical Characterisation of a Novel Design Solid Oxide Fuel Cell: Sofcroll." University of St Andrews, 2005.
- ⁹ Yang, Y., E. Laarz, S. Kaushik, E. Mueller, and W. Sigmund. "Forming and drying." In *Handbook of Advanced Ceramics Vol 1: Materials Science*. edited by S. Somiya et al. San Diego: Elsevier Academic Press, 2003.
- ¹⁰ Yamada, T. "Ionic Conductors/ Oxygen Sensors." In *Handbook of Advanced Ceramics Vol. 2: Processing and their Applications*. edited by S. Somiya et al. San Diego: Elsevier Academic Press, 2003.
- ¹¹ Macdonald, J. R. *Impedance Spectroscopy: Emphasizing Solid Materials and Systems*. New York: John Wiley & Sons, Inc, 1987.
- ¹² Bockris, J., A. K. N. Reddy, and M. Gamboa-Aldeco. *Modern Electrochemistry: Fundamentals of Electrodics*. New York: Kluwer Academic/Plenum Publishers, 2000.
- ¹³ Weller, M. T. *Inorganic Materials Chemistry*. Oxford: Oxford University Press, 1994.
- ¹⁴ Watt, I.M. *The Principles and Practice of Electron Microscopy*. Cambridge: Cambridge University Press, 1985.
- ¹⁵ Wilson, AJC, and E Prince. *International Tables for Crysalllography*. Boston/Dordrect/London: Kluwer Academic Publishers, 1999.

¹⁶ Pecharsky, V. K., and P. Y. Zavalij. *Fundamentals of Powder Diffraction and Structural Characterization of Materials*. Boston: Kluwer Academic Publishers, 2003.

¹⁷ Yamada, N., R. Abe, and M. Okaji. "A Calibration Method for Measuring Thermal Expansions With a Push-Rod Dilatometer." *Measurement Science and Technology* 12 (2001): 2121-29.

¹⁸ Netzsch Instruments, Inc. 2003. www.dilatometer.com,

Chapter 4: Anode Material Studies

4.1 Electrolyser Anode Materials.....	87
4.1.1 Introduction.....	87
4.1.2 Structure of anode materials.....	88
4.2 SEM and EDS Materials Analysis	91
4.2.1 LSM	91
4.2.2 LSCo	93
4.2.3 Ceria interlayer.....	99
4.2.4 LSF.....	101
4.3 Electrolysis Performance.....	103
4.3.1 Electrolysis testing	103
4.3.2 AC impedance.....	105
4.4 LSM anode.....	106
4.5 LSCo anode.....	110
4.6 LSF anode	114
4.7 Anode Material Comparison.....	120
References	124

4.1 Electrolyser Anode Materials

4.1.1 Introduction

The choice of anode material for high-temperature solid oxide electrolysis is an important factor in the overall performance of the electrolysis cell. The anode material must meet several requirements, among them, high electrical conductivity, good thermal and chemical stability, sufficient porosity, good adherence to the electrolyte surface, and catalytic activity for the oxygen reaction at the electrode surface. The orthoferrite-type perovskites are a family of compounds that satisfy many or all of these requirements. These materials are of the general form of $\text{Ln}_{1-x}\text{A}_x\text{MO}_3$, where Ln, A, and M are lanthanide, alkaline earth, and transition metals, respectively.^[1] In this study, the lanthanide is lanthanum (La), the alkaline earth is strontium (Sr), and the transition metal is manganese (Mn), cobalt (Co), or iron (Fe).

The standard SOFC cathode material is lanthanum strontium manganite, $\text{La}_{0.8}\text{Sr}_{0.2}\text{MnO}_3$ (LSM), which has been widely studied for SOFC applications; it possesses good chemical stability and has a comparable thermal expansion coefficient with the YSZ electrolyte material. LSM has also been used as the anode in electrolyzers.^[2,3,4] The main drawback of LSM for both SOFCs and electrolyzers is that its conductivity is low (200 S/cm) and primarily electronic.^[5] This limits the active areas of the electrode to triple phase regions where LSM, YSZ, and air are in contact.

Mixed ionic-electronic conducting materials (MIEC) are being investigated as potential cathode materials for intermediate temperature SOFCs.^[6] These materials also have potential for electrolysis applications. Lanthanum strontium ferrite (LSF) and lanthanum strontium cobaltite (LSCo) are examples of these materials. The mixed conduction provides a larger active region because the anode reaction is not limited to the triple phase regions as in LSM.

LSCo materials have attracted interest for use in several other advanced energy systems such as oxygen separation membranes, SOFC cathodes, sensors, and catalysts.^[7,8,9] LaCoO_3 has a high electrical and ionic conductivity when the divalent cation Sr is

substituted on the La site. Sr doping increases the oxygen deficiency, thus increasing the ionic conductivity to between 0.1-1 S/cm. LSCo has much higher electronic conductivity than LSM as well, with a value of 1000 S/cm at 800 °C.^[10] The main drawback of the LSCo is that the thermal expansion coefficient is much higher, 18-20 $\mu\text{m}/\text{m } ^\circ\text{C}$, than the YSZ electrolyte material.^[11] Also LSCo can react YSZ to form insulating phases at the interface.

The final material of interest, LSF, is also an MEIC material and has been widely studied for use in intermediate temperature fuel cells and as an oxygen membrane for syngas production. LSF anodes have a high ionic conductivity and have shown low interface resistance with YSZ electrolytes.^[12] The thermal expansion coefficient of LSF is 11.9 $\mu\text{m}/\text{m } ^\circ\text{C}$, which is more compatible with YSZ electrolyte material than LSCo.^[13]

4.1.2 Structure of anode materials

The orthoferrite-tye perovskites, $\text{Ln}_{1-x}\text{A}_x\text{MO}_3$, are characterized by rhombohedral distorted perovskite structures, deriving from the ideal cubic symmetry through rotation of the $[\text{MO}_6]$ octahedra around the three-fold axis. The extent of distortion and unit cell volume depend on the A-site dopant in this case, Sr.^[14] Figure 4.1-Figure 4.4 show the x-ray powder diffraction patterns for the LSM, sol-gel LSCo, commercial LSCo, and LSF anode materials. There are double peaks in the x-ray diffraction pattern for the sol-gel LSCo, which are not present in the pattern for the commercial powder.

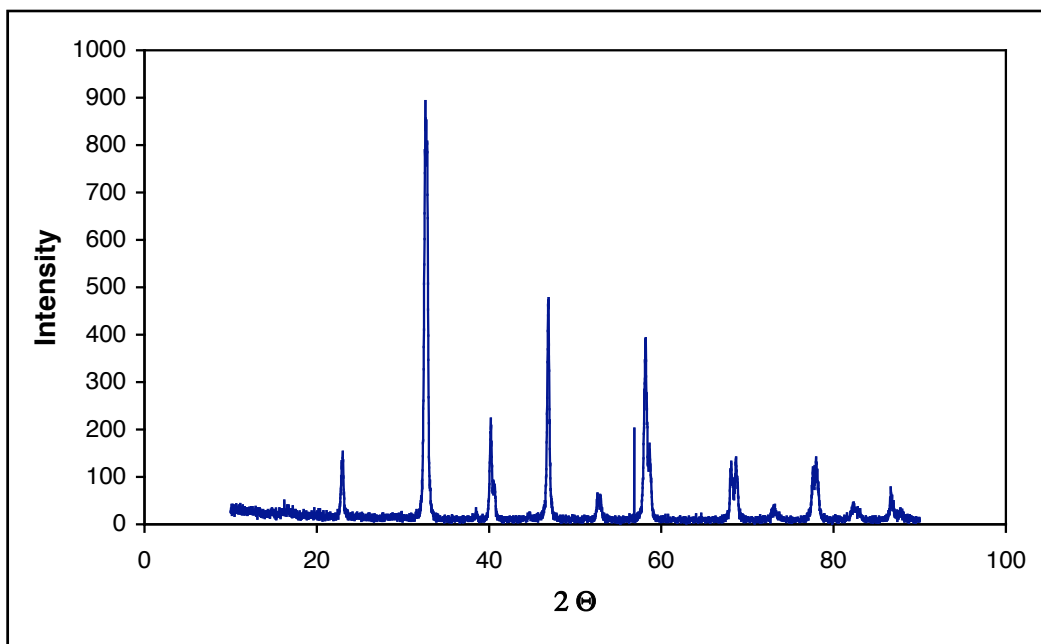


Figure 4.1 Commercial LSM x-ray powder diffraction pattern

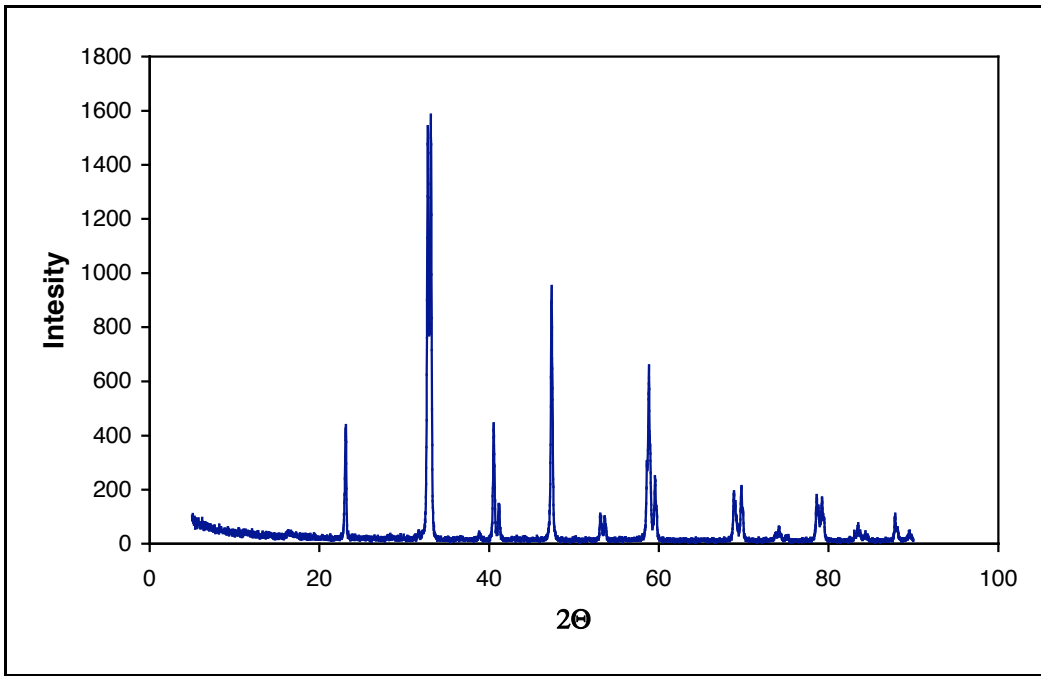


Figure 4.2: Sol-gel LSCo x-ray powder diffraction pattern

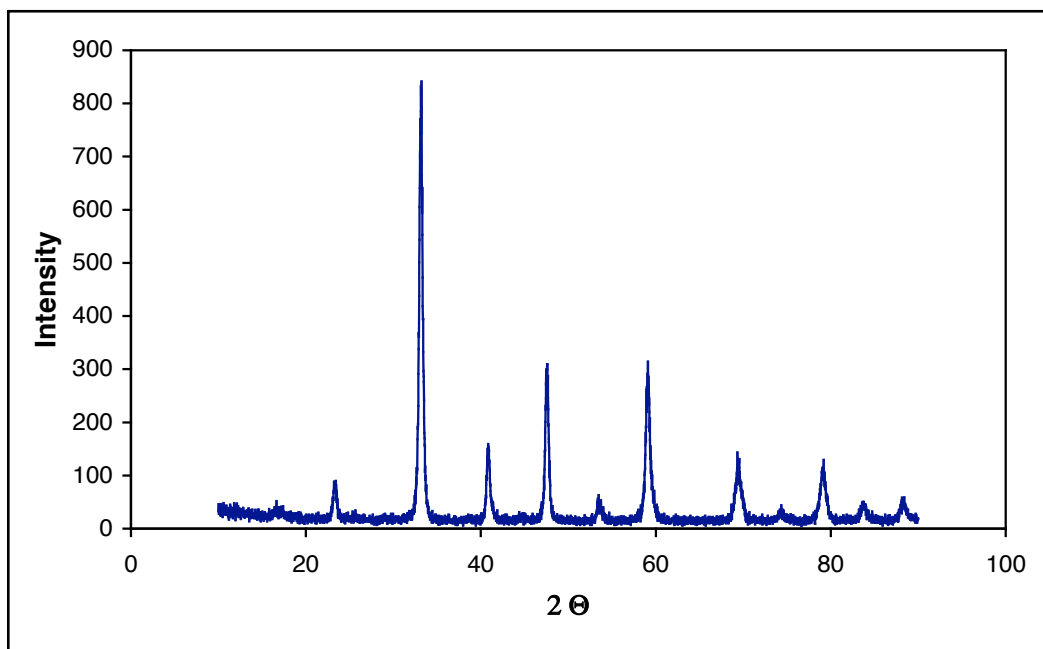


Figure 4.3: Commercial LSCo-4 x-ray powder diffraction pattern

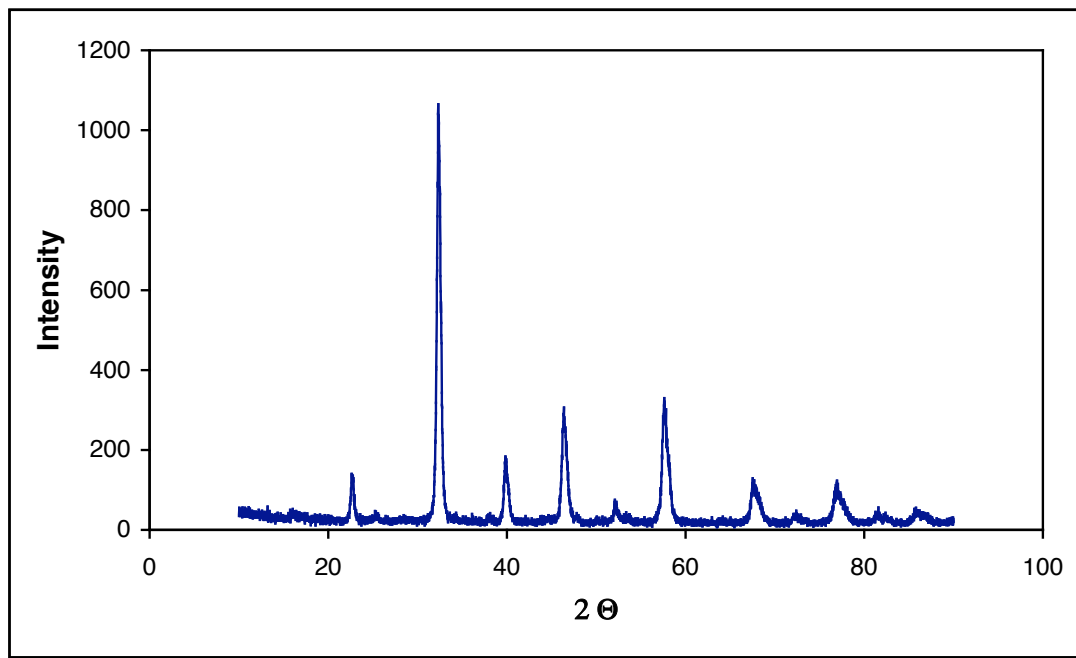


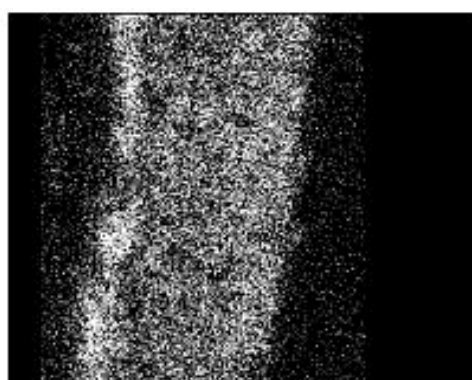
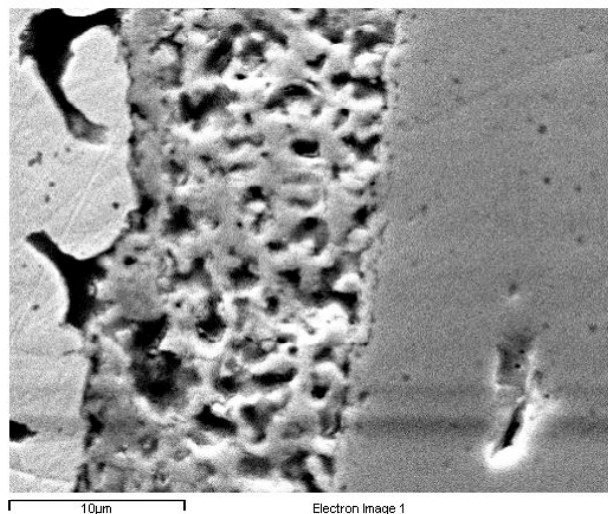
Figure 4.4: Commercial LSF x-ray powder diffraction pattern

4.2 SEM and EDS Materials Analysis

SEM and EDS analysis was performed on samples of electrolysis cells made with the three anode materials, LSM, LSCo, and LSF. The main area of interest was the interface between the screen-printed anode and the electrolyte. Unless otherwise stated all samples were taken from cells after electrolysis testing.

4.2.1 LSM

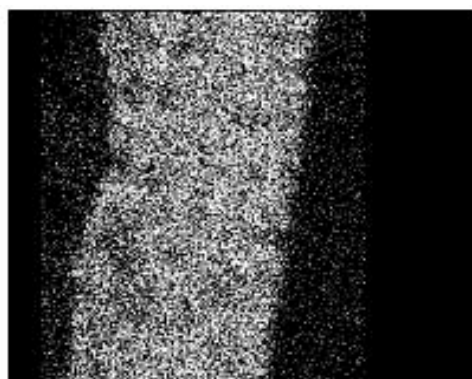
A secondary electron image and EDS element map of a screen-printed LSM layer on YSZ electrolyte substrate are shown in Figure 4.5. The LSM layers in most samples were intact and well adhered to the YSZ electrolyte. The few samples that exhibited a LSM layer separated from the YSZ were damaged upon removal from the electrolysis test apparatus, thus it was not possible to accurately describe the condition of the layer with regard to those few samples. The EDS element map of the LSM shows a slight concentration of Mn near the surface where the Pt current collector was applied. The cause of the Mn concentration is unknown. The element map shows no concentration of Sr at the LSM-YSZ interface, which would be an indication of a detrimental interfacial reaction. The reaction between LSM and YSZ is found to occur at sintering temperatures above 1300 °C. The main reaction product formed at the LSM-YSZ interface is generally believed to be $\text{La}_2\text{Zr}_2\text{O}_7$; this is also true for LaCoO_3 -based electrodes.^[15,16] The addition of Sr can lead to the additional formation of SrZrO_3 . As the Sr content is increased, the formation of $\text{La}_2\text{Zr}_2\text{O}_7$ is hindered and the formation of SrZrO_3 is enhanced.^[17] All electrolysis samples in this study were sintered well below 1300 °C and no insulating La- or Sr-zirconate phases were found. It should be noted as well that the apparent high concentration of Zr on the left side of the SE image and Zr-element map is not Zr but simply interference from the platinum current collector. This interference is seen in all the EDS element maps of sample areas that contain the Pt current collector.



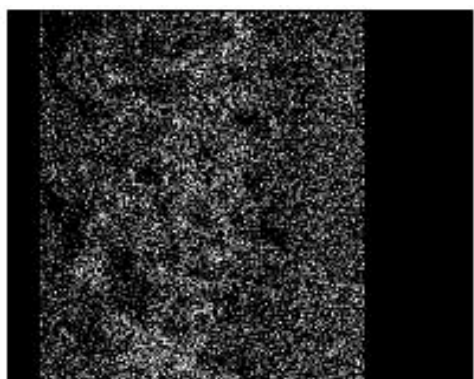
Manganese Ka1



Zirconium La1



Lanthanum La1



Strontium La1

Figure 4.5: Secondary electron image and EDS element map of screen-printed LSM anode on YSZ electrolyte.

4.2.2 LSCo

The initial attempts at screen-printing an LSCo layer on a YSZ substrate were not successful. After the drying and binder burnout and heat treatment up to 1000 °C, the LSCo layer appeared smooth and intact. The layer was delicate at this stage because it lacked a binder adhering the layer to the YSZ. After the sintering heat treatment, however, the layer was crazed and appeared to have shrunk a great deal upon sintering. The layer also flaked off readily indicating that there was poor adhesion to the YSZ substrate.

The screen-printed sample was mounted in epoxy and polished for inspection in the SEM. Figure 4.6 shows a secondary electron image of the LSCo layer on the YSZ electrolyte. The LSCo powder has sintered well, but in some areas the LSCo layer had flaked off indicating poor adhesion to the YSZ substrate. Due to the poor adhesion this sample did not undergo electrolysis testing.

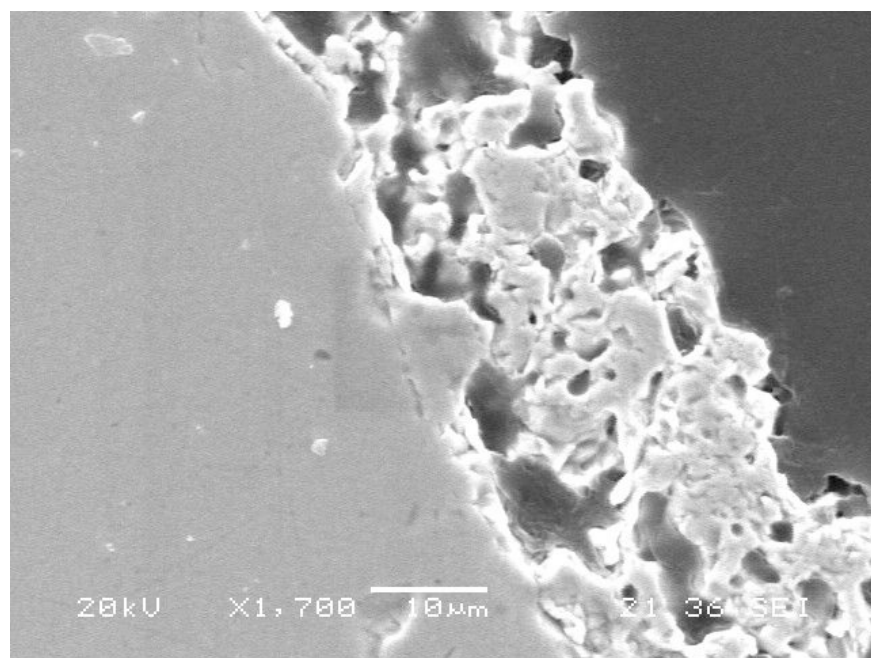


Figure 4.6: SE image of screen-printed LSCo anode on YSZ electrolyte.

The poor adhesion could be due simply to the shrinkage during sintering of the LSCo and could be corrected by altering the heat treatment cycle. Another possible explanation is a reaction between the LSCo and YSZ at the interface. EDS analysis of a section where the adjacent to that seen in Figure 4.6 was conducted, and an x-ray element map obtained. Figure 4.7 shows the element map of the area. A few locations with a high concentration of cobalt near the interface with YSZ are evident. A stripe of strontium also appears just at the interface, suggesting that there is a reaction between the LSCo layer and the YSZ. There is considerable scatter in the strontium response because the Sr K α 1 peak is near to the Zr K α 1 peak. In subsequent EDS element maps, the Sr L α 1 response was used to increase the Sr discrimination.

Both LaCoO₃- and LaMnO₃-based electrode materials can react with YSZ at high temperature, giving La₂Zr₂O₇ and SrZrO₃. This reaction also occurs between YSZ and La_{1-x}Sr_xCoO₃ materials with low strontium content.^[18] The presence of the concentration of strontium and an absence of lanthanum at the interface indicates that the reaction product is more likely to be SrZrO₃ than La₂Zr₂O₇. The reaction also occurred with the commercial LSCo powder. In the section shown in Figure 4.8, the LSCo layer has completely pulled away from the YSZ surface. The corresponding EDS element analysis shows a clear stripe of strontium at the YSZ surface, but no lanthanum in the same area.

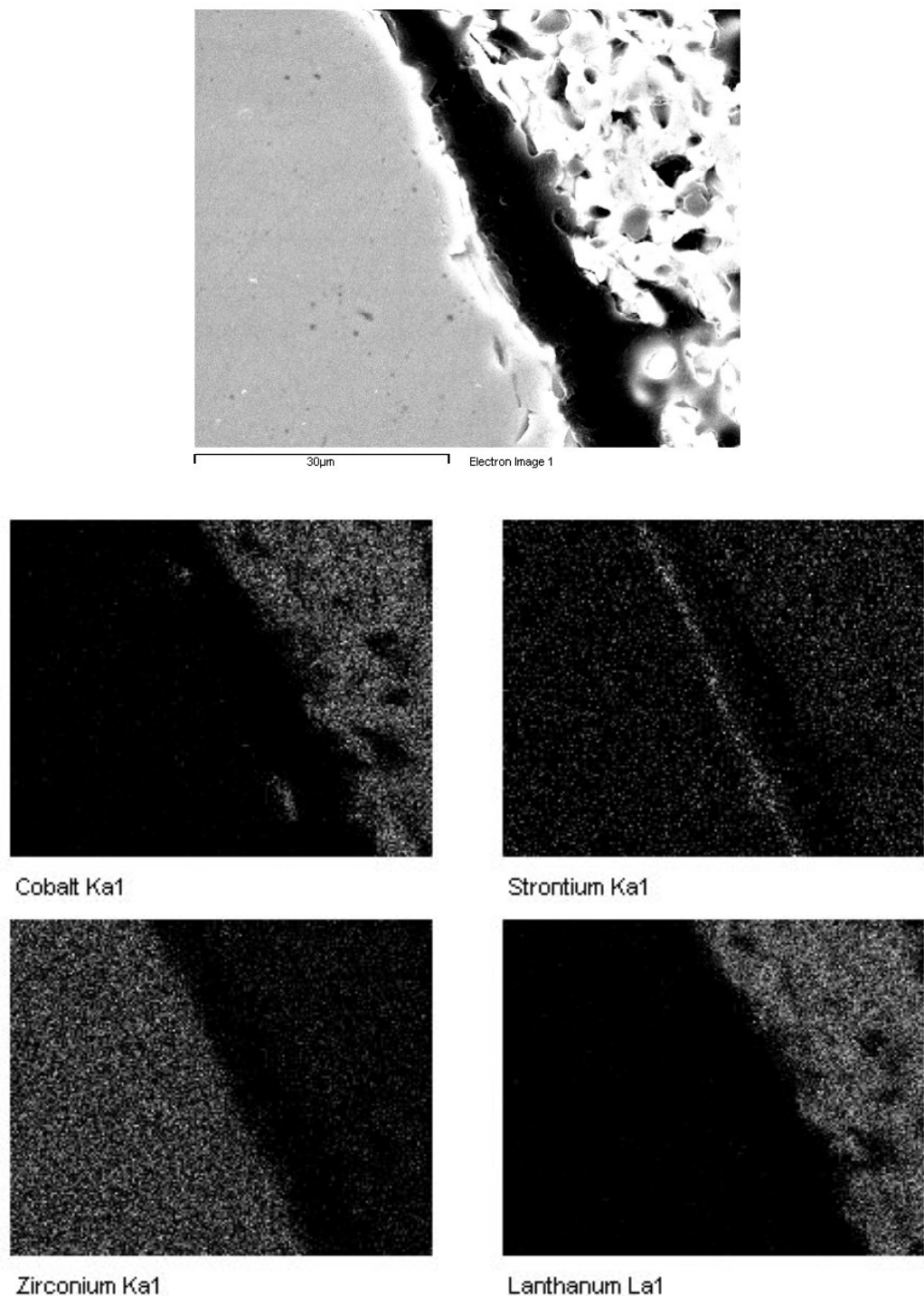
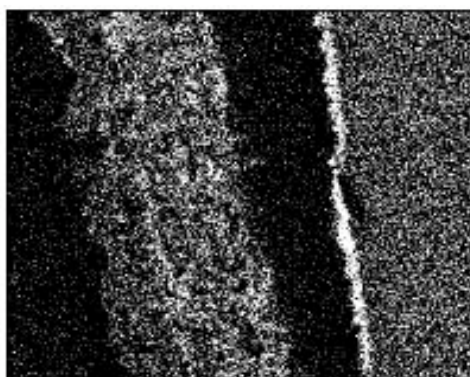
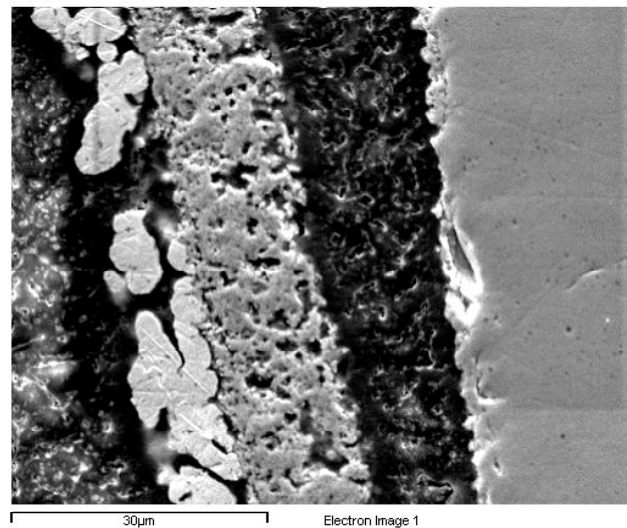
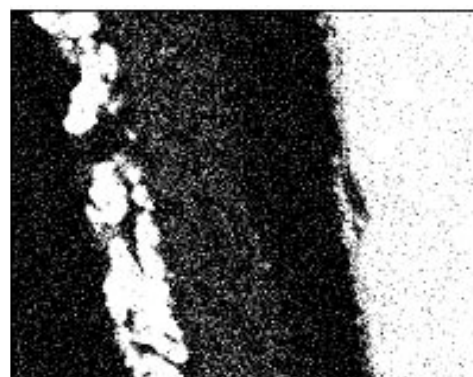


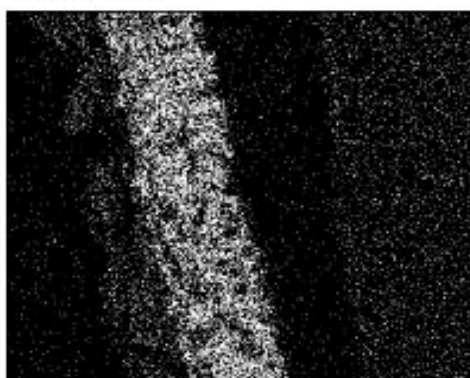
Figure 4.7: SE image and EDS element map of screen-printed LSCo on YSZ electrolyte.



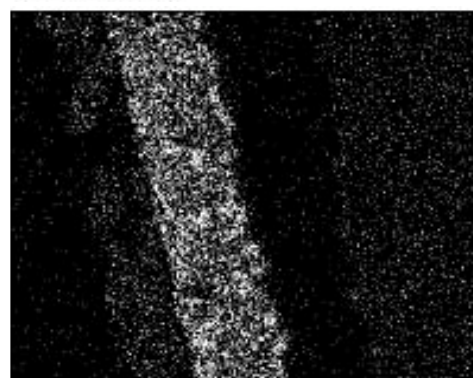
Strontium La1



Zirconium La1



Lanthanum La1



Cobalt Ka1

Figure 4.8: SE image and EDS element map of screen-printed LSCo anode on YSZ electrolyte showing a concentration of strontium at the interface.

slower heating rate with no interruption from room temperature to 1150 °C was employed for both the binder burnout and sintering of the screen-printed LSCo layer. The slower heating alleviated the crazing problem. The LSCo layer appeared intact prior to testing. This slower rate was used for the samples prepared with the commercial LSCo powder

In some samples, which appeared to be in good condition prior to electrolysis testing, the LSCo layer was damaged after testing, and the YSZ electrolyte was tinged blue around the perimeter of the screen-printed layer after testing. Where the contact layer of platinum remained intact on top of the LSCo layer the condition of the LSCo layer or any cracking could not be seen.

Polished cross sections of the slow heating rate electrolysis cells were prepared. Figure 4.9 shows a secondary electron image of a representative area in an LSCo cell. The electrode layer does not appear to be adhered to the YSZ electrolyte, but that may be due to epoxy shrinkage during the curing step of the polished sample preparation. The poor adherence could also be a result of shrinkage upon cooling of the sample after testing.

Most of the LSCo samples appeared similar to the one shown in Figure 4.9, with only a small separation between the LSCo layer and the YSZ. Two samples, however, had LSCo layers that were wavy and had buckled away from the YSZ. This effect can be seen in Figure 4.10. The buckling is undoubtedly due to the CTE mismatch. The LSCo layer expanded more upon heating than the YSZ, causing the LSCo layer to buckle. It is not known why only a few samples exhibited this buckling; perhaps these samples were sintered in a location of the muffle furnace with uneven heating.

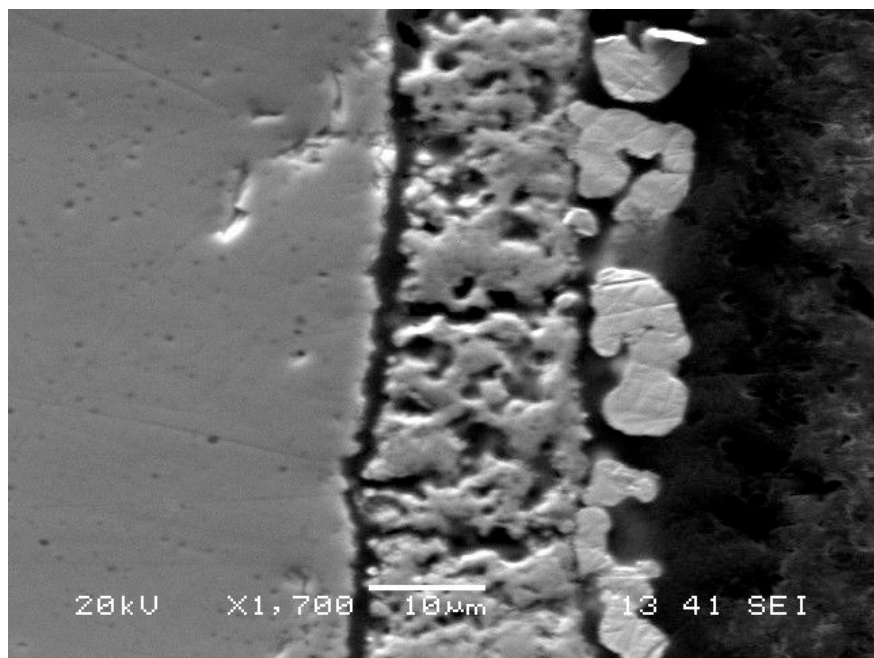


Figure 4.9: SE image of screen-printed LSCo anode on YSZ electrolyte with a small separation between the layers after testing.

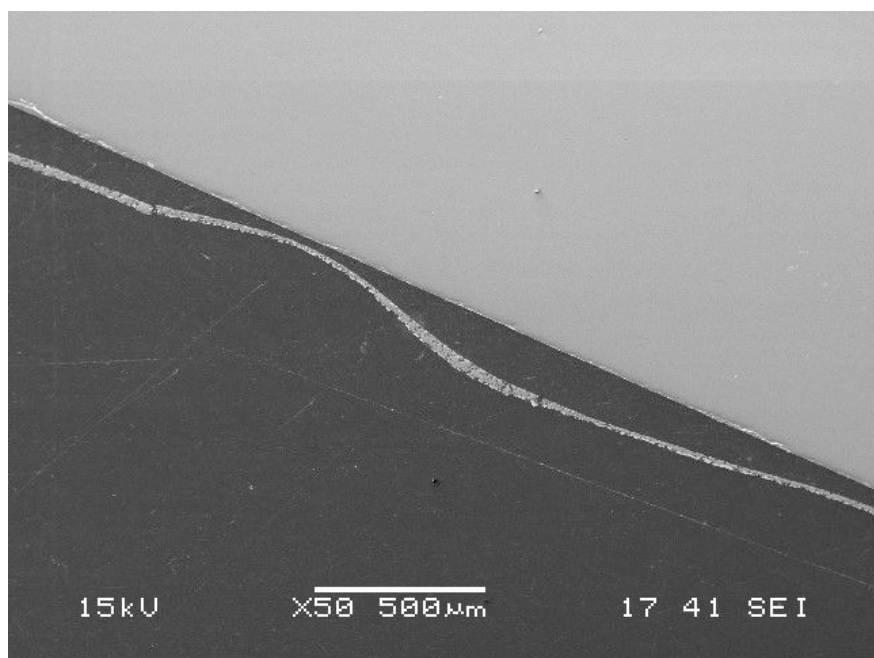


Figure 4.10: SE image of a buckled LSCo anode on YSZ electrolyte.

4.2.3 Ceria interlayer

In an attempt to avoid the reaction between the LSCo electrode and the YSZ electrolyte a protective interlayer of ceria was applied to some samples. Figure 4.11 is an EDS element map of an area in a cell with the ceria interlayer. The strontium map does not contain the concentration of strontium at the interface that was seen in the previous LSCo samples.

The ceria interlayer seemed to act as a barrier to the interface reaction between the anode and electrolyte. This was a first attempt with the interlayer. Further study of the effects of the ceria on the anode material and the performance of the electrolysis cells is needed.

SOFC system studies ^[19,20,21] indicate that a ceria interlayer can enhance the SOFC cell performance up to 50%, though the exact role of the ceria layer is not fully understood. Most likely the ceria layer enhances the mixed ionic and electronic conduction, extending the active interface.

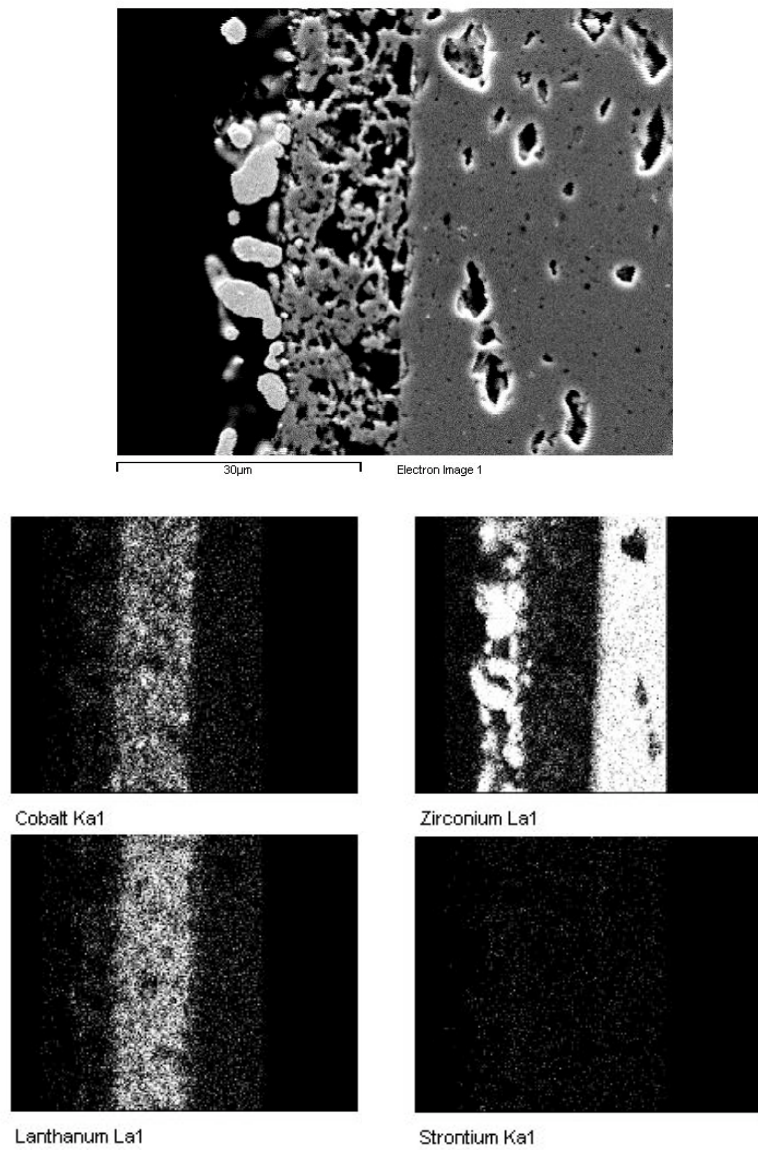


Figure 4.11: SE image and EDS element map of electrolysis cell with ceria interlayer between the LSCo anode and YSZ electrolyte

4.2.4 LSF

Figure 4.12 shows a secondary electron image of a screen-printed LSF layer on a YSZ electrolyte. As shown in the image, a feature along the interface between the materials can be readily seen. An EDS element map of the interface region was obtained to examine the interface area and is presented in Figure 4.13.

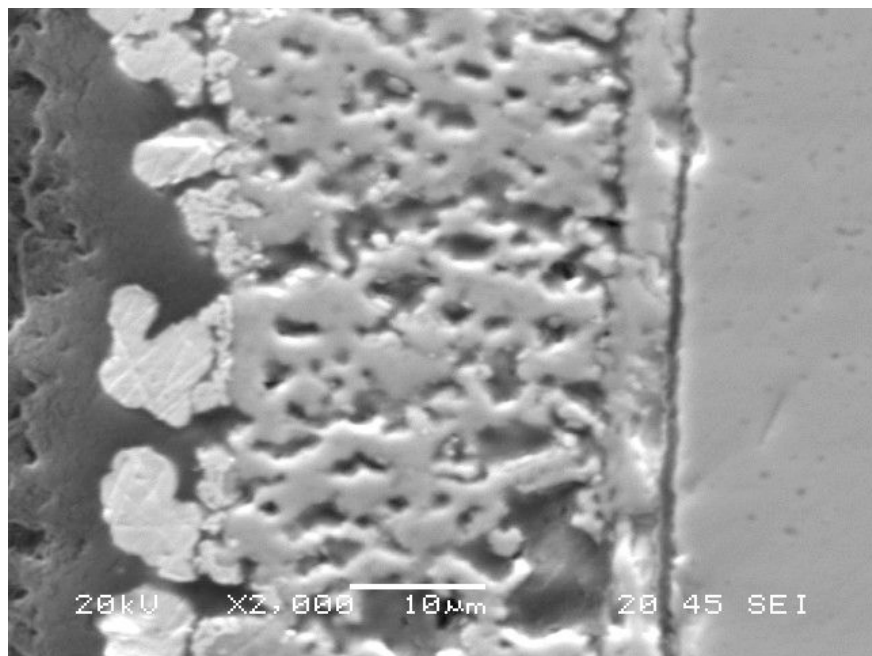
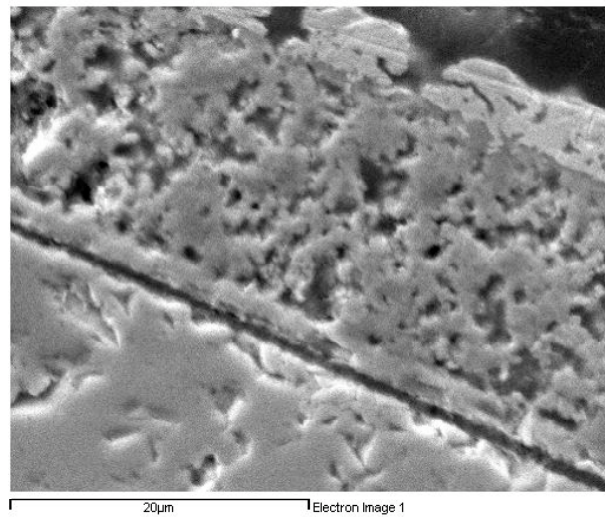
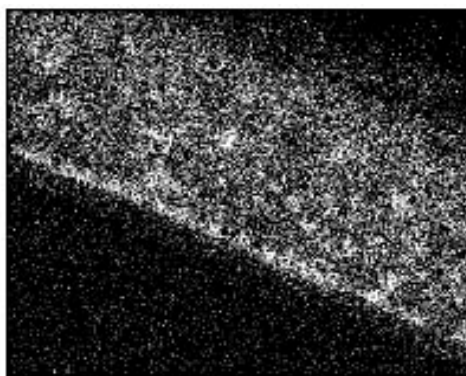


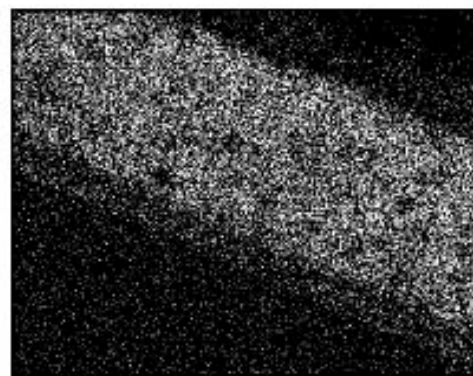
Figure 4.12: SE image of screen-printed LSF anode on YSZ electrolyte



20μm Electron Image 1



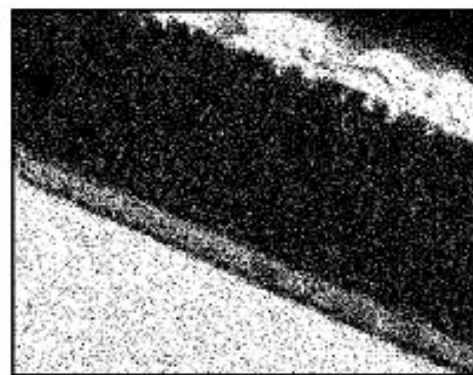
Iron Ka1



Lanthanum La1



Strontium La1



Zirconium La1

Figure 4.13: SE image and EDS element map of LSF on YSZ

The EDS element map shows the interface region contains Zr, Sr, and a concentration of Fe, as well as an absence of La. This may be the result of a new denser phase forming at the interface boundary. The new phase would be of the form $\text{Sr}(\text{Fe},\text{Zr})\text{O}_{3-\delta}$. Another

possible explanation from literature is the XRD results of Simner et al.^[22], which claim no new reaction phases are present in sintered mixtures of LSF and YSZ up to 1400° C. Simner et al. found an increase in the unit cell is observed from the XRD results, indicating a different perovskite is produced. The explanation given for the increase is due to Zr inclusion in the LSF perovskite structure up to a depth of 2 µm into the LSF. The explanation by Simner is not consistent with the EDS results from this work, which show a La-deficiency at the interface. Further investigation would be required to fully understand this interface.

4.3 Electrolysis Performance

4.3.1 Electrolysis testing

All cells were tested in the manner described in section 3.2. The samples were tested in each of four gas atmosphere conditions as tabulated in Table 4.1.

Table 4.1: Gas atmosphere conditions for electrolysis testing

Name	Cathode chamber	Anode chamber
“Dry/Ar”	3% H ₂ O in Ar	Ar
“Steam/Ar”	50% H ₂ O in Ar	Ar
“Dry/O ₂ ”	3% H ₂ O in Ar	O ₂
“Steam/O ₂ ”	50% H ₂ O in Ar	O ₂

Some cells were not tested in all gas conditions due to sample cracking, anode deterioration, or sealing problems. The open circuit voltage (OCV) for the electrolysis tests are not as straight forward as for fuel cell testing, where an OCV of approximately 1V is expected for O₂ vs H₂ atmospheres. In the electrolysis tests the opposing gases were H₂O in Ar vs. Ar, or vs. O₂. The measured OCV for most tests in Dry/Ar and Steam/Ar was 0.75 V. Often the measured OCV was not stable and would decrease with time. This was likely due to improper sealing of the test apparatus. In the Dry/O₂ and Steam/O₂ atmospheres the OCV was close to 0V because the opposing gases did not produce a sufficient oxygen gradient across the electrolyser cell. Another cause for error in the OCV

measurement is the flow rate of the gases. Although every effort was taken to keep the flow steady the flow meters used to control the inlet gases fluctuated during the testing.

Figure 4.14 shows a typical set of I-V curves for a cell with an LSCo anode at several temperatures. It can be seen that the performance of the cell improves as the temperature increases as is expected. All samples made with each of the three anode materials behaved in this manner regardless of the testing gas atmosphere used, so I-V performance at all temperatures will not be presented for each material. Full I-V sweeps from 0V to 1.5V and back to 0V are shown in Figure 4.15. For many tests, especially the “steam” tests, there was considerable noise on the downward ($1.5V \rightarrow 0V$) sweep. Also due to equipment error it was not always possible to record the downward sweep for all tests. For these reasons only the upward sweep is shown in most figures, except where noted.

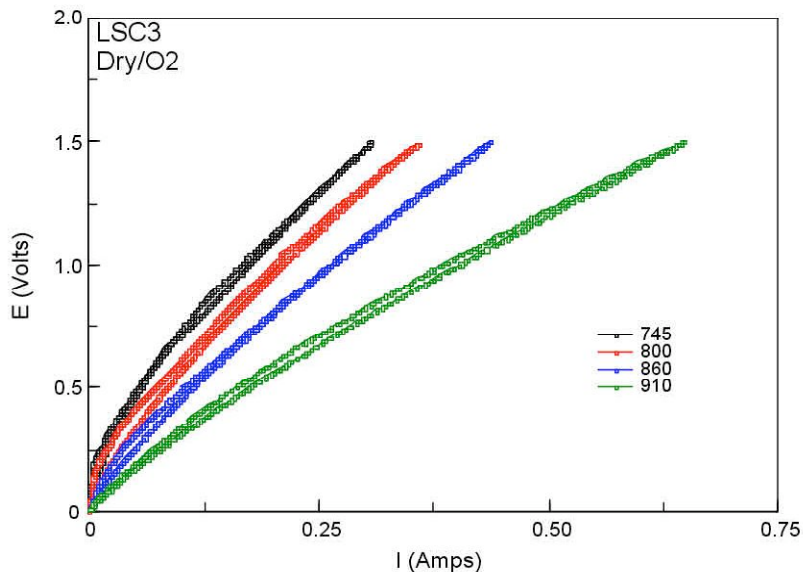


Figure 4.14: Electrolysis performance as a function of temperature. LSCo anode sample, 3% H_2O in Ar on Pt cathode, O_2 on anode.

4.3.2 AC impedance

AC impedance measurements give information on material resistance, including internal resistances involved with transport of electrons in electrode and transport of oxygen ions in the electrolyte and electrodes, and contact resistance from the contact between the electrode and electrolyte. All AC impedance data were obtained on electrolysis cells with a platinum cathode, YSZ electrolyte and LSM, LSCo, or LSF as the cathode. Platinum was used as the cathode because NiO in the more common Ni-YSZ cermet material could not be adequately reduced in the Ar atmosphere used in the test apparatus. The electrolysis cell resistance was obtained from the high frequency intercept of the Nyquist plot of AC impedance. The Nyquist plots of the AC impedance data generally contain two or three arcs for electrolysis tests. Only two semicircles could be distinguished in the Nyquist plots for the electrolysis cells in this work. The Nyquist plots for the materials in this study were not ideal semicircles, but generally had overlapping arcs representing the different responses. The overlap arises because the time constants for the processes occurring at different frequencies are of similar magnitude and are too close together to distinguish.

Analysis by the use of equivalent circuits allows for the impedance data to be modelled, as a circuit comprised of resistors and capacitors representing the various transport processes. The equivalent circuit shown in Figure 4.15 was used with the Z-view complex non-linear least squares fitting program to model the impedance response^[23]. The high frequency response represents the YSZ electrolyte ionic resistance. It is necessary to note that this resistance includes the resistance of the electrical contact wires. Medium frequency response is related to the electrode-electrolyte interface reactions or ion transfer resistances. Low frequency response is related to the electrode surface oxygen exchange reaction and gas diffusion through the electrode.. The model generally had a good fit at high frequencies for all materials, however, at low frequency the fit deviated from the measured data as the model fails to account for the complexity of the electrolyser system. A polarization was applied during some AC impedance tests to further distinguish between the electrode responses. The AC impedance tests were performed under the electrolysis testing gas conditions. The steam conditions were generally not stable enough to get reliable AC impedance data. The steam caused

condensation at the head of the test apparatus causing sporadic short circuits in the electrical contacts at the electrode.

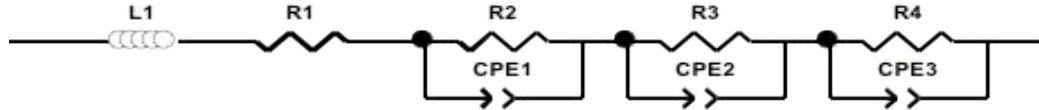


Figure 4.15: Equivalent circuit used for fitting ac impedance data

4.4 LSM anode

Figure 4.16 presents the Nyquist plot of AC impedance for an electrolysis cell with LSM anode. It can be clearly seen that the resistance of the electrolysis cell decreases with increasing temperature. A representative example of the electrolysis performance of a cell with an LSM anode under each testing atmosphere is shown in Figure 4.17. As can be seen the performance of the cell with O₂ in the anode chamber was nearly identical for tests with the dry (3% H₂O) and steam (50% H₂O) atmospheres in the cathode chamber, indicating the process is not strongly affected by the concentration of available steam. The OCV of the Steam/Ar test is 0.74V, the measured OCV of the Dry/Ar test was much lower around 0.35V. An apparent activation polarization is seen in the Dry/Ar test up to approximately the expected OCV voltage. Observation of the pO₂ sensor on the Ar outlet stream revealed that electrolysis did not occur until the cell voltage was greater than the expected OCV. There is a concentration polarisation seen in both tests at higher current. This concentration polarisation is much more severe and occurs at a lower current for the dry test than for the steam test. The area specific resistances (ASR) from the electrolysis tests on LSM anode cells in various atmospheres are presented in Figure 4.18. It should be noted that the ASR values are taken from a linear fit of the cell voltage region of the I-V curve in the upward (0V → 2.2V) sweep of the measurement, neglecting the activation polarization and concentration polarization regions of the curve, see Figure 2.3. There was little agreement between the LSM anode cells under the Steam/Ar condition resulting in significant scatter in the resulting average ASR plot. As stated previously operation under

steam conditions caused condensation in the electrolysis test apparatus leading to a noisy I-V for many tests.

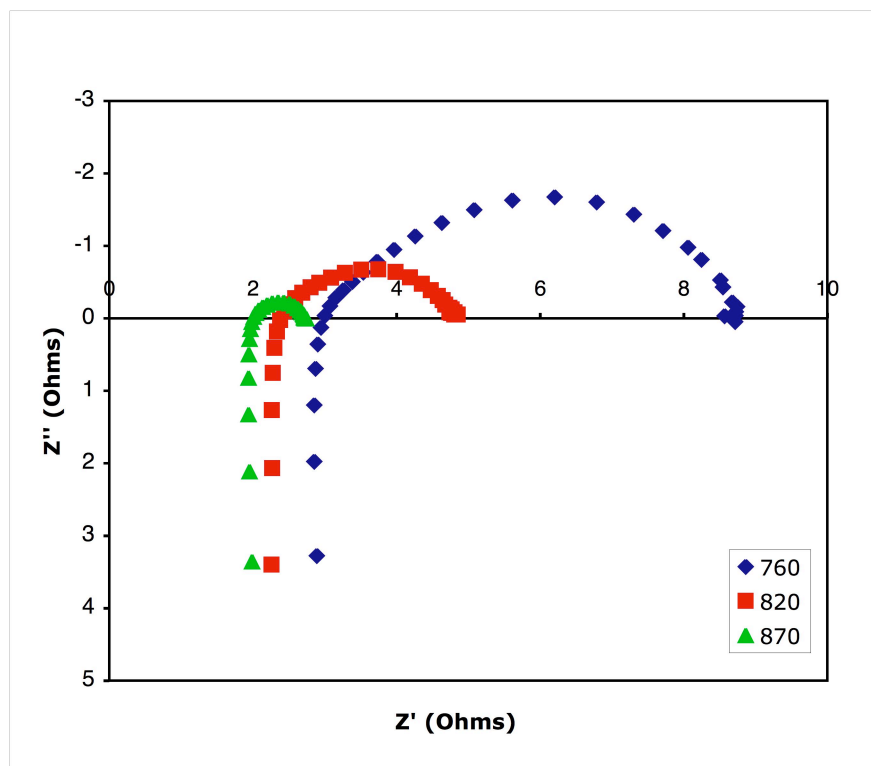


Figure 4.16: Nyquist plot of electrolysis cell with LSM anode showing decrease in resistance with increasing temperature

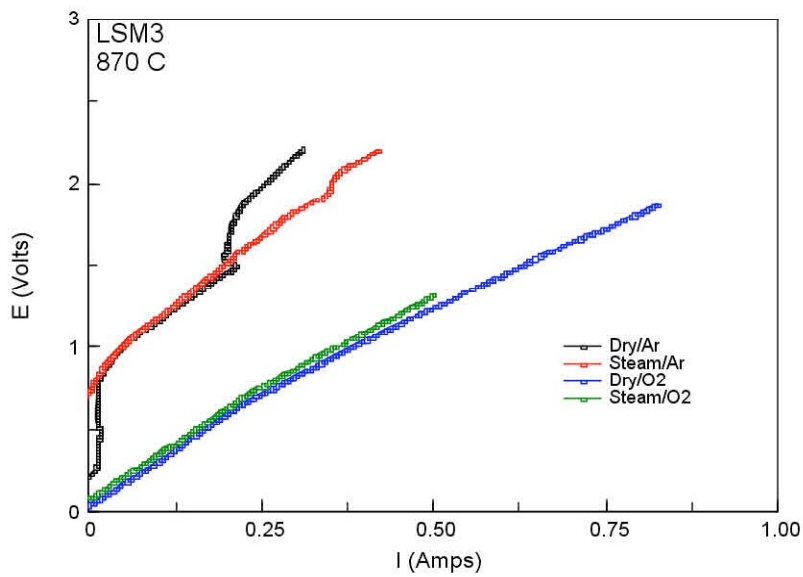


Figure 4.17: Electrolysis performance for cell with LSM anode in various gas atmosphere conditions at 870 °C.

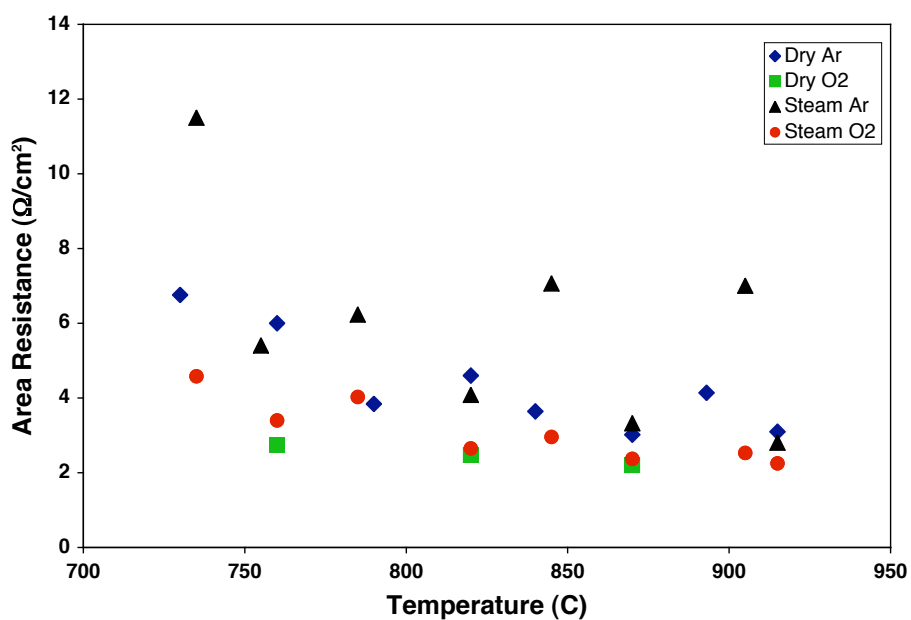


Figure 4.18: Average area resistance for all electrolysis cells with LSM anode in various gas atmosphere conditions

Only the upward sweep of the I-V curves are shown in Figure 4.17, the complete I-V curves including the downward sweep for the Dry/Ar and Steam/Ar tests at 870 °C are shown in Figure 4.19. A large hysteresis is observed in both of these I-V curves, particularly in the case of the Dry/Ar atmosphere. The downward sweep does not exhibit the polarisation at high currents seen in the upward sweep. This hysteresis behaviour was observed in all LSM and LSF electrolysis tests in the Dry/Ar atmosphere at all testing temperatures. No hysteresis was observed for Dry/O₂ or Steam/O₂ tests. This result indicates the presence of a reversible polarisation at higher currents. Nyquist plot of the AC impedance data for this cell under each of the testing atmospheres is presented in Figure 4.20. The responses for the cell under the Steam/O₂ and Dry/O₂ conditions are the same with the Dry/O₂ with a slightly lower resistance. The Dry/Ar shows a low frequency arc, and then the response goes off the scale of the plot. The Steam/Ar response is much larger than the scale of the plot.

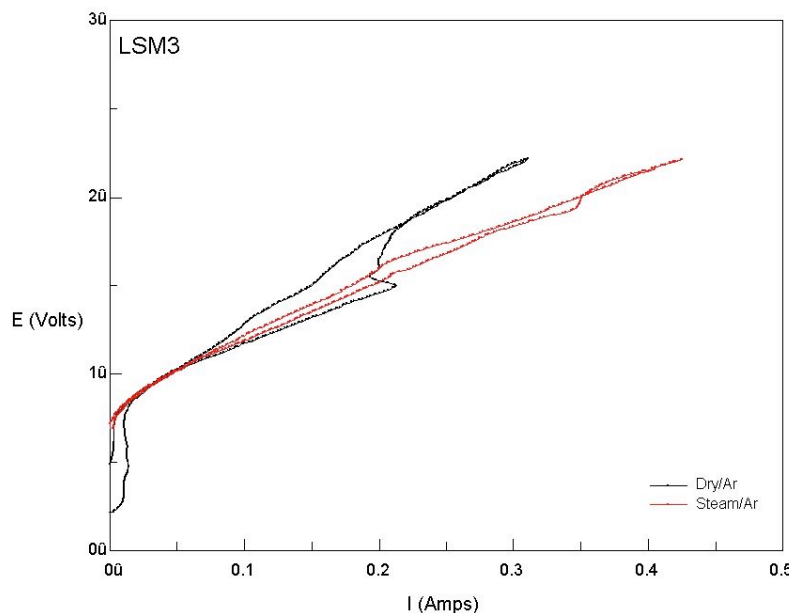


Figure 4.19: Electrolysis performance for cell with LSM anode at 870 °C in Dry/Ar and Steam/Ar atmospheres. The full 0V→2.2V→0V sweep is shown.

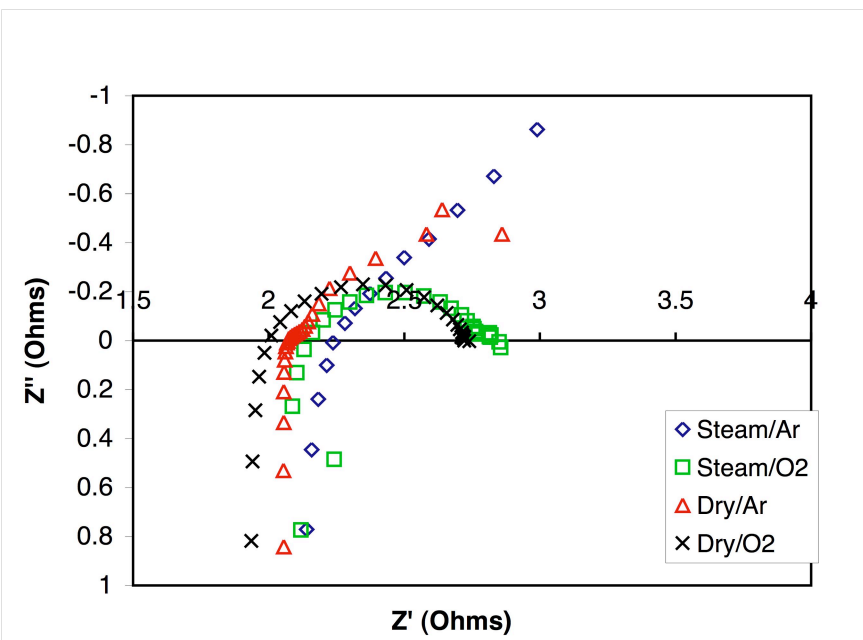


Figure 4.20: Nyquist plot of AC impedance for electrolysis cell with LSM anode in various testing atmospheres.

4.5 LSCo anode

As with LSM the resistance of the electrolysis cell with LSCo anode decreased with increasing temperature as seen in the Nyquist plot of the AC impedance data in Figure 4.21. Figure 4.22 shows a representative I-V plot for cells with an LSCo anode. The OCV measured prior to the electrolysis tests for the Steam/Ar and Dry/Ar tests was 0.75V, but decreased between measurements likely due to a gas leak in the test apparatus. Again like the previous LSM oxygen production could not be detected until the cell voltage was greater than 0.75V. This can be observed by the apparent activation polarisation seen at low currents in the I-V curve. Unlike the LSM cells the performances with O₂ in the cathode chamber are not identical for the dry and steam tests. The performance for the dry test was better than the steam test. This was typical for all LSCo cells. An explanation for this could be that the LSCo anode deterioration over time or formation of La₂O₃ impurity under steam conditions. The tests were performed in the dry atmosphere from 700-900 °C, and then the steam tests were performed. As discussed in section 4.2.2, the LSCo material was very susceptible to reaction with the YSZ electrolyte, and the time and thermal cycle for the dry tests could easily be enough to deteriorate the LSCo anode and form the insulating zirconate product at the interface. The tests performed with Ar in the

cathode compartment had similar activation polarisation behaviour to the LSM cells at low current, although the concentration polarisation was not observed at higher currents. The area specific resistances for electrolysis tests of LSCo anode cells in various testing atmospheres are presented in Figure 4.27.

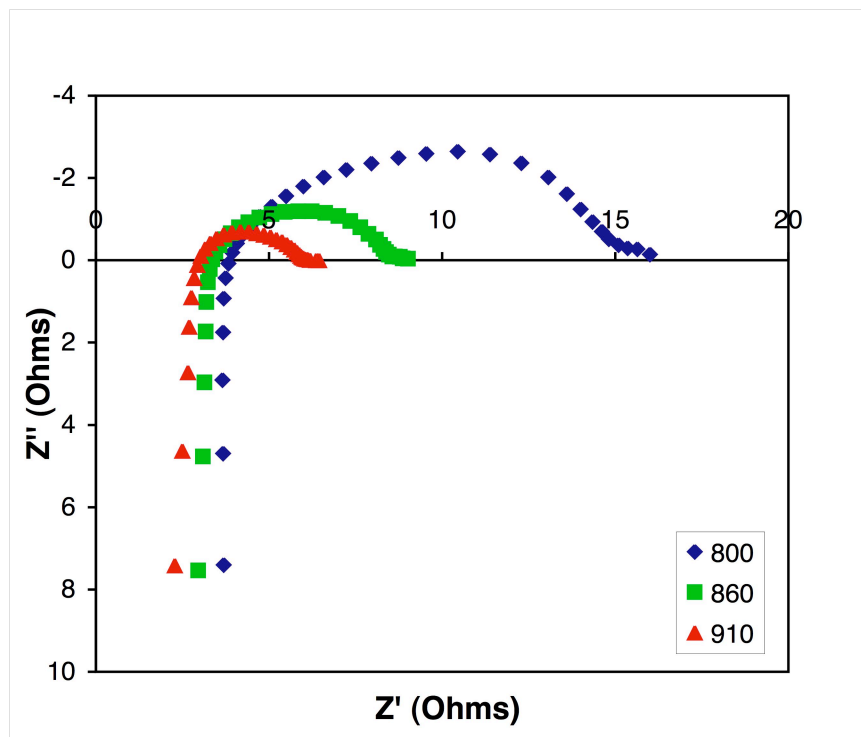


Figure 4.21: Nyquist plot of electrolysis cell with LSCo anode showing decrease of resistance with increasing temperature

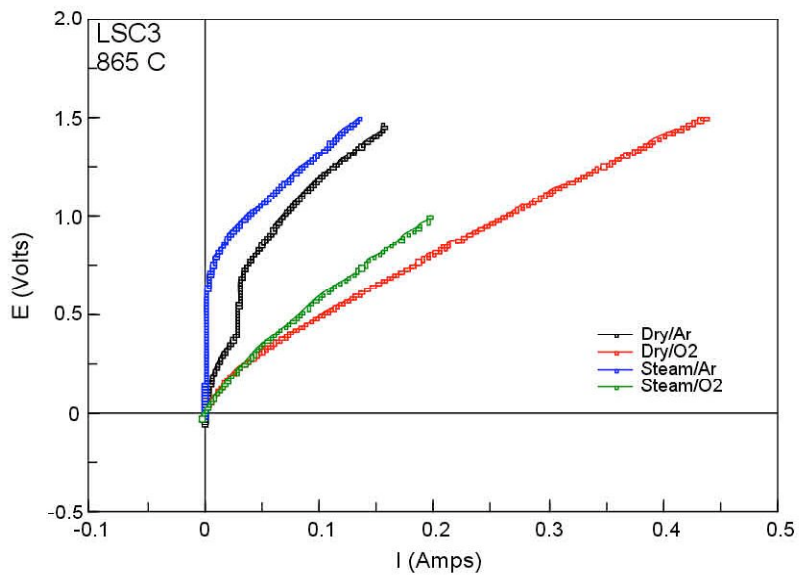


Figure 4.22: Electrolysis performance for cell with LSCo anode in various gas atmosphere conditions at 865 °C.

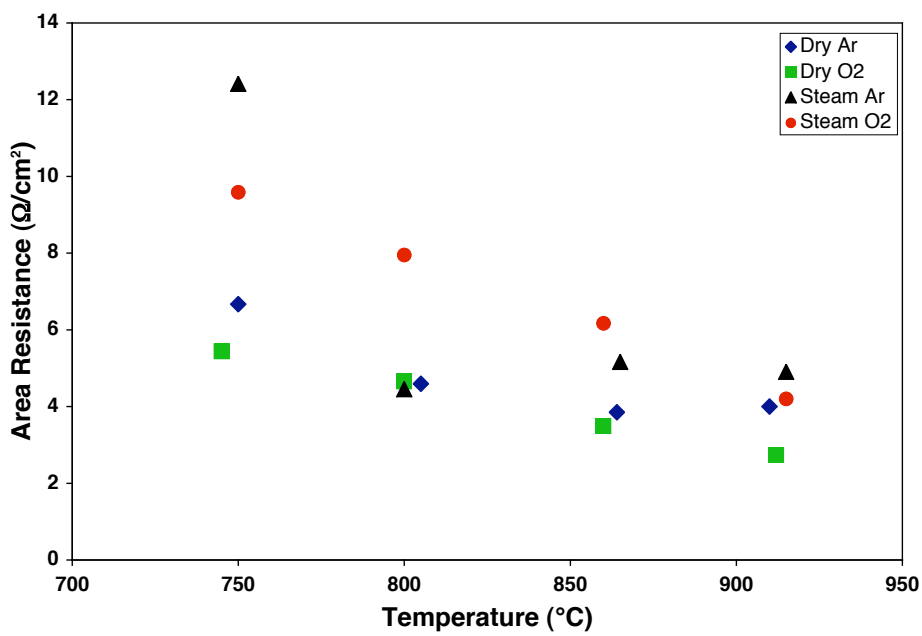


Figure 4.23: Average area resistance for all electrolysis cells with LSCo anode in various gas atmosphere conditions

AC impedance tests were performed on the LSCo electrolysis cells with a polarisation applied to draw a current through the cell. Figure 4.24 shows the Nyquist plot of the AC impedance at 860 °C and 910 °C with and without the 0.1V polarisation applied to the electrolysis cell. The responses with the applied polarisation exhibit smaller overlapping arcs than without polarisation at each temperature. The low frequency arcs for the polarised tests curve back toward the origin. Table 4.2 shows the fitted equivalent circuit results for the cell. The equivalent circuit shown in Figure 4.15 was used to model the AC impedance response. From the model R2 and R4 decrease under polarisation for both temperatures. R3, however, increases with polarisation for 860 °C and decreases with polarisation for 910 °C.

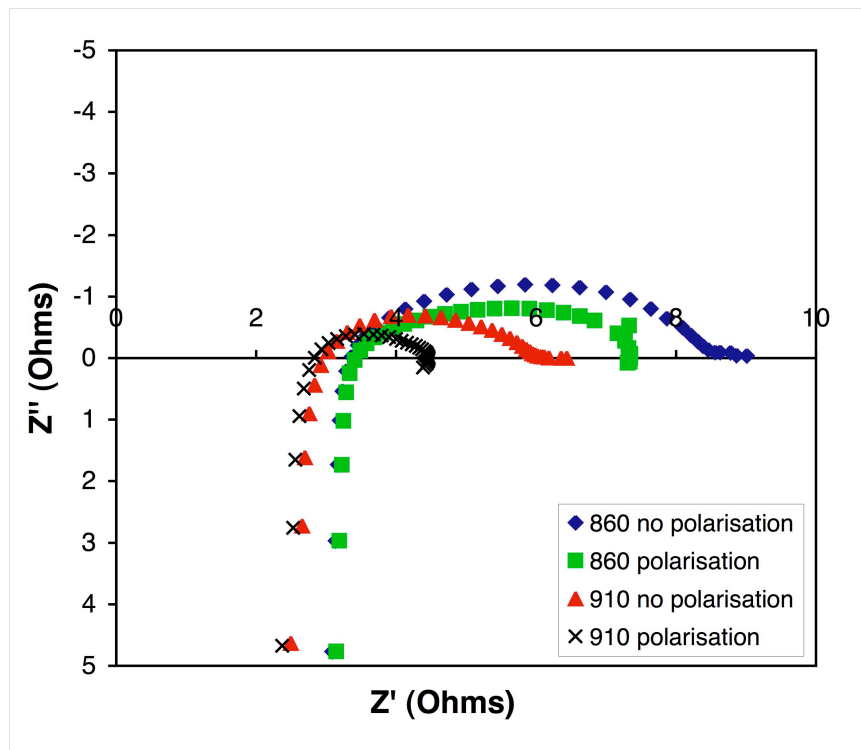


Figure 4.24: Nyquist plot of AC impedance data for LSCo electrolysis cell at 860 °C and 910 °C with and without 0.1V polarization applied to the cell.

Table 4.2: Equivalent circuit model results for electrolysis cells with LSCo anode at 860 °C and 910 °C with and without polarisation

	860 °C no polarisation	860°C polarisation	910 °C no polarisation	910 °C polarisation
L1 (H)	2.96E-06	2.94E-06	3.15E-06	3.08E-06
R1 (Ω)	3.049	3.06	1.672	2.001
R2 (Ω)	1.528	0.64287	0.41152	0.13723
CPE1T	0.008871	0.0606	0.008007	0.17395
CPE1P	0.81163	0.94154	0.92888	0.75801
R3 (Ω)	1.032	2.213	1.263	0.47669
CPE2T	0.006562	0.008924	0.000569	1.43E-05
CPE2P	0.53619	0.47511	0.48045	0.82858
R4 (Ω)	2.753	1.513	2.424	1.905
CPE3T	0.002387	0.015015	0.001414	0.005015
CPE3P	0.66641	0.67586	0.64046	0.50918

4.6 LSF anode

The electrolysis cells with LSF anode had the same decrease in resistance with increasing temperature as with the other anode materials. Figure 4.25 shows the Nyquist plot for AC impedance data for LSF anode cells, from the plot it can be seen that the resistance of the cell decreases with increasing temperature. Figure 4.26 shows a typical example of I-V plots for cells with LSF anode in the various testing atmospheres. The OCV of the Dry/Ar test is 0.75V, the measured OCV of the Steam/Ar test was somewhat lower at 0.42V. This plot is very similar to the behaviour observed for the LSM cells. The curves for the tests with Ar in the anode chamber exhibit polarisations as the current increases. The steam test has a slightly better overall performance than the dry test, and has only a very small concentration polarisation at higher currents. The area specific resistances for electrolysis tests on LSF anode cells in various atmospheres are presented in Figure 4.27.

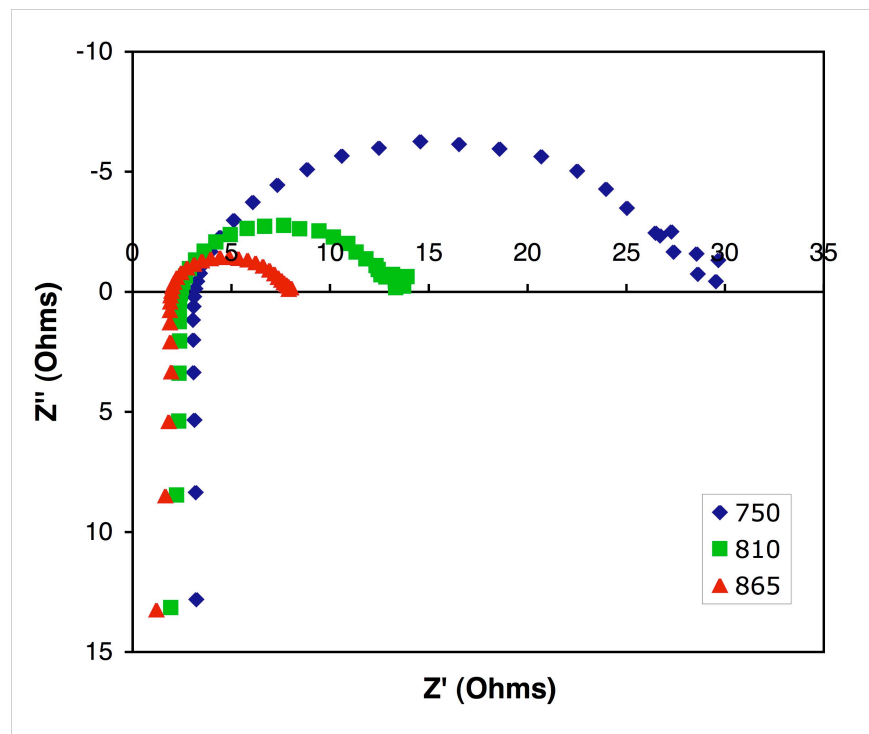


Figure 4.25: Nyquist plot of electrolysis cell with LSF anode showing decrease of resistance with increasing temperature...

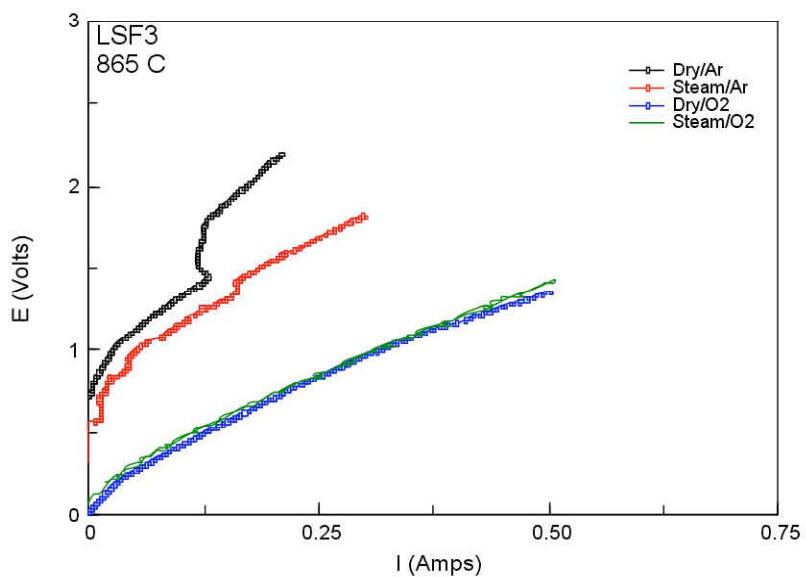


Figure 4.26: Electrolysis performance for cell with LSF anode in various gas atmosphere conditions at 865 °C.

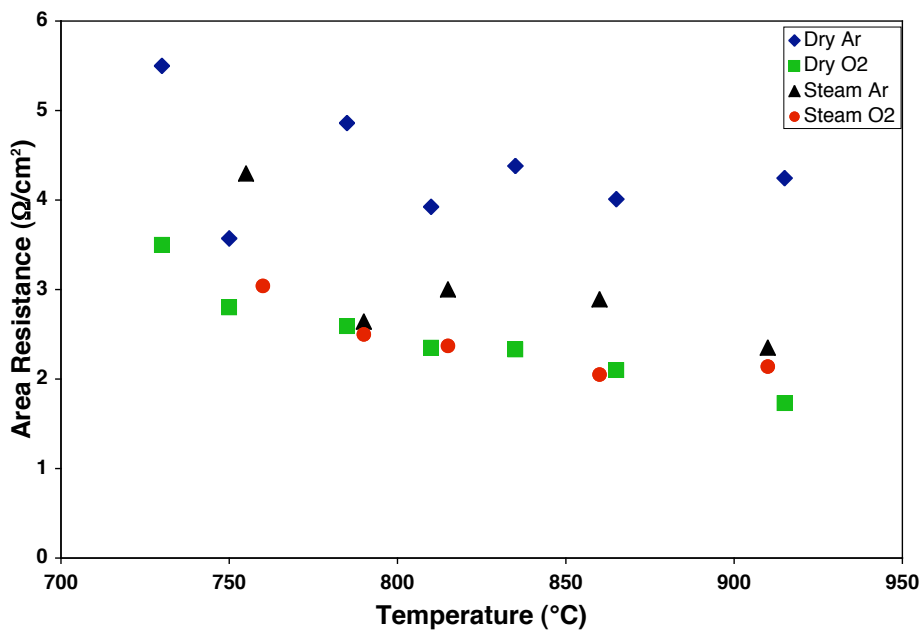


Figure 4.27: Average area resistance for all electrolysis cells with LSF anode in various gas atmosphere conditions

The same hysteresis behaviour discussed in Section 4.3.2 for the LSM anode was observed in the LSF electrolysis tests, as illustrated in Figure 4.28. The full downward sweep for 750 and 810 °C for this sample are not shown, but the concentration polarisation trend on the upward sweep can clearly be seen. The full voltage sweep for both Dry/Ar and Steam/Ar electrolysis tests at 865 C is shown in Figure 4.29. The Nyquist plots of AC impedance for tests performed under different testing atmospheres for the LSF anode cells were different for O₂ and Ar atmospheres. Unlike for LSM anodes though the Ar arcs were not completely off the scale, and more clearly showed the low frequency arc. The Nyquist plots for LSF cells in Dry/O₂ and Dry/Ar at 810 °C is shown in Figure 4.30. The LSF anode cells were tested with a polarisation applied to the cell during AC impedance testing. The polarised cell response generally decreased the magnitude of the arcs seen in Nyquist plots of the data, and increased the definition on the high frequency arcs, as seen in Figure 4.31. The data was analysed using the equivalent circuit model shown in Figure 4.15 the results of which can be seen in Table 4.3 for LSF anode cell at 810 °C polarised and unpolarised tests. The R₂ of the cell decreases with polarisation, while the other resistance elements decrease by around 1 Ω.

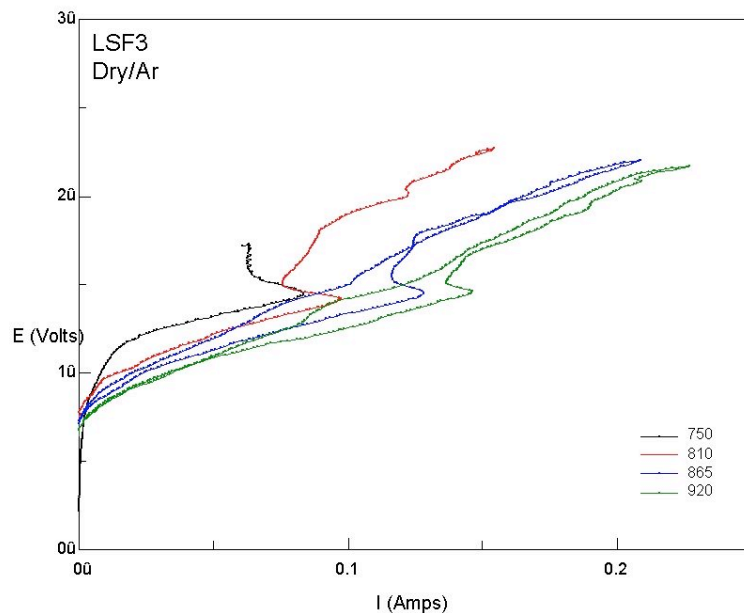


Figure 4.28: Electrolysis performance for cell with LSF anode at various temperatures in Dry/Ar atmosphere. The full $0V \rightarrow 2.2V \rightarrow 0V$ sweep is shown.

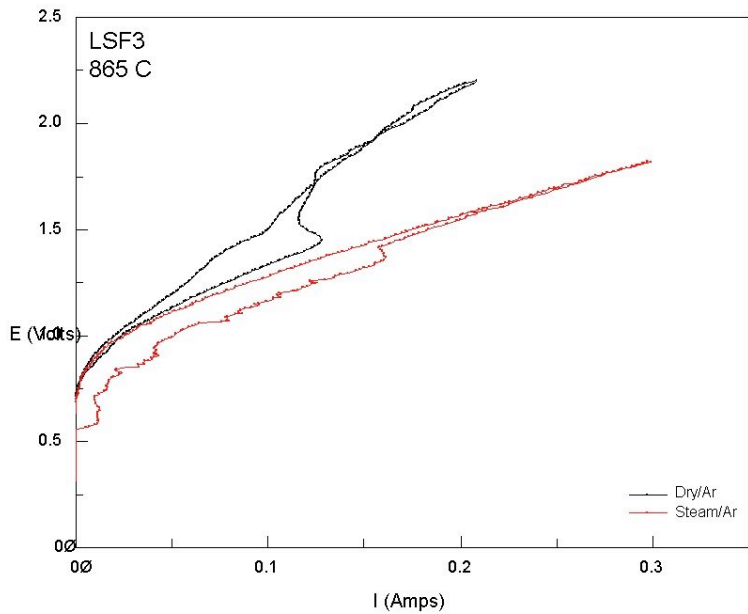


Figure 4.29: Electrolysis performance for cell with LSF anode at 865 °C in Dry/Ar and Steam/Ar atmospheres.

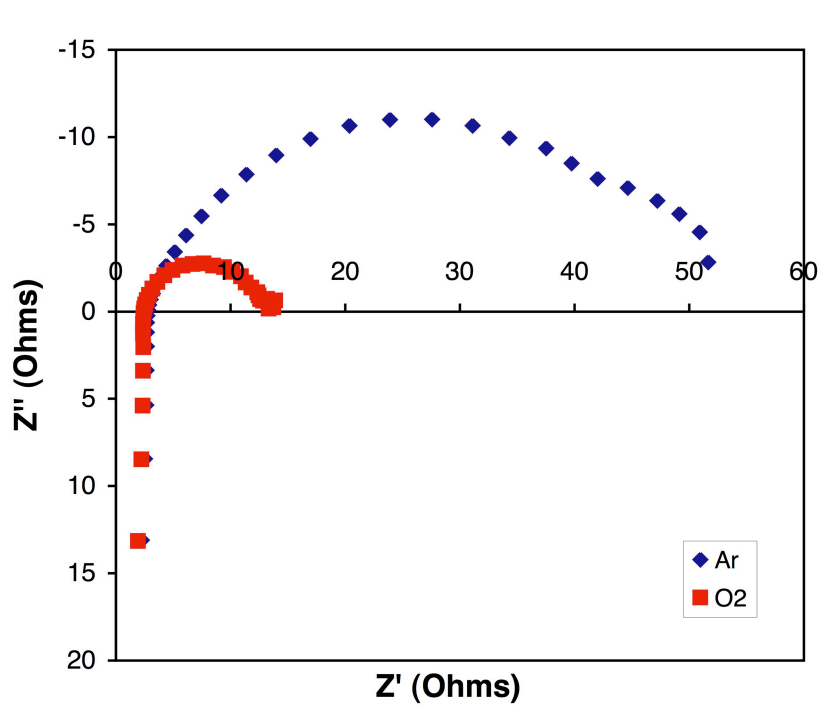


Figure 4.30: Nyquist plot of AC impedance data for electrolysis cell with LSF anode at 810 °C showing the difference in response between tests run with Ar and O₂ in the anode chamber

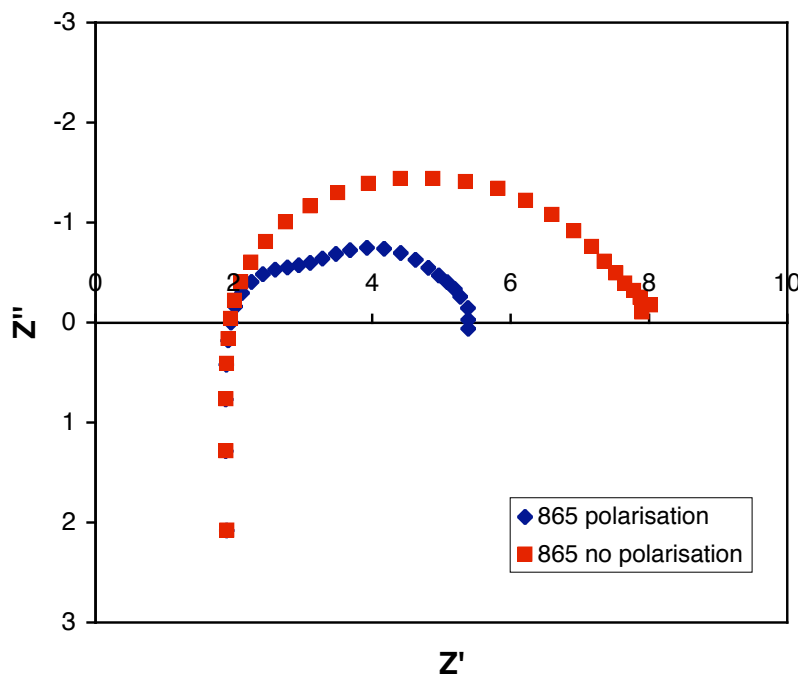


Figure 4.31: Nyquist plot of AC impedance data from an electrolysis cell with LSF anode at 865 °C, under polarization and without polarization in Dry/O₂ atmosphere.

Table 4.3: Equivalent circuit model results for electrolysis cells with LSF anode at 865 °C with and without polarisation

	865 °C no polarisation	865°C polarisation
L1 (H)	3.38E-06	3.40E-06
R1 (Ω)	1.858	1.839
R2 (Ω)	1.722	0.032411
CPE1T	0.001704	0.000271
CPE1P	0.81549	1.168
R3 (Ω)	1.089	0.85966
CPE2T	0.000491	0.000603
CPE2P	0.86262	0.82931
R4 (Ω)	3.117	2.729
CPE3T	0.008569	0.015243
CPE3P	0.6911	6.5105

4.7 Anode Material Comparison

The slope of the I-V curve corresponds to the cell resistance and is sometimes referred to as the area specific resistance (ASR). The ASR is a good way to compare the performance of different cells and different cell conditions. As with all previous ASR values, the data presented were taken from the linear fit of the cell resistance portion of the I-V curve, neglecting the activation polarisation and concentration polarisation portions of the curves, see Figure 2.3. Figure 4.32 shows the I-V curve for cells with each of the three different anode materials at 870 °C in Dry/O₂ conditions. From this result the LSF material performed best of the three although from the I-V plot an initial activation polarisation at low current can be seen in the LSF cell. The linear region of the I-V plot has a smaller slope than either the LSCo or the LSM cells. Further optimization of the LSF microstructure could minimize the polarisation.

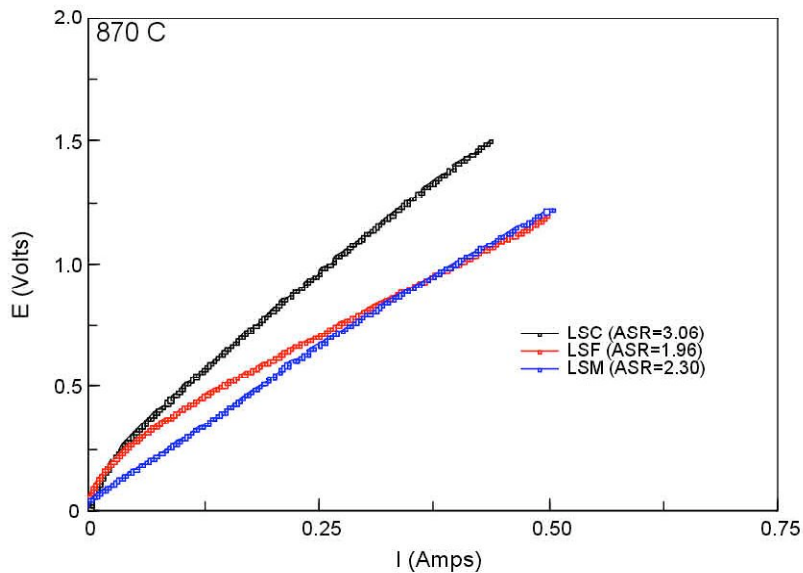


Figure 4.32: Comparison of I-V performance of electrolysis cells with LSCo, LSM and LSF anodes at 870 °C.

Figure 4.33-Figure 4.36 show the average area specific resistances for the different anode materials taken from electrolysis tests in the various gas atmosphere conditions. The ASRs for these tests were taken from the linear region of the I-V performance, neglecting the polarisations. In the plot of area resistance under the Dry/Ar condition in Figure 4.33 it can be seen that for temperatures above 775 °C all the anode materials give essentially the same response, with only slight improvement with increasing temperature. The LSM and LSF area resistances in the Dry/O₂ atmosphere, shown in Figure 4.34, follow the same trend, while the LSCo resistance is much higher at all temperatures. Under the Steam/Ar condition, presented in Figure 4.35, the LSF gives the best response, with little change with increasing temperature. Apart from low temperatures the LSCo area resistance is better than LSM under Steam/Ar. The LSF material under Steam/O₂ again shows the best response, as seen in Figure 4.36. The LSF is only slightly better than the LSM under this condition though, with the LSCo material performing the worst.

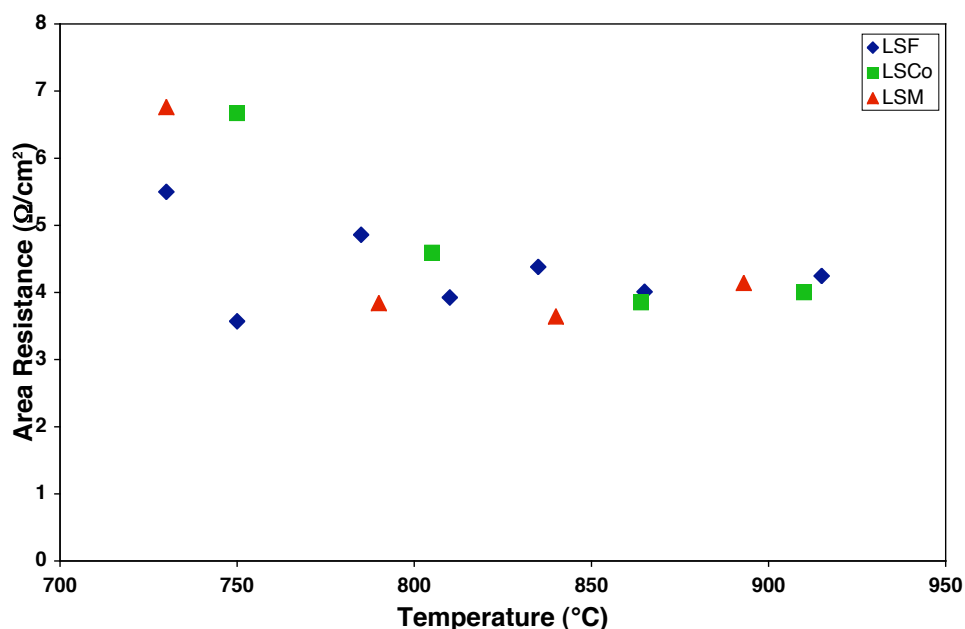


Figure 4.33: Average area resistance for electrolysis cells in Dry/Ar atmosphere

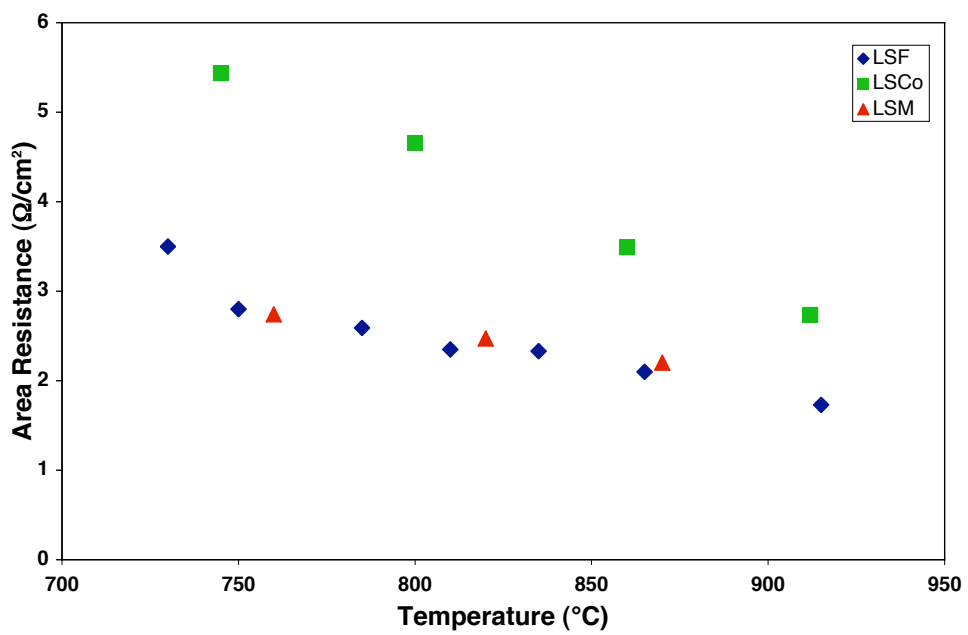


Figure 4.34: Average area resistance of electrolysis cells in Dry/O₂ atmosphere

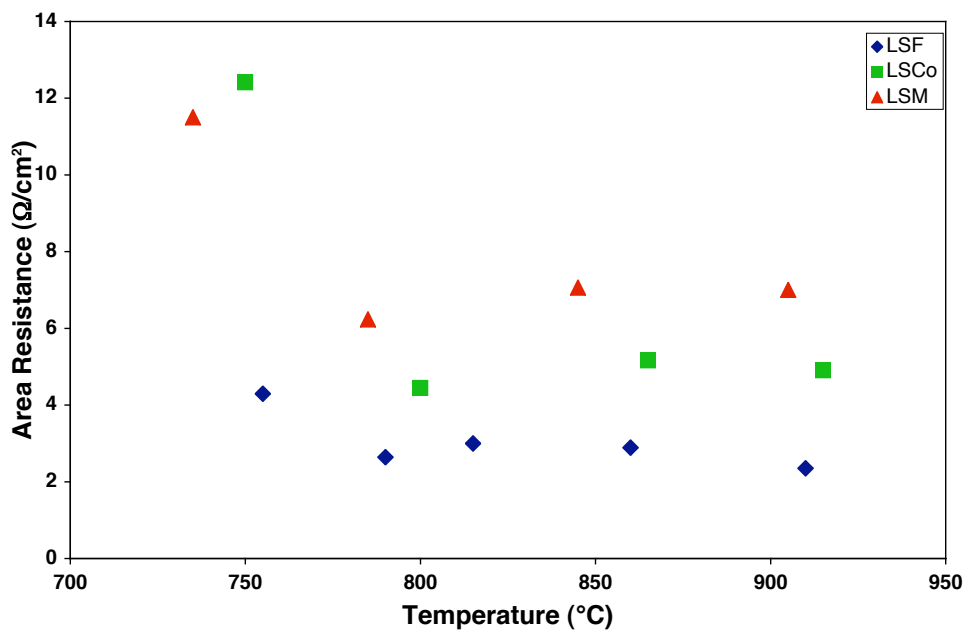


Figure 4.35: Average area resistance for electrolysis cells in Steam/Ar atmosphere

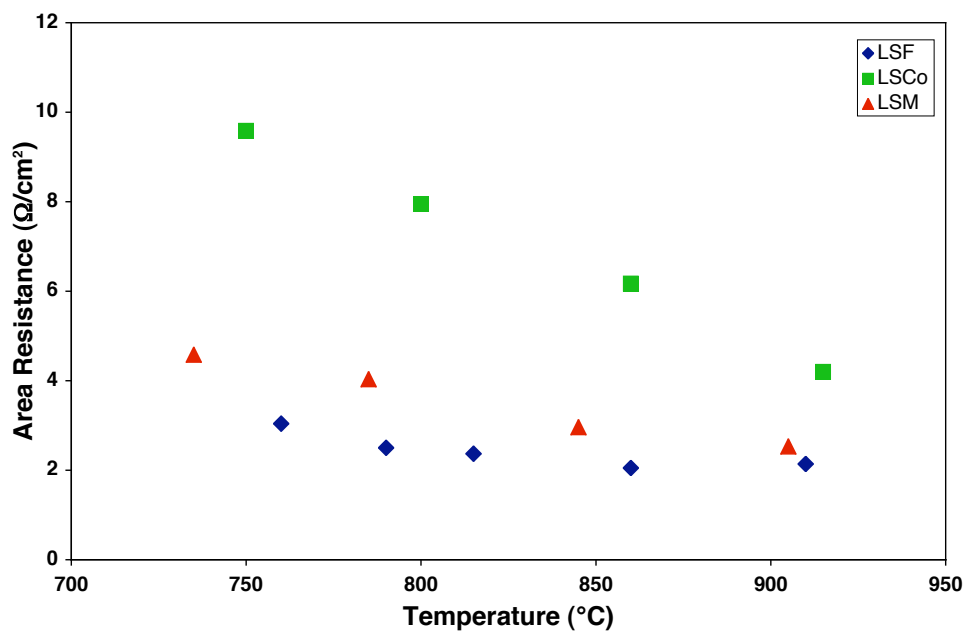


Figure 4.36: Average area resistance of electrolysis cells
in Steam/O₂ atmosphere

References

- ¹ Takeda, Y., Kanno, R., Noda, M., Tomida, Y., and Yamamoto, O. "Cathodic Polarization Phenomena of Perovskite Oxide Electrodes With Stabilized Zirconia." *Journal of the Electrochemical Society* 134 (1987): 2656-61.
- ² Eguchi, K., Hatagishi, T., and Arai, H. "Power Generation and Steam Electrolysis Characteristics of an Electrochemical Cell With Zirconia-Or Ceria-Based Electrolyte." *Solid State Ionics* 86-88 (1996): 1245-49.
- ³ Hino, R., Haga, K., Aita, H., and Sekita, K. "R&D on Hydrogen Production By High-Temperature Electrolysis of Steam." *Nuclear Engineering and Design* 233 (2004): 363-75.
- ⁴ Herring, J.S., Lessing, P.A., O'Brien, J.E., and Stoots, C. "High-Temperature Solid-Oxide Electrolyzer System." *DOE Hydrogen Program* (2004):
- ⁵ Minh, N., "Ceramic Fuel Cells." *Journal of the American Ceramic Society*, 76 (1993): 563-588.
- ⁶ Ringuede, A., and Fouletier, J. "Oxygen Reaction on Strontium-Doped Lanthanum Cobaltite Dense Electrodes At Intermediate Temperatures." *Solid State Ionics* 139 (2001): 167-177.
- ⁷ Balachandran, U., Dusek, J.T., Mieville, R.L., Poeppel, R.B., Kleefisch, M.S., Pei, S., Kobylinski, T.P., Udovich, C.A., and Bose, A.C. "Dense Ceramic Membranes for Partial Oxidation of Methane to Syngas." *Applied Catalysis A* 133 (1995): 19-29.
- ⁸ Manoharan, R., and Shukla, A.K. "Oxides Supported Carbon Air-Electrodes for Alkaline Solution Power Devices." *Electrochimica Acta* 30 (1985): 205.
- ⁹ Teraoka, Y., Zhang, H.M., Okamoto, K., and Yamazoe, N. "Mixed Ionic-Electronic Conductivity of $\text{La}_{1-x}\text{Sr}_x\text{Co}_{1-y}\text{Fe}_y\text{O}_{3-\delta}$ Perovskite-Type Oxides." *Materials Research Bulletin* 23 (1988): 51-58.
- ¹⁰ Mizusaki, J., Tabuchi, J., Matsuura, T., Yamachi, S., and Fueki, K. "Electrical Conductivity and Seebeck Coefficient of Nonstoichiometric $\text{La}_{1-x}\text{Sr}_x\text{CoO}_{3-\delta}$." *Journal of the Electrochemical Society* 136 (1989): 2082-88.
- ¹¹ Petric, A., Huang, P., and Tietz, F. "Evaluation of La-Sr-Co-Fe-O Perovskites for Solid Oxide Fuel Cells and Gas Separation Membranes." *Solid State Ionics* 135 (2000): 719-25.
- ¹² Ralph, J.M., Schoeler, A.C., and Krumpelt, M. "Materials for Lower Temperature Solid Oxide Fuel Cells." *Journal of Material Science* 36 (2001): 1161-72.
- ¹³ Mai, A., Haanappel, V., Uhlenbruck, S., Tietz, F., and Stover, D. "Ferite-Based Perovskites as Cathode Materials for Anode-Supported Solid Oxide Fuel Cells. I. Variation of Composition." *Solid State Ionics* 176 (2005): 1341-50.
- ¹⁴ Millini, R., Gagliardi, M.F., and Piro, G. "Structure, Stoichiometry and Phase Purity of Strontium-Doped Lanthanum Manganite Powders." *Journal of Material Science* 29 (1994): 4065-69.

¹⁵ van Roosmalen, J.A.M., and Cordfunke, E.H.P.. Chemical reactivity and interdiffusion of (La,Sr)MnO₃ and (Zr,Y)O₂ solid oxide fuel-cell cathode and electrolyte materials. *Solid State Ionics* 52 (1992): 303-312.

¹⁶ Wiik, K., Shmidt, C.R., Faaland, S., Shamsili, S., Einarsrud, M.A., and Grande, T. Reactions between strontium-substituted lanthanum manganite and Yttria-stabilized zirconia: I. Powder samples. *Journal of the American Ceramic Society* 82 (1999): 721-728.

¹⁷ Figueiredo, F.M., Labrincha, J.A., Frade, J.R., and Marques, F.M.B. "Reactions Between a Zirconia-Based Electrolyte and LaCoO₃-Based Electrode Materials." *Solid State Ionics* 101-103 (1997): 343-49.

¹⁸ Labrincha, J.A., Frade, J.R., and Marques, F.M.B. "La₂Zr₂O₇ Formed at Ceramic Electrode/YSZ Contacts." *Journal of Material Science* 28 (1993): 3809-15.

¹⁹ Uchida, H., Arisaka, S., and Watanabe, M. "High Performance Electrodes for Medium-Temperature Solid Solid Oxide Fuel Cells: Activation of La(Sr)CoO₃ Cathode With Highly Dispersed Pt Metal Electrocatalysts." *Solid State Ionics* 135 (2000): 347-51.

²⁰ Shiono, M., Kobayashi, K., Nguyen, T.L., Hosoda, K., Kato, T., Ota, K., and Dokiya, M. "Effect of CeO₂ Interlayer on ZrO₂ Electrolyte/La(Sr)CoO₃ Cathode for Low-Temperature SOFCs." *Solid State Ionics* 170 (2004): 1-7.

²¹ Simner, S.P., Bonnett, J.F., Canfield, N.L., Meinhart, K.D., Sprenkle, V.L., and Stevenson, J.W. "Optimized Lanthanum Ferrite-Based Cathodes for Anode-Supported SOFCs." *Electrochemical and Solid-State Letters* 5 (2002): a173-a175.

²² Simner, S.P., Shelton, J.P., Anderson, M.D., and Stevenson, J.W. "Interaction Between La(Sr)FeO₃ SOFC Cathode and YSZ Electrolyte." *Solid State Ionics* 161 (2003): 11-18.

²³ Gamry Instruments <http://www.gamry.com/Products/EIS300.htm> © 1997-2006

Chapter 5: Electrolyser Tube Development

5.1 Introduction	129
5.1.1 Closed-end tape cast electrolysis tubes	129
5.2 Tube Development	131
5.2.1 SEM characterisation	131
5.2.2 Initial tube configuration.....	134
5.2.3 Tube flaws.....	134
5.2.4 Cathode formulation	136
5.2.5 Sinter rate	136
5.2.6 Thin tapes.....	137
5.2.7 Electrolyte thickness	139
5.2.8 Tube length	140
5.2.9 Isostatic pressing.....	141
5.3 Manganese Deficiency.....	142
5.4 Dilatometry	146
5.5 Electrolysis Testing	148
5.6 Performance of Electrolysis Tubes	151
5.7 Tube Comparison.....	153
References	156

5.1 *Introduction*

5.1.1 Closed-end tape cast electrolysis tubes

There are two standard design configurations for solid oxide fuel cells and electrolyzers: a planar design and a tubular design, shown in Figure 5.1. In the planar design, the components are assembled in flat stacks, with air and fuel flowing through channels built into the cathode and anode. In the tubular design, components are assembled in the form of a hollow tube, with the cell constructed in layers around a tubular cathode; air flows through the inside of the tube and fuel flows around the exterior. Both standard configurations have advantages and disadvantages. Generally planar cells are fragile and require high temperature seals for gas separation. Tubular cells have a higher mechanical strength than planar cells, but tubular cells usually require many processing steps, often involving expensive deposition equipment. In addition the different material components used in both designs must be processed and sintered separately, adding to the production time and cost.

The design chosen for the electrolysis cells in this work, illustrated in Figure 5.2, is based on the more robust tubular design, but without the attending disadvantages of the standard tubular design. The electrolyser is based on an LSM anode supported tube, with thin outer layers of YSZ electrolyte and Ni-YSZ cermet cathode. Details of the fabrication can be found in section 3.1.7.

The electrolyser tubes were fabricated from flexible tape cast ceramic anode, electrolyte, and cathode materials, which were then rolled together to form a tube. The subsequent heat treatment and sintering are performed on complete cells in a single step. The tape case tube design eliminates the need for interconnect materials. Gas tight sealing is still required, but the closed-end tube design requires only one ceramic to metal join, without extensive sealing between all materials of the cell, as found in a planar cell. Tape casting is an inexpensive ceramic processing technique together with the co-firing of all component layers makes for cost effective and simple processing.

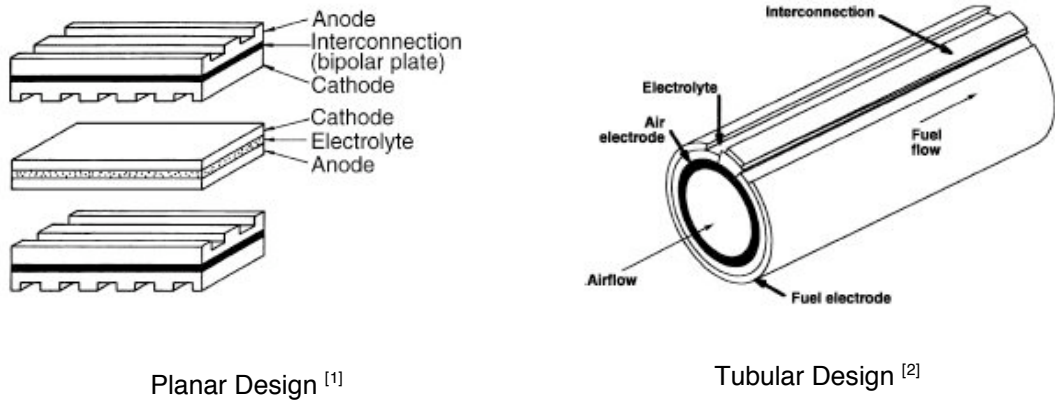


Figure 5.1: Two standard design configurations of SOFCs

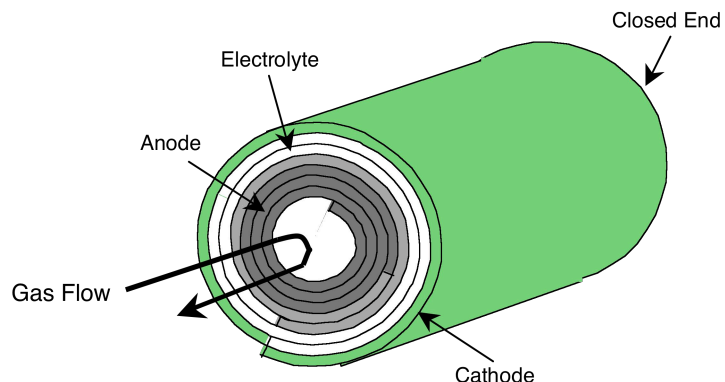


Figure 5.2: Tape cast electrolyser tube design

5.2 *Tube Development*

5.2.1 SEM characterisation

The following sections will contain secondary electron (SE) images of various tubes and tube features obtained from the scanning electron microscope (SEM). The SE images will generally show only a portion of the tube cross-section. Figure 5.3 is a composite of several SE images of a tube arranged to show the entire tube cross-section.

Figure 5.4 is a portion of the tube cross-section used to indicate the different layers in the tube. All subsequent SE images will have the same basic layout with the layers as shown.

Different types of cracks can be seen throughout the cross-section of the tube. Some cracks were present before impregnation with epoxy resin. These cracks are evidence of flaws in the tubes or of failures that occurred during testing. The cracks due to flaws and failures will contain epoxy, indicating that the crack was present prior to impregnation. Additional cracks are caused by the epoxy, which shrinks upon curing. These cracks tend propagate along the direction of the tape windings, sometimes through the electrolyte layer, other times causing a delamination between differing layers. The cracks caused by the curing of the epoxy will not contain resin. Figure 5.5 shows the two different kinds of cracks; the red arrow indicates a failure crack present prior to impregnation, and the blue arrow indicates a crack caused by the shrinking of epoxy.

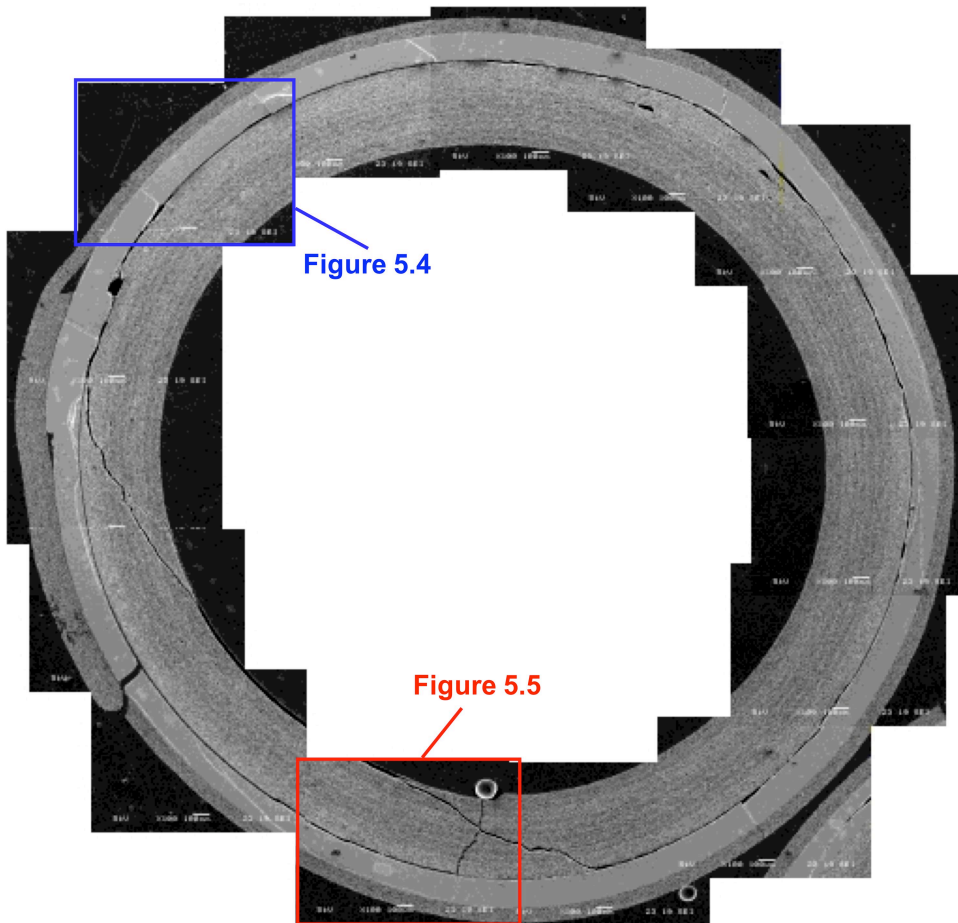


Figure 5.3: Composite photo of tube cross-section

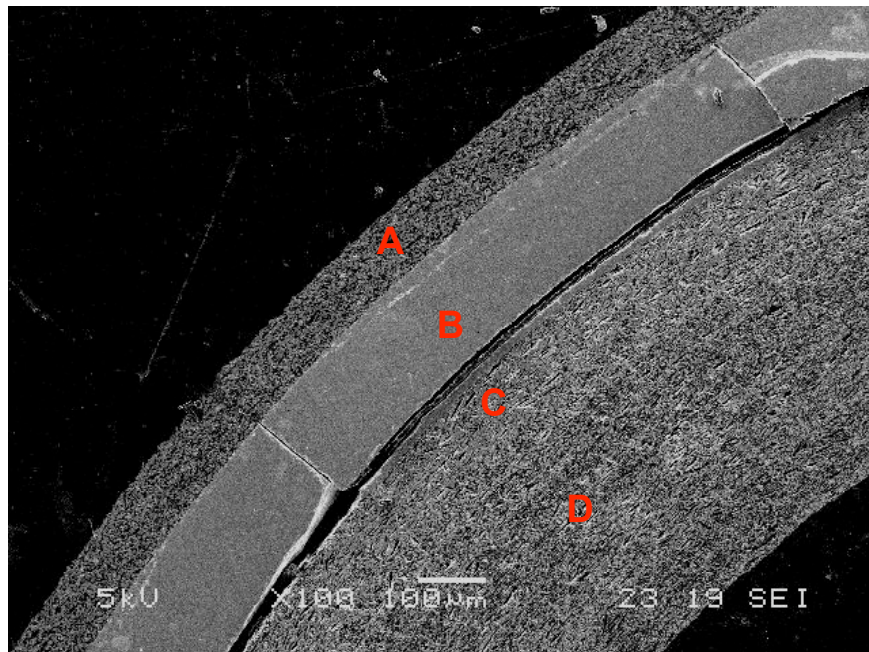


Figure 5.4: SE image of a portion of the tube cross-section, showing the different layers of the tube, A) porous NiO-YSZ active cathode, B) dense YSZ electrolyte, C) porous LSM+YSZ active anode, and D) porous LSM anode current collector.

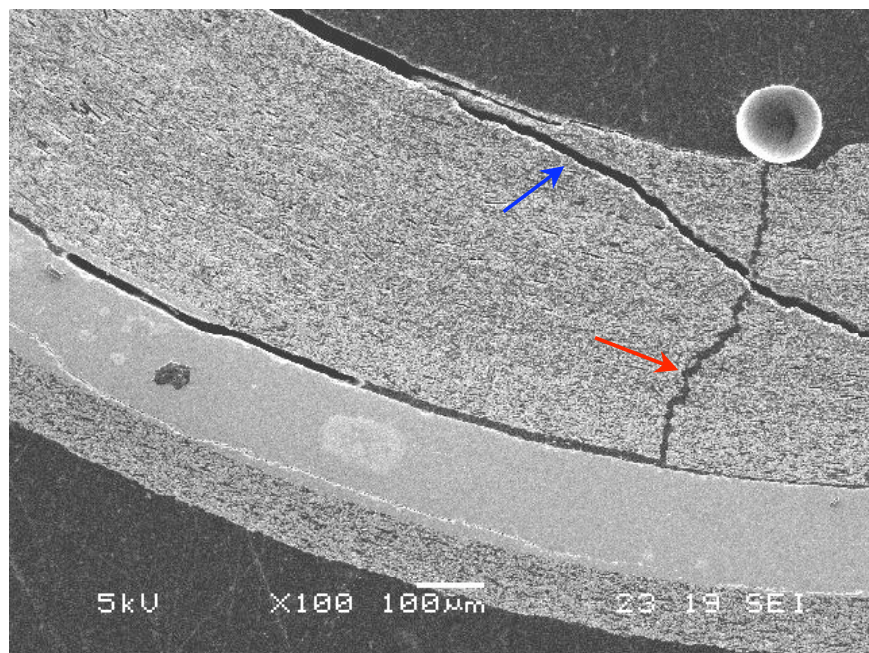


Figure 5.5: SE image illustrating the cracks seen in the tube cross-sections. The red arrow indicates crack impregnated with epoxy, and the blue arrow indicates a crack with an absence of epoxy.

5.2.2 Initial tube configuration

The initial tape processing and rolling techniques were adapted from the previous work of Jones.^[3] The tubes are based on an LSM anode-supported design, with a thick inner anode layer as a mechanical support to the thin YSZ electrolyte and Ni-YSZ cathode layers. The first design employed to make tubes was not ideal. In this initial design all three layers, anode, electrolyte, and cathode, extended to the bottom of the tube as illustrated in Figure 5.6 (a). This design was flawed because the cathode and anode could be easily short-circuited by the silver paint contact material. The design was revised to the one shown in Figure 5.6 (b). This design had a shorter width of cathode, which provided an area of electrolyte around the bottom of the tube to further separate the cathode and anode layers, thus avoiding a short circuit.

5.2.3 Tube flaws

Some tubes had visible cracks in the NiO-YSZ. Visual inspection was not sufficient to determine if the cracks continued through the electrolyte layers. Therefore, the tubes were sealed onto the steel supports and then submersion tested. Many of the tubes with visible external cracks leaked air during the submersion test, as described in section 3.2.2, thus it was thought that the external cracks might indicate a stress point or flaw in the interior of the tube. As a result, tubes containing visible external flaws were not used in any electrolysis tests. A few tubes had brown spots on the green NiO-YSZ exterior. This was an indication of manganese diffusion through cracks or flaws in the electrolyte from the inner LSM layers. Tubes with the brown spots were deemed unsuitable for further testing. Figure 5.7 shows two tubes containing flaws. The tube on the left contains cracks at the seams and a fold in the Ni-YSZ tape, as indicated by the arrows. The tube on the left displays a brown spot where manganese has come through the electrolyte, as indicated by the arrow.

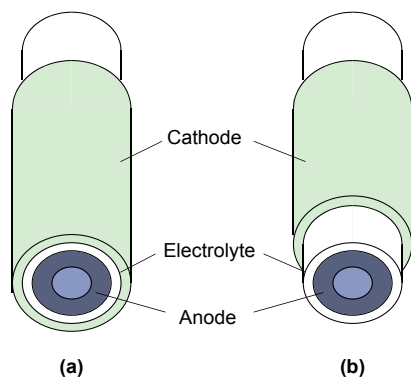


Figure 5.6: (a) Original tube design and (b) revised tube design with shorter cathode to prevent short circuit.

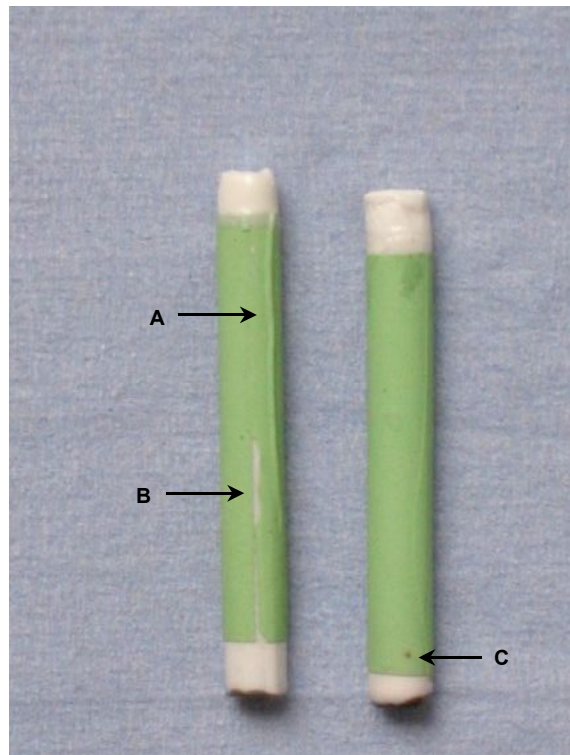


Figure 5.7: Tube flaws: a) fold, b) crack and c) brown spot where MnO_2 diffused through a flaw in the electrolyte

5.2.4 Cathode formulation

There were three formulations for the cathode tapes designated here as A, B, and C. These formulations were initially developed by Jones and designated 14A, 15A and 25A respectively.^[3] The formulations are tabulated in Table 5.1.

Table 5.1: Cathode tape formulations

Cathode	Ni content	Graphite content	Porosity
A	low	medium	medium
B	high	low	low
C	medium	high	high

Sample tubes were prepared using tapes of cathode A and cathode B. Tubes prepared with cathode A contained very few flaws. Cathode B had better electrical conductivity due to the high nickel content, but after sintering, the cathode layer was cracked and in some cases flaked off the tube completely. Sample tubes were then prepared with layers of A, which adhered well to the electrolyte, and a final layer of cathode C for improved electrical conductivity. The layer of C cracked and flaked away from the layers of A. As a result, Cathode A was used exclusively in all subsequent tubes.

5.2.5 Sinter rate

Initially, the tubes were sintered with a simple “fast” heating rate of 0.5 °C/min to 1000°C for binder burnout, followed by 5 °C/min to 1350 °C. This heating rate resulted in cracks along the seams of approximately half of the tubes. All the green tapes used were roughly the same thickness, but there was nearly always some gap between the tapes as the tube was rolled, and these gaps or seams were the source of many of the flaws in the tubes.

A more detailed “slow” heating rate developed by Jones^[3] for co-firing of the SOFCRoll materials was then adopted for sintering the electrolysis tubes in an attempt to prevent cracks upon sintering. The different materials of the tubes shrink at different rates upon heating, this shrinkage can cause stresses, which result in cracks in the sintered tube. The slow heating rate takes into consideration the different shrinkage times and temperatures

of each of the materials to allow for co-firing of all layers with a minimum of stress and cracks.

5.2.6 Thin tapes

As described in section 5.2.5, cracks often formed in the sintered tubes at the tape seams. The gap at the seams might be sites for the initiation of cracks. In an attempt to reduce the size of the gaps and prevent the cracking, thinner tapes were cast and used to fabricate tubes. The original green tape thicknesses were 0.6-0.7 mm with a corresponding sintered tape thickness of roughly 60 μm . The green thin tape thicknesses were 0.3-0.35 mm with a corresponding sintered tape thickness of approximately 25 μm . Figure 5.8 is an SE image of a tube fabricated with the thick tapes. A seam, approximately 60 μm high, in the YSZ can be seen with a crack at the corner of the seam. It should be noted that the crack in Figure 5.8 is filled with epoxy resin thus indicating that the crack was present prior to impregnation with epoxy. Figure 5.9 is an SE image of a tube fabricated with the thin tapes. The seam in the thin tape tube is approximately 25 μm . The crack at the corner of the seam in the thin tube is not filled with epoxy resin, indicating that crack was caused by the epoxy shrinkage during curing. This indicates a possible weak spot in the tube, but the tube was not cracked prior to mounting in epoxy.

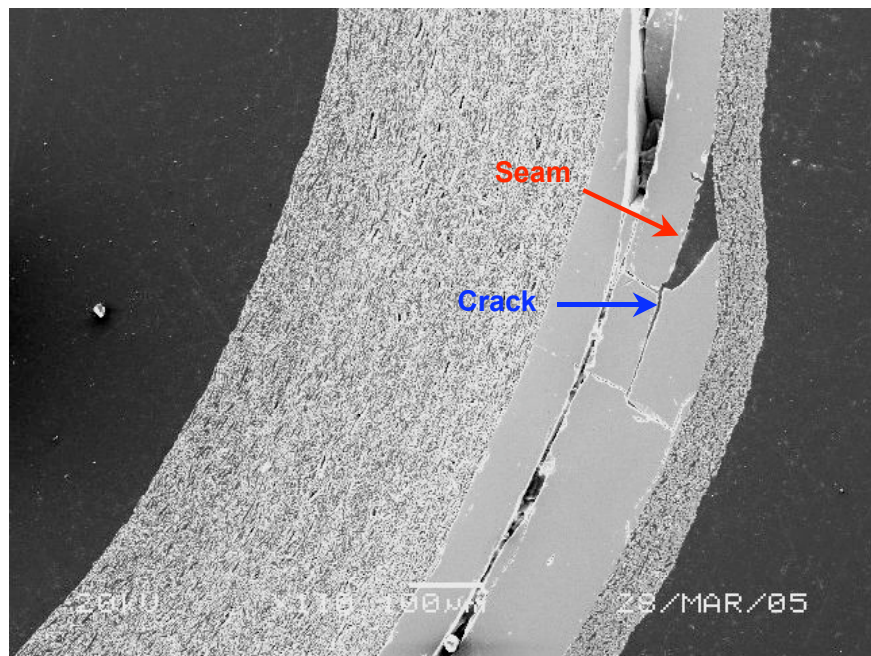


Figure 5.8: SE image showing a seam in the YSZ electrolyte layer of a tube made with regular tapes, indicated by the red arrow and a crack originating from the seam, indicated by the blue arrow.

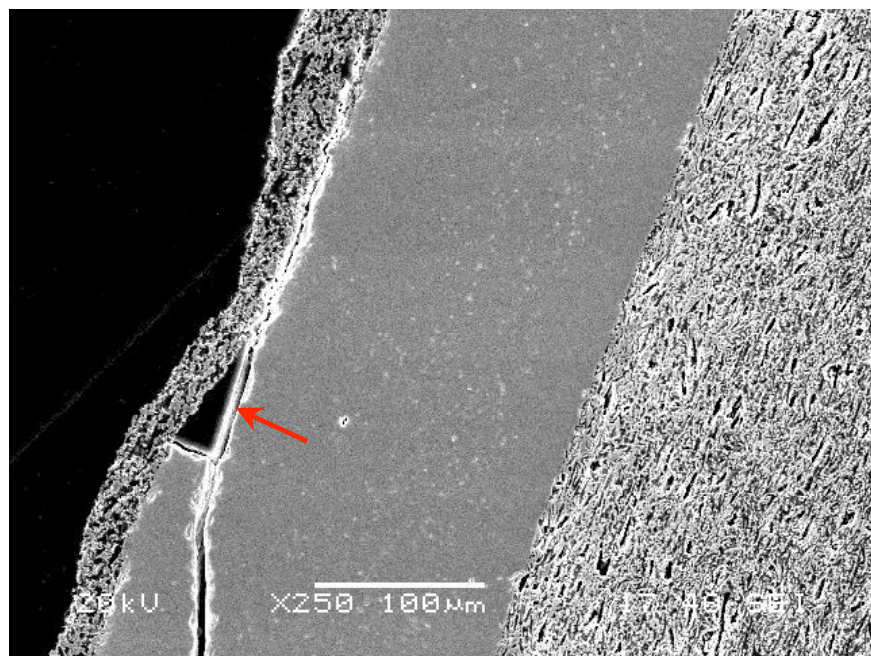


Figure 5.9: SE image showing the gap left by a seam in the YSZ electrolyte layer of a tube made with thin tapes.

The thin tapes did reduce the size of the gaps left by the tape seams, but ultimately the thin tapes proved unsuitable. The thin tapes contained more flaws in the electrolyte, and

as a result the sintered tubes developed numerous brown spots. These thin green tapes were more difficult to work with and roll properly. The resulting tubes were more fragile and contained many wrinkles and flaws as a consequence of the tapes being difficult to handle. Figure 5.10 shows an example of the edge of the YSZ tape after it was folded over, leaving a large gap and resulting in an even larger seam. The outer Ni-YSZ layer in this tube was cracked nearly the entire length of the seam as seen from the outside; this condition was most likely a result of the YSZ fold.

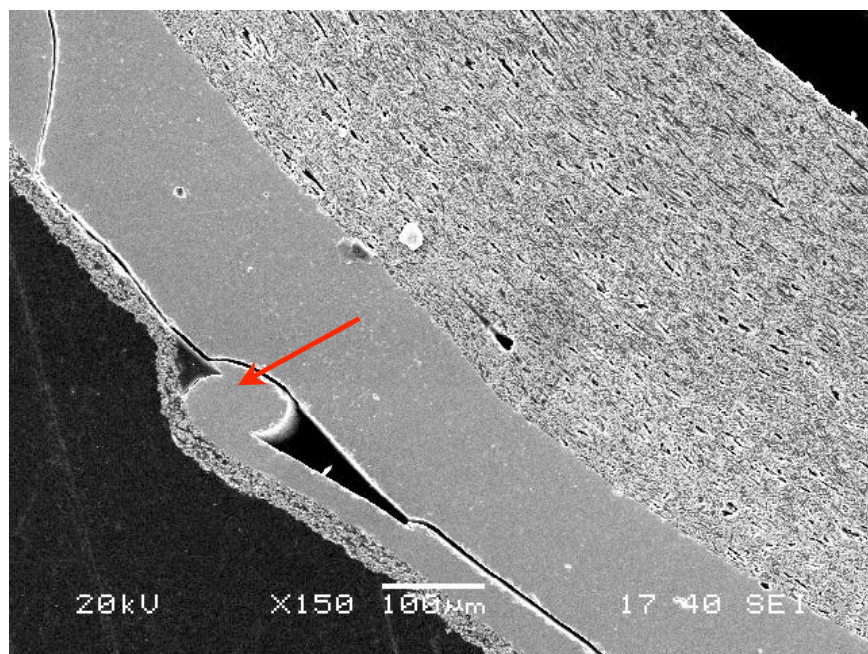


Figure 5.10: SE image showing a thin-tape tube with a fold along the edge of the YSZ electrolyte tape, as indicated by the arrow.

5.2.7 Electrolyte thickness

The first tubes electrolysis tested were found to fail between 800 and 850 °C. The tubes cracked at or very near the location where the steel support tube connected to the ceramic electrolysis tube. The steel support tubes were fabricated from 316 stainless steel. This steel has a coefficient of thermal expansion much greater than the ceramic components in the electrolysis tube and the sealing material. These values are tabulated in Table 5.2. The thermal expansion mismatch between the materials will be discussed further in section 5.4.

Table 5.2: Coefficient of thermal expansion for tube component materials

Material	Coefficient of thermal expansion
316 stainless steel	16 $\mu\text{m}/\text{m}\cdot^\circ\text{C}$, 20°C 17.5 $\mu\text{m}/\text{m}\cdot^\circ\text{C}$, 500°C
YSZ	10.5 $\mu\text{m}/\text{m}\cdot^\circ\text{C}$
LSM	11 $\mu\text{m}/\text{m}\cdot^\circ\text{C}$
Ni-YSZ	10.5 $\mu\text{m}/\text{m}\cdot^\circ\text{C}$
Ceramic adhesive	7.7 $\mu\text{m}/\text{m}\cdot^\circ\text{C}$

Tubes with thicker electrolyte were fabricated in an attempt to alleviate the problem of the tubes failing above 800 °C. The original tubes had two layers of electrolyte. New tubes were made with three and four layers. Each layer of electrolyte is roughly 50-60 μm thick after sintering. The tubes with thicker layers improved the mechanical strength of the tubes, but decreased the electrolysis performance as expected for a thicker electrolyte. The thicker layers reduced the number of tubes exhibiting brown spots as well, so even if there was a flaw in one layer of electrolyte the additional layers prevented the flaw from ruining the tube. The tubes with thicker electrolytes continued to fail above 800 °C, but the reduction in flaws was beneficial.

5.2.8 Tube length

Another attempt to prevent the cracking from the thermal expansion mismatch of the steel was to fabricate longer electrolysis tubes. The original tubes were 4.5 cm long. The long tubes had a length of 8.0 cm. With the longer tubes, the steel joint would be further from the hotspot in the furnace. The joint area could be as much as 250-300 °C cooler than the temperature of the tube in the region of the hotspot. With the joint area well below the operating temperature, this allowed for the electrolyser to be operated at higher temperature and improved the tube lifetime. One drawback of the longer tubes was that there was a large area of active tube that was not electrolysing at the operating temperature. Another problem with the long tubes was bending during sintering. The tubes were sintered in an upright position to preserve the round shape, and as a result the tubes would sometimes slump or bend slightly in the furnace. Figure 5.11 shows all three

sizes of the tubes used. The long tube pictured on the right shows the slight bending, although in the case of this tube the bending was not so severe as to prevent testing. An intermediate tube length of 6.5 cm was decided upon. The short one on the left represents the initial length used, while the tube in the middle is the final design.

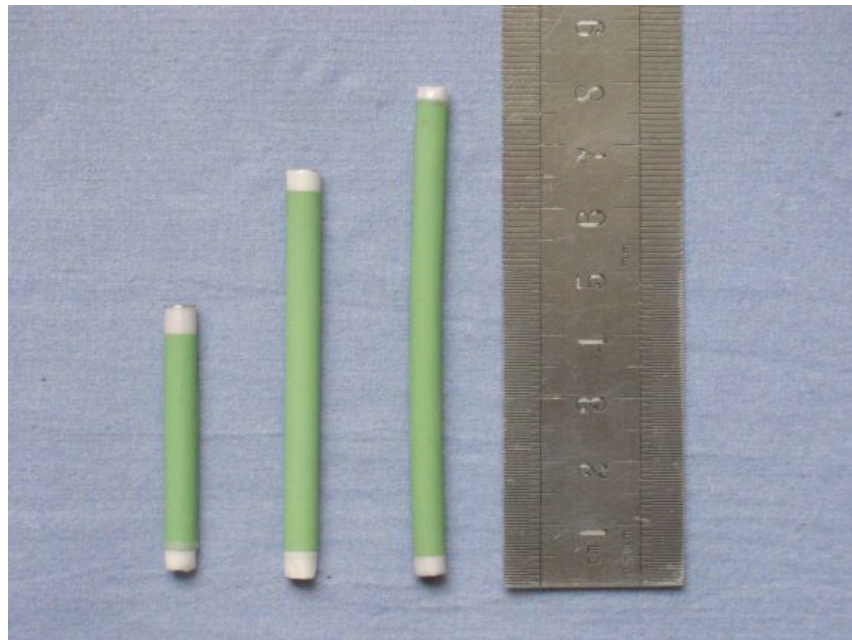


Figure 5.11: Three tube sizes, initial short design, final intermediate length design, and long design, from left to right respectively.

5.2.9 Isostatic pressing

The final improvement to the tube design was to include an isostatic pressing step into the fabrication process. Before heat treatment and sintering the green tubes were put in an isostatically pressed to 230 MPa (34,000 psi). The pressing step was added to improve the strength, durability and structure of the tubes. The pressing improved the lamination between the layers of tape and between the different materials. The seams between the YSZ and electrode materials were still present after pressing, but cracks did not seem to develop from these seams as before.

5.3 Manganese Deficiency

An EDS examination was performed on the tube cross-sections. Element map of the various layers of the tubes were generated. Upon examination an unusual feature was seen in the region of the interface between the LSM anode current collector and the LSM+YSZ composite interlayer. The interlayer is made of A-site deficient LSM mixed with YSZ. One function of the interlayer is to prevent an unfavourable reaction between the LSM anode and the YSZ electrolyte. The composite interlayer improves the cell performance by providing mixed conduction through the layer: oxygen ions through the YSZ and electrons through the LSM, thereby extending the oxygen reaction from the electrolyte/electrode interface into the electrode region.^[4,5] The durability of the cell is also improved because the interlayer helps to bridge the small difference in thermal expansion coefficient between the YSZ and LSM. The element maps revealed a manganese-deficient zone in the interlayer at the anode-interlayer interface. Figure 5.12-
Figure 5.14 show SE images of the regions and the element maps of the various elements for several tubes. It can be seen from the element maps that the lanthanum in the region is unaffected. Figure 5.12 shows a tube made from standard tapes. This tube had also been sealed and used in electrolysis testing. Figure 5.13 shows also a tube made from standard tapes, but had not been used in electrolysis tests. This indicates that the Mn-deficient region was independent of whether the tube had been tested. Figure 5.14 shows a tube made from thin tapes. The Mn-deficient region is present in this tube as well. In each case the region is approximately 5 μm . In the thin-tape tube the interlayer is only 17-20 μm thick, so the Mn-deficient region represents a larger percentage of the total layer.

The cause of the Mn-deficient region in the composite interlayer is not fully understood.. The Mn-deficient region could have been formed by Mn diffusion during sintering of the tubes between the intermediate layer and the anode layers. The extent of the effect this Mn-deficient region has on the performance of the tubes is not known, and is an issue that must be addressed.

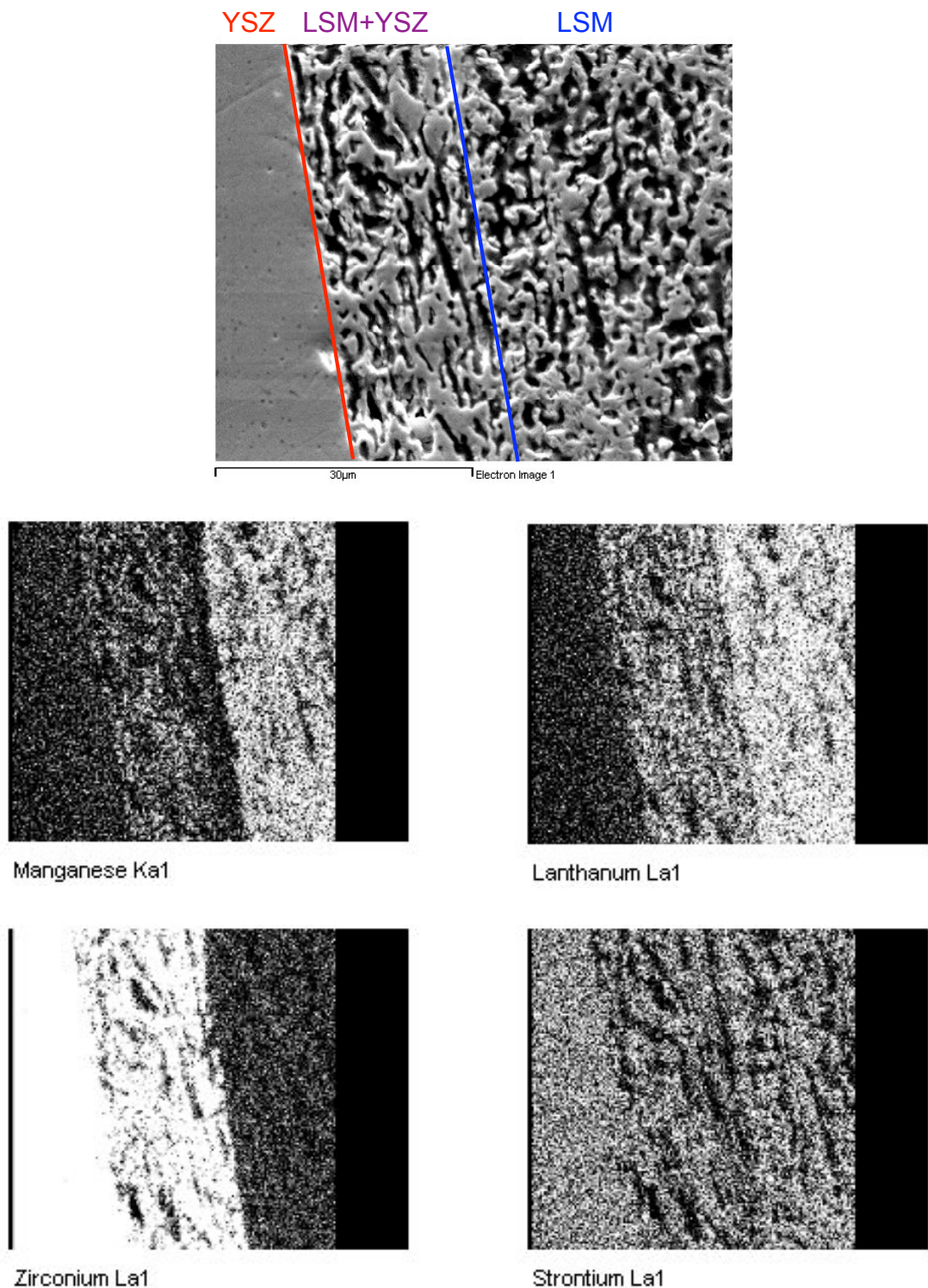
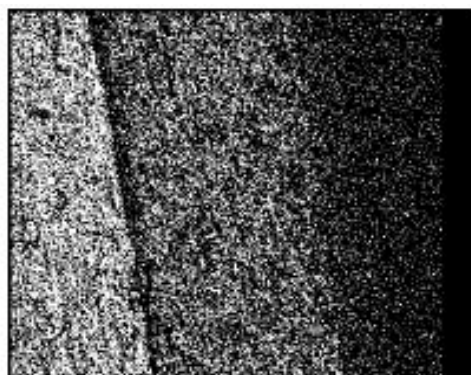
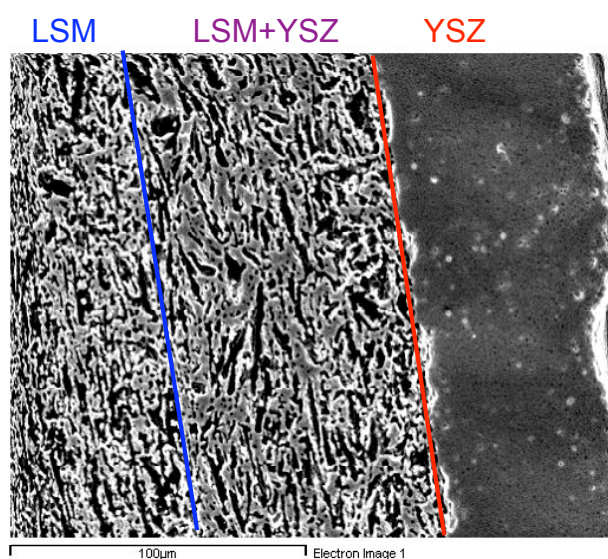
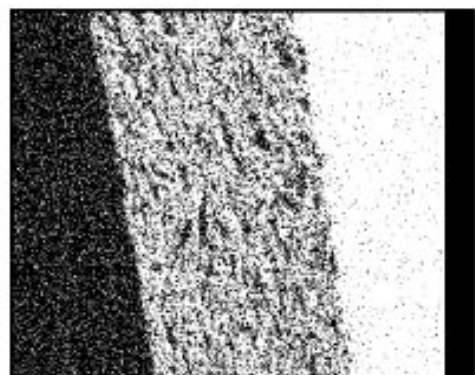


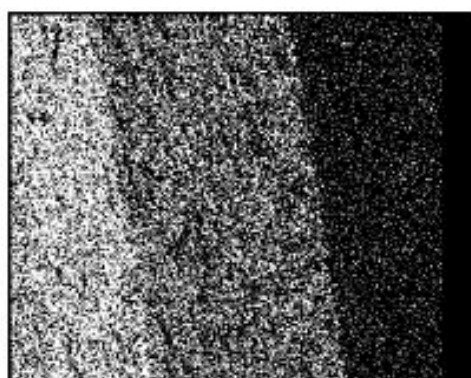
Figure 5.12: SE image and EDS element map of the layers
in a tested standard tube



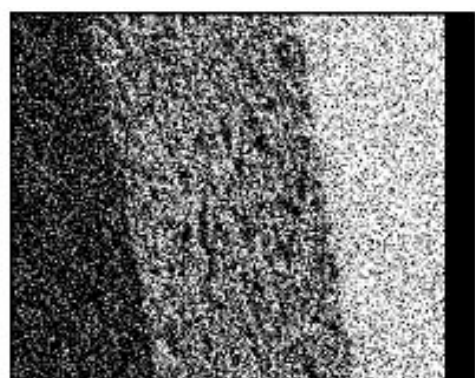
Manganese Ka1



Zirconium La1



Lanthanum La1



Yttrium La1

Figure 5.13: SE image and EDS element map of layers in an untested standard tube

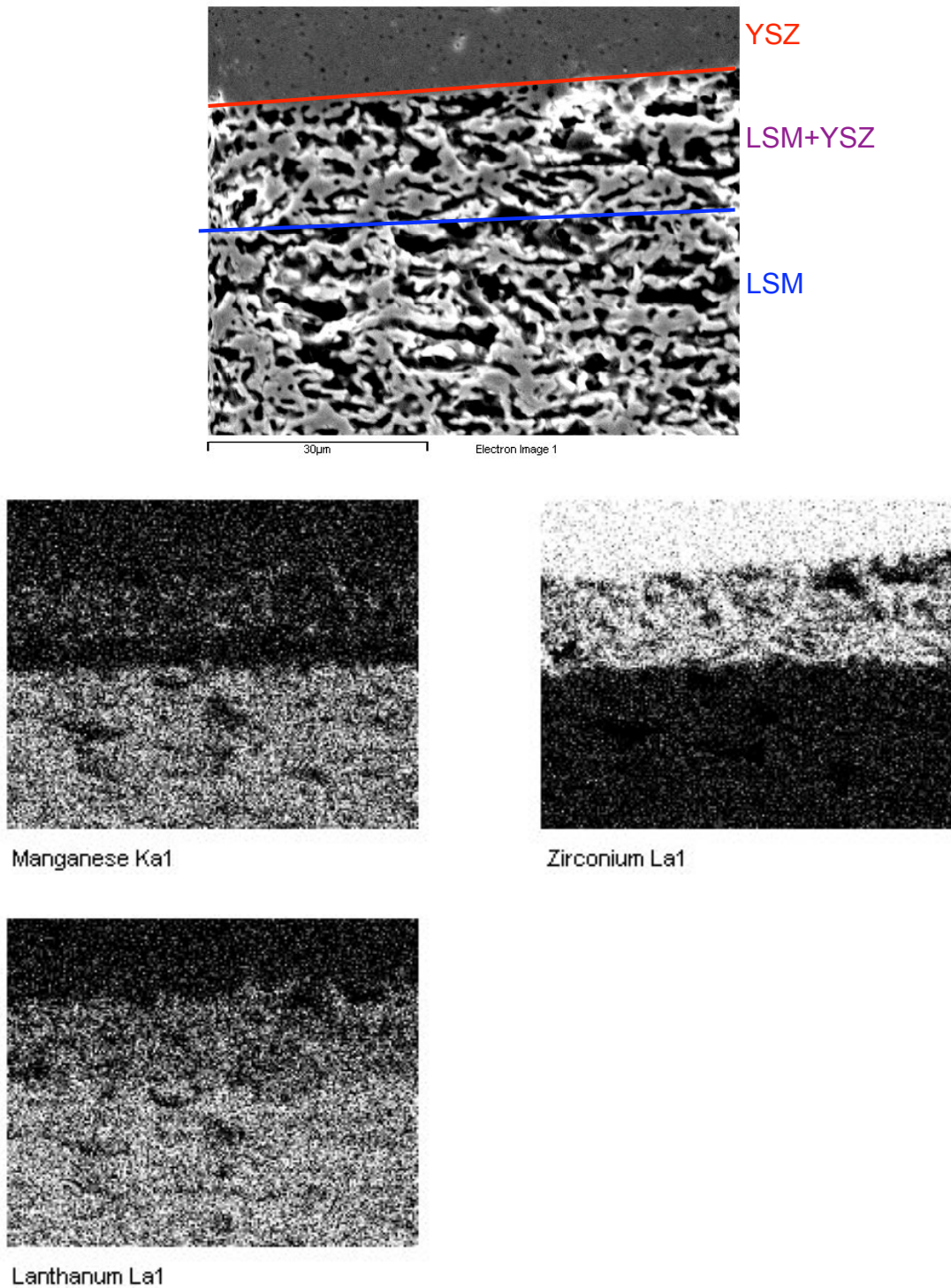


Figure 5.14: SE image and EDS element map of layers in a thin-tape tube

5.4 Dilatometry

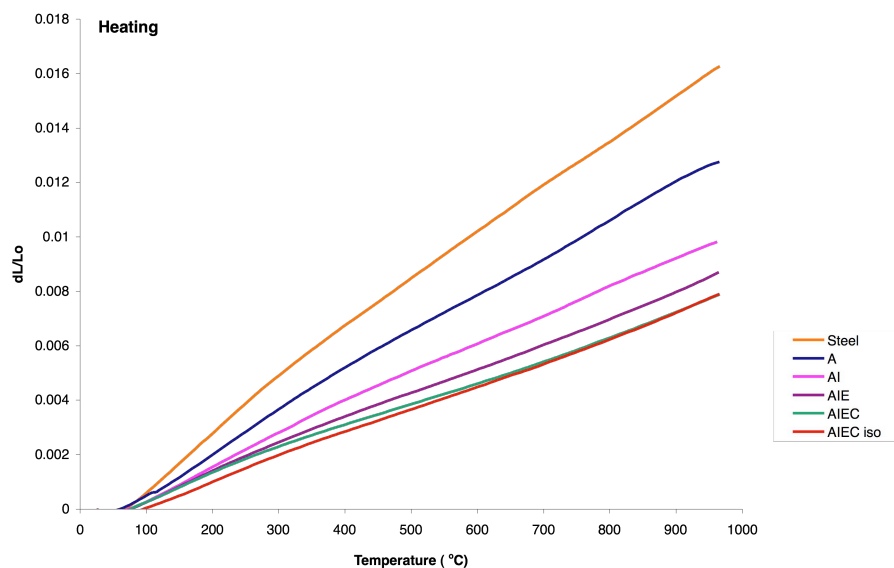
Thermal expansion experiments were performed on samples consisting of various layers of the materials from the electrolysis tubes. The samples were in the shape of 1-cm long sintered tubes, with diameters consistent with the electrolysis tubes. The experiments were performed to investigate the thermal expansions of the various layers: LSM anode current collector (A), LSM+YSZ composite active anode interlayer (I), YSZ electrolyte (E), and NiO+YSZ active cathode (C). The first sample was simply a tube of the LSM anode material, the next sample was the LSM anode with an additional layer of the LSM+YSZ composite interlayer material, and so on building the layers to make a full electrolysis tube. A final sample was tested of the steel support tube. A list of all the samples is tabulated in Table 5.3.

The dilatometry results are shown in Figure 5.15 and Figure 5.16 comparing the thermal expansion of all the tube samples upon heating and cooling respectively. The corresponding linear coefficient of thermal expansion, (α), values are presented in Table 5.4.

The steel tube thermal expansion test was performed to compare the measured α with reported values listed in Table 5.2. The measured values are consistent with reported values for 316 stainless steel. The thermal expansion of the A sample was slightly higher than the reported value for LSM, due to the high porosity in the A sample. As the additional material layers are added to the tube samples the thermal expansion decreases to a final value of around $8 \mu\text{m}/\text{°K}$. The thermal expansion mismatch between the final tube (both AIEC and AIEC-iso samples) and the steel tubes used in the tube assembly set up is approximately $10 \mu\text{m}/\text{°K}$, which is even larger than the suspected mismatch based on reported α values for the various materials. This large mismatch is undoubtedly the cause of the cracking seen in the electrolysis tube samples after testing.

Table 5.3: Dilatometry samples

Sample	Layers	Abbreviation
1	LSM	A
2	LSM, LSM+YSZ	AI
3	LSM, LSM+YSZ, YSZ	AIE
4	LSM, LSM+YSZ, YSZ, NiO+YSZ	AIEC
5	LSM, LSM+YSZ, YSZ, NiO+YSZ, isostatically pressed	AIEC-iso
6	316 stainless steel	steel

**Figure 5.15:** Thermal expansion on heating of tube layer samples obtained from dilatometry.

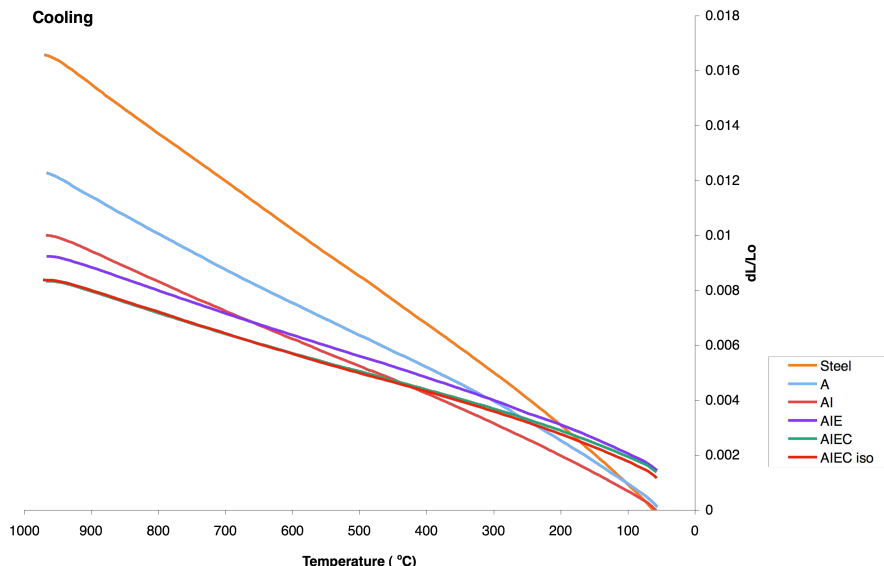


Figure 5.16: Thermal expansion on cooling of tube layer samples obtained from dilatometry.

Table 5.4: Average linear coefficient of thermal expansion (α) between 500 °C and 950 °C for tubular samples upon heating and cooling.

Sample	Heating α ($10^{-6}/K$)	Cooling α (1/K)
A	13.9	13.4
Al	10.8	11.3
AIE	9.25	8.87
AIEC	8.28	7.84
AIEC-iso	8.25	8.15
Steel	17.9	19.0

5.5 Electrolysis Testing

A list of the tube and testing parameters is presented in Table 5.5. The list contains only tubes that were deemed suitable for electrolysis testing, i.e. no visible flaws or cracks prior to sealing onto the test apparatus. All tubes listed in Table 5.5 were fabricated from

standard thickness tapes of cathode A, as described in section 6.2.4. The gas atmosphere in the cathode chamber was altered from that of the pellet cells used in the anode material tests. Argon gas with 5% hydrogen was used in the cathode chamber to assure that the Ni-YSZ cathode used in the tubes remained reduced.

Comparing the current-potential performance of various tubes to each other is difficult in this work. The difficulty lies in the fact that the tube development was continually changing the parameters of the tubes themselves as well as the testing apparatus. Leaks in the test apparatus, seals, and tubes were a constant challenge, as a result many tubes were damaged during testing and no usable data were obtained. An extreme example of such a case is tube T4-1x. This tube appeared intact and the seal onto the test assembly withstood submersion in water to test for leaks. During the first electrolysis test at 680 °C, however, no ocv could be obtained and when potential was applied to the cell there was no current response. The tube was cooled and removed from the test apparatus. Upon inspection, large cracks had developed in the tube. Examination in the SEM revealed a gap between the anode and electrolyte layers in the tube as shown in Figure 5.17. This gap could not be readily detected visually prior to testing, but is the likely cause of the mechanical failure of the tube during testing. Many other tubes, however, were cracked and damaged during testing without such an easily noticeable cause.

Table 5.5: Electrolysis tube and testing parameters.

	Electrolyte thickness (μm)	Sinter rate	Electrical contact cathode side	Electrical contact anode side
T2-1x	100	Fast	Ni wire	Ag paste
T3-1x	100	Fast	Ni wire	Ag paste
T4-1x	100	Fast	Ni wire	Ag paste
T5-3x	175	Slow	Ni mesh	Ag paste
T6-2x	125	Slow	Ni mesh	Ag paste
T7-2x	125	Slow	Ni mesh	Ag paste
T8-3x	200	Slow	Ni mesh	Ag paste
T9-3x	150	Slow	Ni mesh	Ag paste
T10-4x	220	Slow	Ni mesh	Ag paste
T11-3x	150	Slow	Ni mesh	Ag paste
T12-4x*	200	Slow	Ni mesh	Pt wire
LT-3x**	175	Slow	Ni mesh	Ag paste

*alumina test assembly **intermediate length tube

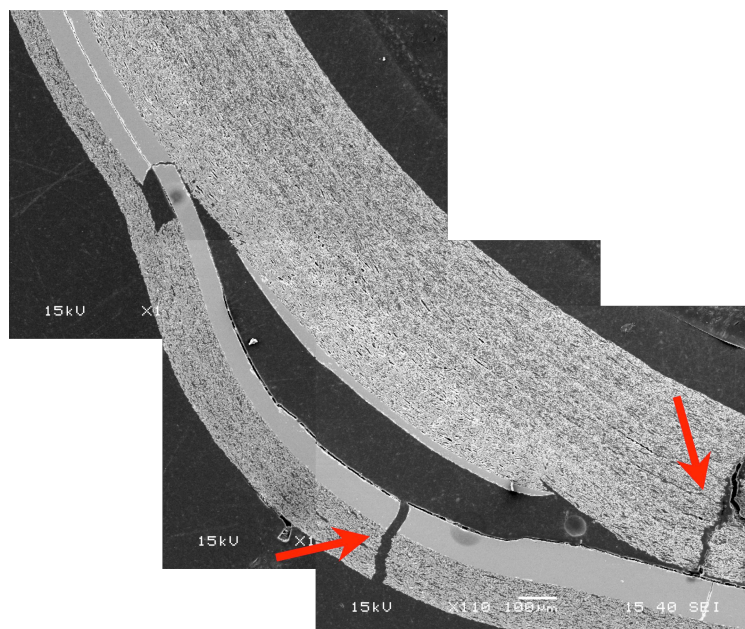


Figure 5.17: Composite SE image of a cross section of Tube T4-1x showing a large gap between the anode and electrolyte layers. The arrows indicate the cracks formed after testing.

5.6 Performance of Electrolysis Tubes

Tube T3-1x was from the early generation of tube development with a sintered electrolyte thickness of 100 μm . The I-V characteristics of T3-1x at various temperatures are presented in Figure 5.18. The plot shows that the performance improves with temperature up to 768 $^{\circ}\text{C}$ and then is worse for 815 $^{\circ}\text{C}$. A crack developed after testing at 768 $^{\circ}\text{C}$ resulting in a leak. H_2 gas was detected in the pO_2 sensor. The performance of the tube decreased as the leaking H_2 reduced the LSM anode material.

Tubes T5-3x and T6-2x were from a group of tubes fabricated from the same batches of green tapes but were made with two different electrolyte thicknesses, 175 μm and 125 μm respectively. Plots of the I-V performance of each of these tubes are presented in Figure 5.19 and Figure 5.20. For both tubes the performance increases with temperature. T5-3x failed at testing temperatures above 820 $^{\circ}\text{C}$ and T6-2x failed above 775 $^{\circ}\text{C}$.

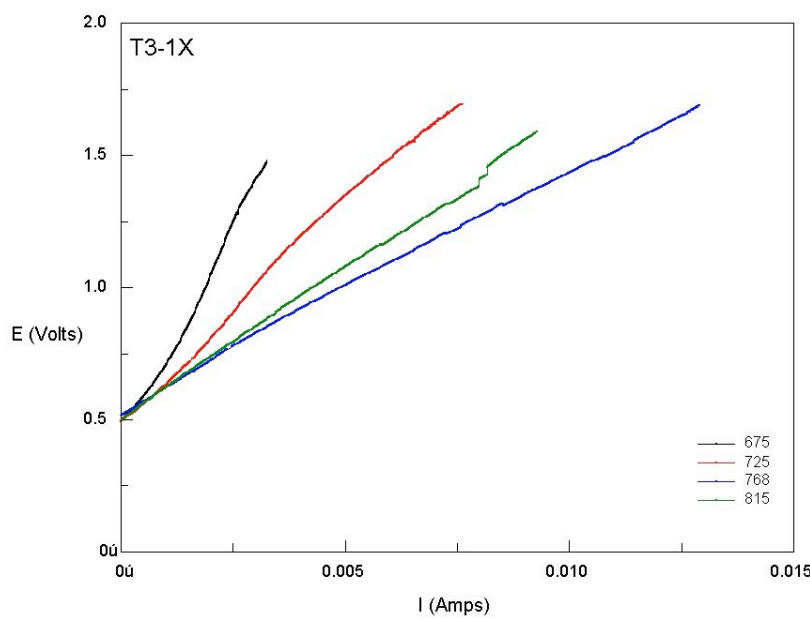


Figure 5.18: I-V performance of tube T3-1x at various operating temperatures. Dry 5% H_2 /Ar vs Ar atmosphere.

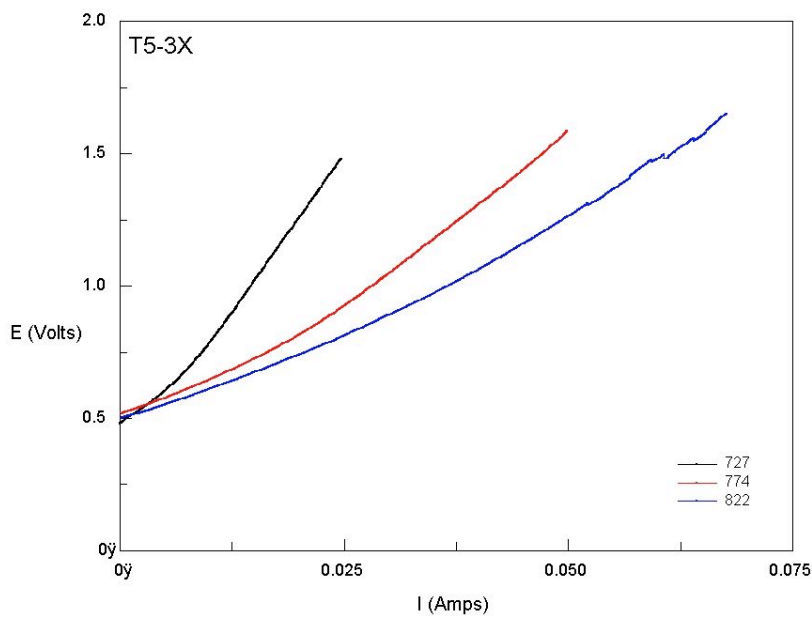


Figure 5.19: I-V performance of tube T5-3x at various operating temperatures. Dry 5%H₂/Ar vs Ar atmosphere

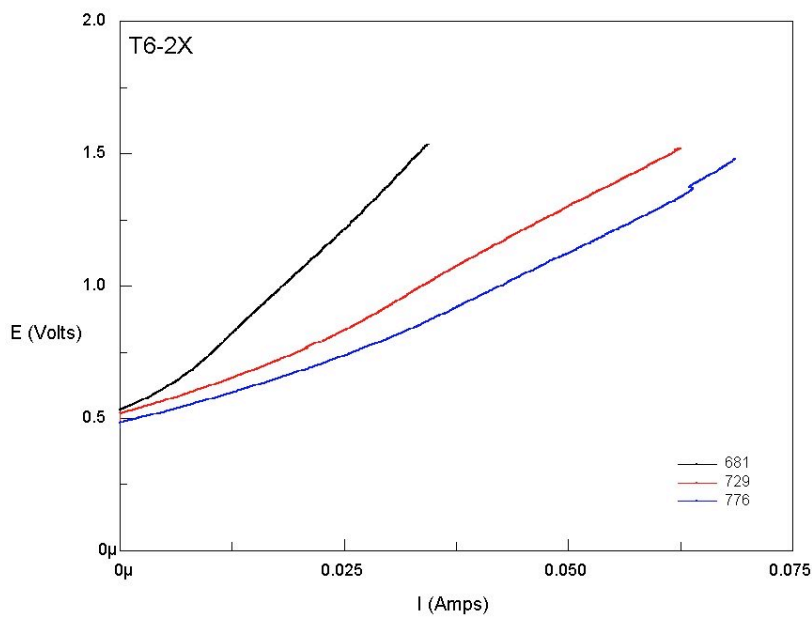


Figure 5.20: I-V performance of tube T6-2x at various operating temperatures. Dry 5%H₂/Ar vs Ar atmosphere

5.7 *Tube Comparison*

Tubes T3-1x, T5-3x and T6-2x are compared at two temperatures in Figure 5.22, and the corresponding area specific resistances of the tubes are presented in Figure 5.23. T3-1x, shown in black, clearly has the worst performance of the three. This tube had the thinnest electrolyte, and correspondingly should have the lowest cell resistance. However, the thin electrolyte was not mechanically robust enough for the temperature cycles involved with sealing and testing. T3-1x had small cracks throughout the cell that were not severe enough to break the tube at these temperatures, but were significantly detrimental to the tube performance. T5-3x and T6-2x were made from the same batch of green tapes, but had different electrolyte thicknesses, 175 μm and 125 μm respectively. T6-2x exhibits the best performance at both temperatures and the electrolyte maintains mechanical strength throughout the testing cycles up to 775 $^{\circ}\text{C}$. A thicker electrolyte is needed for operation above 775 $^{\circ}\text{C}$.

After changing the tube design to a longer length it took several attempts to obtain an intermediate-length tube suitable for testing. The intermediate-length tube LT-3x had the best I-V performance of all tubes due to the larger active area, with a measured ASR of 19 at 663 $^{\circ}\text{C}$ and 13 at 710 $^{\circ}\text{C}$. Tube LT-3x failed during testing at 760 $^{\circ}\text{C}$ so no data was available for higher temperatures. The I-V performance for LT-3x is shown in Figure 5.21.

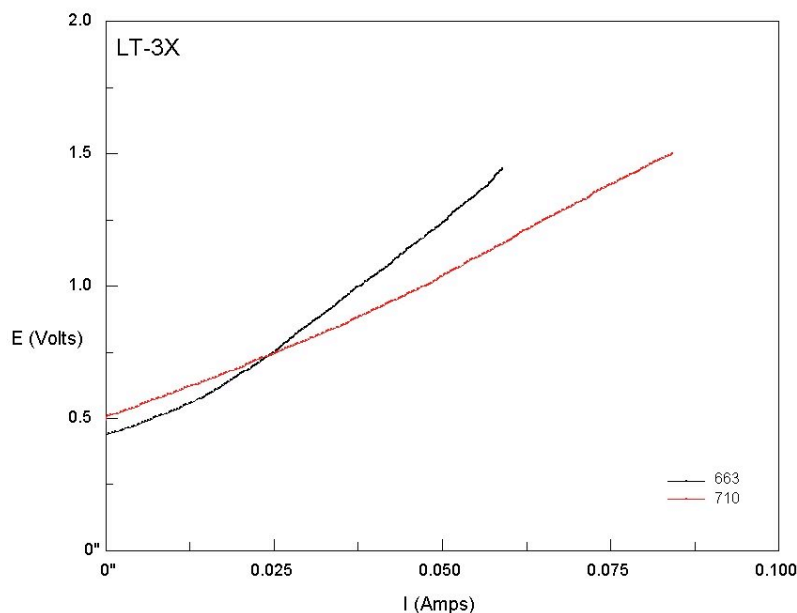


Figure 5.21: I-V performance of tube LT-3x at 663 °C and 710 °C, with ASR of 19 and 13 respectively. Dry 5%H₂/Ar vs Ar atmosphere.

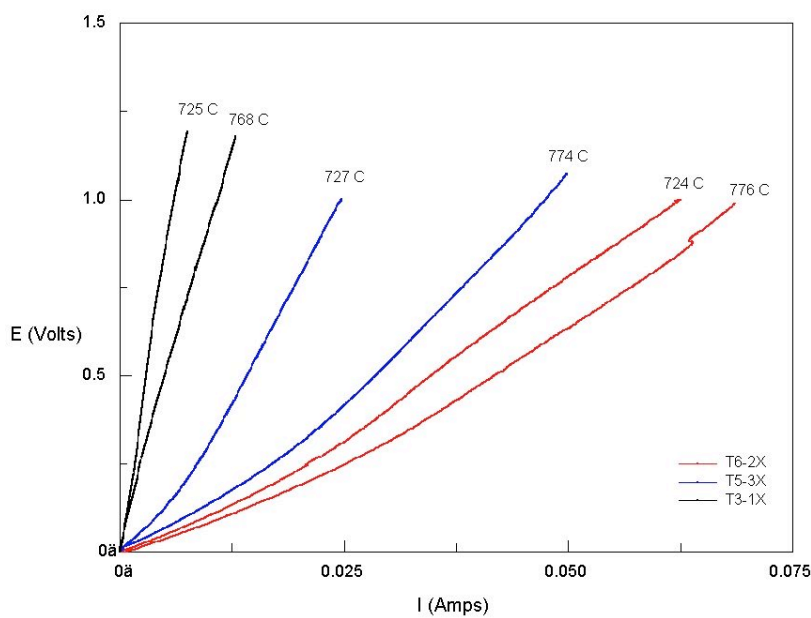


Figure 5.22: Comparison of the I-V performance at 725 °C and 775 °C of three tubes with different electrolyte thicknesses: T3-1x (100 μm), T5-3x, (175 μm), and T6-2x (125 μm). Dry 5%H₂/Ar vs Ar atmosphere.

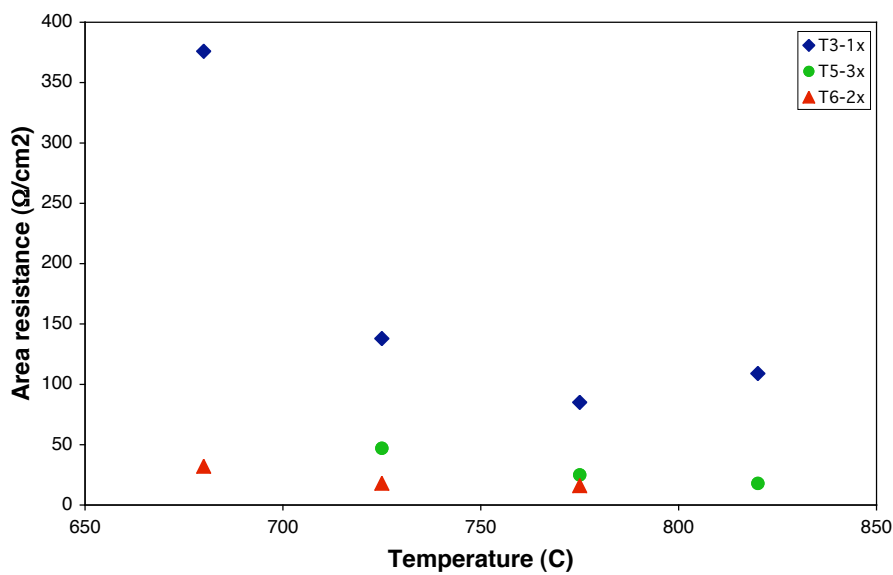


Figure 5.23: Area specific resistance for tubes T3-1x, T5-3x, and T6-2x.

References

- ¹ Singhal, S.C. "Science and technology of solid oxide fuel cells. " *MRS Bulletin*, 25 (2000): 16-21
- ² Siemens AG, 2006,
www.powergeneration.siemens.com/en/fuelcells/technology/tubular/index.cfm
- ³ Jones, F.G.E. "Tape Casting, Co-Firing and Electrical Characterisation of a Novel Design Solid Oxide Fuel Cell: Sofcroll." PhD Thesis, University of St Andrews, 2005.
- ⁴ Virkar, A.V., Chen, J., Tanner, C., and Kim, J.W. "The role of electrode microstructure on activation and concentration polarizations in solid oxide fuel cells. " *Solid State Ionics*. 131 (2000): 189-198
- ⁵ Modensen, M., Primdahl, S., Jorgensen, M.J., and Bagger, C. "Composite electrodes in solid oxide fuel cells and similar solid state devices." *Journal of Electroceramics* 5 (2000): 141-152.

Chapter 6: Discussion

The SEM microstructure studies of the anode materials provided further insight into LSM, LSCo, and LSF materials as electrolysis materials. The LSM anode exhibited many characteristics that make it a good anode material for electrolysis. The LSM layer adhered well to the YSZ electrolyte and exhibited no undesirable reactions between the materials at the interface. The samples also did not exhibit the deteriorations seen by other researchers after electrolysis testing.^[12]

The LSCo materials, both sol-gel prepared and commercial powder, displayed some problems with adherence to the YSZ. The LSCo materials reacted with the YSZ to form a Sr-zirconate reaction product at the interface. Thermal expansion mismatch between LSCo and YSZ was certainly a cause of the poor adherence along with the interfacial reaction between the materials. With a ceria interlayer between the anode and electrolyte the reaction was inhibited. The ceria interlayer also improved the adherence of the LSCo onto the YSZ.

The LSF anode material adhered well to the YSZ substrate with little to no cracking seen in the layers. EDS analysis revealed a new denser phase or possible Zr diffusion into the LSF perovskite structure. The Zr inclusion in the LSF would decrease the electronic conductivity at the interface region. Electrical conduction in LSF occurs primarily through hopping of electrons between adjacent Fe cations. The Zr⁴⁺ cations would act as blocking sites within the lattice.^[3]

The three anode materials of interest in this work all had a similar perovskite structure of the form $L_{1-x}Sr_xMO_3$, where M is Mn, Co, or Fe. The LSM material is well understood as a cathode for SOFCs, but has a lower conductivity that is primarily electronic. The LSCo and LSF materials are both mixed ionic-electronic conductors. The mixed conduction allows for potentially a greater performance as an electrolysis anode for these materials. Both the LSCo and the LSF anodes reacted with the YSZ electrolyte material in the

electrolysers. The LSCo reacts to form La- and Sr-zirconate phases at the interface between the anode and electrolyte. These zirconate phases are insulating and decrease the conductivity and consequently the performance of the electrolyser. The LSF material also reacts with the YSZ electrolyte, but the reaction and its effect on the conductivity and performance are less clear.

When the electrolysis performance is combined with the results from the EDS analysis of the anode materials it is not surprising that overall the LSCo material had the poorest performance of the three. The formation of the insulating zirconate phases at the interface has a detrimental effect on the overall performance of the material. Although LSCo did exhibit the poorest performance it was not orders of magnitude worse than the other two. With tighter control of the microstructure, improved processing and/or the addition of a protective interlayer, LSCo is still a possible anode material for solid oxide electrolysis. The high conductivity of LSCo makes it an attractive anode material despite the problems associated with the interface reactions. Another promising avenue for future investigation would be doping on the Co-site of the LSCo anode in an attempt to improve the TEC mismatch with the YSZ electrolyte for greater long-term stability of the anode. It has been shown in material studies that doping the Co-site with Fe³⁺ can reduce the TEC, although this results in a decrease in the ionic conductivity.⁴

The LSF anode material is a promising alternative to the traditional LSM anode. The performance of the LSF electrolysis cells was higher than both LSM and LSCo, particularly under steam operation, although the EDS analysis of LSF did show an interface reaction between the anode and electrolyte materials. Further work is required to better understand the role of this interface reaction. Alteration of the LSF microstructure and the inclusion of a protective interlayer material to suppress the interface reaction may improve the performance of the LSF anode even further. A logical next step in this work would be to further explore the protective ceria interlayer coating between the YSZ electrolyte and both LSCo and LSF.

The electrolysis cells were fabricated from flexible tapes rolled together to form a closed-end tube. The heat treatment and sintering are performed on complete cells in a single step. The tape case tube design eliminates both the need for interconnect materials as well

as sealing between all layers of the cell. Gas tight sealing is still required, but the closed-end tube design requires only one ceramic to metal join.

The tube design went through many stages of development: examining the cathode composition, sinter rates, tape thickness, electrolyte thickness and tube length. The resulting design incorporated a trade off between performance and mechanical robustness. Cracking due to flaws in the tubes themselves and due to the coefficient of thermal expansion mismatch between the ceramic and metal components of the test apparatus was a continual challenge. Gas-tight sealing proved to be the largest difficulty with the design.

This work has successfully initiated the development of solid oxide electrolyser tubes from tape cast precursor materials. The development steps have resulted in a design, which can be fabricated reliably. The design balances strength and performance, and could easily be adapted for the use of other component materials. Much work is still required to obtain tubes suitable for efficient operation in an electrolyser stack set-up.

No reliable data was acquired from the oxygen sensor for the tube experiments due to equipment failure and experimental design problems. The gas flow through the tube assembly had to be kept low to preserve the ceramic to metal seal. The oxygen sensor was not sensitive enough to accurately measure oxygen partial pressure differences in such a low flow in the relatively short time of the experiments. Therefore no hydrogen production values could be obtained. The purpose of the electrolysis tube experiments was to develop the design and fabrication to obtain a reliable device that could then be further developed in the future to improve the performance. The experimental test set-up will have to be modified to obtain accurate hydrogen production and faradaic efficiency values for future experiments.

The difficulty in testing of the electrolysis tubes was mainly due to the tubes failing mechanically. Thermal expansion mismatch between the ceramic and metal components in the test apparatus contributed greatly to the problems. Using a ferritic stainless steel or high-chromium steel (Crofer 22 APU^[5]) may at least partially alleviate this problem. Crofer 22 APU in particular is attractive as it is designed to oxidize on the outer surface

forming chromium oxide and is compatible to the other ceramic materials used in solid oxide fuel cells and electrolyzers.

A gastight seal is essential for efficient operation of the electrolyser. Although the closed-end tubular design reduces the issues typically encountered with sealing of solid oxide fuel cells and electrolyzers, there is the need for a durable ceramic to metal seal. This seal must endure thermal cycling and pressure differentials in the test apparatus. This seal has been a major source of problems associated with this work. The ceramic slurry seal used in this work was not mechanically strong enough for the application. Even with the addition of the Ceramabond paste for added mechanical strength the seal often failed. SEM observation of a polished cross-section of the seal area of a tube, shown in Figure 6.1, indicated that only the outer part of the YSZ slurry densified: the inner region was porous. A longer dwell time at high temperature might help to alleviate the porosity, but would not help the seal problem significantly as the YSZ slurry material did not sufficiently adhere to and seal with the stainless steel tubing.

The ceramic slurry seal used in this work was not mechanically strong enough for the application. Even with the addition of the Ceramabond paste for added mechanical strength the seal often failed. SEM observation of a polished cross-section of the seal area of a tube, shown in Figure 6.1, indicated that only the outer part of the YSZ slurry densified: the inner region was porous. A longer dwell time at high temperature might help to alleviate the porosity, but would not help the seal problem significantly as the YSZ slurry material did not sufficiently adhere to and seal with the stainless steel tubing.

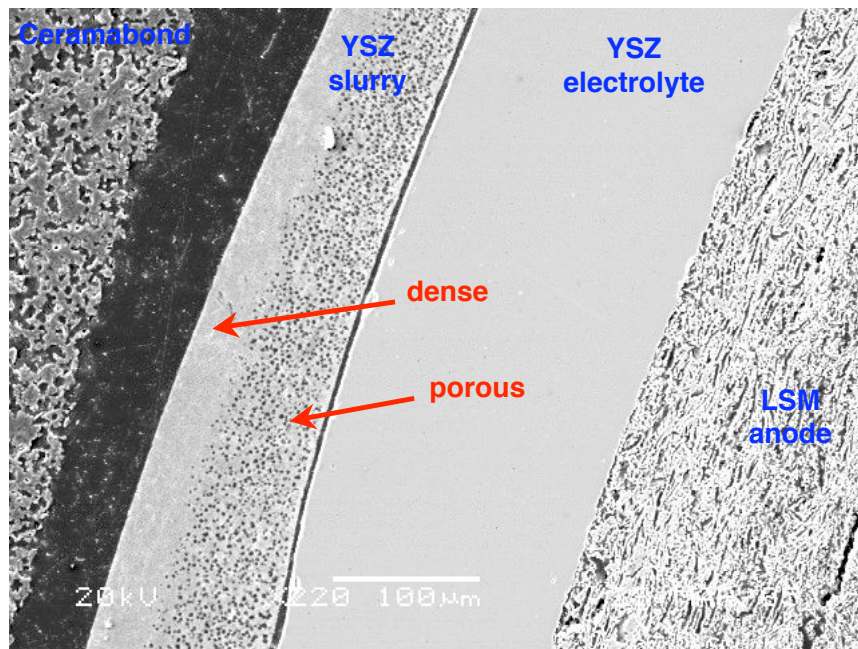


Figure 6.1: SE image of electrolyser tube end with seal materials: ceramabond for mechanical strength, and YSZ slurry for gastight seal. Arrows indicate dense and porous regions of YSZ slurry material.

Other researchers working on a similar problem developed a metal ceramic seal using conventional brazing techniques. Their seal was tested up to 150 psi (10.3 bar) pressure differential and has withstood several rapid temperature cycles with no observed performance degradation.⁶ A similar technique might be possible for application to this work.

Reference

¹ Ralph, J.M., Schoeler, A.C., and Krumpelt, M. "Materials for Lower Temperature Solid Oxide Fuel Cells." *Journal of Material Science* 36 (2001): 1161-72.

² Ralph, J.M., Schoeler, A.C., and Krumpelt, M. "Materials for Lower Temperature Solid Oxide Fuel Cells." *Journal of Material Science* 36 (2001): 1161-72.

³ Simner, S.P., Shelton, J.P., Anderson, M.D., and Stevenson, J.W. "Interaction Between La(Sr)FeO₃ SOFC Cathode and YSZ Electrolyte." *Solid State Ionics* 161 (2003): 11-18.

⁴ Tai, L.W., Nasrallah, M.M, Anderson, H.U, Sparlin, D.M., and Sehlin, S.R. "Structure and Electrical Properties of La_{1-x}Sr_xCo_{1-y}Fe_yO₃. Part 1. The System La_{0.8}Sr_{0.2}Co_{1-y}Fe_yO₃." *Solid State Ionics* 76 (1995): 259-71.

⁵ ThyssenKrupp Steel AG

http://www.thyssenkrupp.com/en/presse/art_detail.html&eid=tk_pnid930, 2007

⁶ Pham, A.Q., E. See, D. Lenz, P. Martin, R.Glass. "High-efficiency steam electrolyser." Proceedings of the US DOE Hydrogen Program Review, 2002.

Chapter 7 Conclusions

The three anode materials of interest in this work all had a similar perovskite structure of the form $L_{1-x}Sr_xMO_3$, where M is Mn, Co, or Fe. The LSM material is well understood as a cathode for SOFCs, but it has a lower conductivity that is primarily electronic. The LSCo and LSF materials are both mixed ionic-electronic conductors. The mixed conduction allows for theoretically a greater performance as an electrolysis anode for these materials. Both the LSCo and the LSF anodes reacted with the YSZ electrolyte material in the electrolyssers. The LSCo reacts to form La- and Sr-zirconate phases at the interface between the anode and electrolyte. These zirconate phases are insulating and decrease the conductivity and, consequently, the performance of the electrolyser. The LSF material also reacts with the YSZ electrolyte, but the reaction and its effect on the conductivity and performance are less clear.

The LSM anode exhibited many characteristics that make it a suitable anode material for electrolysis. The LSM layer adhered well to the YSZ electrolyte and exhibited no undesirable reactions between the materials at the interface. The performance of the LSM anode cells exceeded that of the LSCo anode cells, and in most cases the performance was consistent with that of the LSF anode cells.

Formation of the insulating zirconate phases at the interface in the LSCo cells has a detrimental effect on the overall performance of the cells. The high conductivity of LSCo makes it an attractive anode material in spite of the problems associated with the interface reactions found in these cells. The electrolysis performance was poorest of the three anode materials, but with improvement of the microstructure, and/or the addition of a protective interlayer, LSCo is still a viable anode material for solid oxide electrolysis. The LSCo materials, both sol-gel prepared and commercial powder, displayed some problems with adherence to the YSZ. Thermal expansion mismatch between LSCo and YSZ was certainly a cause of the poor adherence, along with the interfacial reaction between the materials. By employing a ceria interlayer between the anode and electrolyte, the reaction

was inhibited. The ceria interlayer also improved the adherence of the LSCo to the YSZ. Another promising avenue for future investigation would be to examine the use of doping on the Co-site of the LSCo anode in an attempt to improve the TEC mismatch with the YSZ electrolyte to increase long-term stability of the anode.

The LSF anode material is a promising alternative to the traditional LSM anode. The performance of the LSF electrolysis cells exceeded both LSM and LSCo, particularly under steam operation, although the EDS analysis of LSF did show an interface reaction between the anode and electrolyte materials. Further work is required to better understand the role of this interface reaction. Alteration of the LSF microstructure and the inclusion of a protective interlayer material to suppress the interface reaction may improve the performance of the LSF anode even further. The LSF anode material adhered well to the YSZ substrate, with little to no cracking seen in the layers. EDS analysis revealed a new, denser phase or possible Zr diffusion into the LSF perovskite structure. A logical next step in this work would be to further explore the protective ceria interlayer coating between the YSZ electrolyte and both LSCo and LSF.

The development of solid oxide electrolyser tubes from tape cast precursor materials resulted in a solid design, which can be fabricated reliably, and balances strength with performance. The design used LSM anode, YSZ electrolyte, and Ni-YSZ cathode materials but could easily be adapted for the use of other component materials in the future. Proper sintering rates, cathode tape formulation, tube length, tape thickness, and electrolyte thickness were factors explored in this work to improve the electrolyser tubes.

Altering the component materials would be the next step in this work. A cathode that does not require a reducing atmosphere as does the Ni-YSZ cermet is necessary for use in an efficient electrolyser system. Alternate anode materials with mixed ionic-electronic conduction could improve the performance of the tubes. Anodes based on the $\text{La}_{0.8}\text{Sr}_{0.2}\text{CoO}_3$ (LSCo), $\text{La}_{0.8}\text{Sr}_{0.2}\text{FeO}_3$ (LSF), and $\text{La}_{1-x}\text{Sr}_x\text{Co}_{1-y}\text{Fe}_y\text{O}_3$ (LSCF) perovskite systems are likely future choices, but would require a protective interlayer material to prevent interface reactions. An interlayer material would not alter the fabrication steps of the electrolyser tubes greatly, apart from adding one additional tape layer. The use of new component materials would require that some of the development steps be repeated to

accommodate the properties of the new materials. Changing the steel alloy used in the test assembly would be another improvement in the overall electrolyser design. Ferritic stainless steels and high-chromium steels (Crofer) may offer improved conduction without sacrificing performance due to corrosion.

A gastight metal-ceramic seal is essential for efficient operation of the electrolyser. A brazed metal-ceramic seal or a gas-tight glass seal that is stable under operating conditions must be developed because many of the problems associated with electrolysis testing were a direct result of the poor sealing. Improved sealing would enhance the system stability, increase the reliability of all measurements, and lead to further improvements in the electrolyser tubes. A reliable seal on the electrolyser tubes is necessary for accurate electrolysis measurements, as well as pO₂ measurements, to determine the faradaic efficiency of the electrolyser tubes.

Chapter 8: Future Work

Although progress has been made in developing the tape cast electrolyser tubes there are several areas that need to be addressed for future work. A different cathode material for the electrolysis tubes is an obvious alteration to explore in the future. The Ni-YSZ cermet is not an ideal choice and was only used because it is a well understood material in the fuel cell system. A cathode which did not require a reducing atmosphere to maintain good electrical conduction, as the Ni-YSZ cermet does, would be a major improvement. New anode materials with mixed ionic-electronic conduction would be an improvement as well. Anodes based on the $\text{La}_{0.8}\text{Sr}_{0.2}\text{CoO}_3$ (LSCo), $\text{La}_{0.8}\text{Sr}_{0.2}\text{FeO}_3$ (LSF), and $\text{La}_{1-x}\text{Sr}_x\text{Co}_{1-y}\text{Fe}_y\text{O}_3$ (LSCF) perovskite systems are possible choices. With new component materials some of the development steps would have to be repeated to accommodate the properties (shrinkage, TEC, etc) of the new materials. New anode materials would likely need the addition of an interlayer between the electrolyte and anode materials to prevent interface reactions.

Another improvement in the design could be made by changing the steel alloy used in the test assembly. Stainless steel 316 is not an ideal choice for this application; however it is available in many forms including the gauge of tubing required for the test apparatus. Other steel alloys including ferritic stainless steels and high-chromium steels (Crofer 22 APU) may offer improved properties, but these alloys are more expensive and difficult to obtain in the proper form.

The closed-end tubular design reduces the issues typically encountered with sealing of solid oxide fuel cells and electrolyzers. However, there is the need for a robust ceramic to metal seal on one end able to withstand temperature cycling and pressure differentials in the test apparatus. A gastight seal is essential for efficient operation of the electrolyser. This seal has been a major source of problems associated with this work. Glass seals or a ceramic to metal join by brazing are the most likely solutions to the sealing problem and should be explored.

The testing of the electrolyser performance requires improvement. Many of the problems associated with electrolysis testing were a direct result of the poor seals. Proper sealing would make a more stable system; this would increase the reliability of all measurements and lead to further improvements in the electrolyser tubes. With a reliable seal on the electrolyser tubes the gas pressure could be increased allowing for higher accuracy in electrolysis measurements as well as pO₂ measurements to determine the faradaic efficiency of the electrolyser tubes. For faradaic efficiency and hydrogen production measurements it would be a major improvement to have a hydrogen detector to directly measure the hydrogen production values rather than relying on calculating the production from pO₂ measurements. Such a detector was not available for this work, but would be beneficial for future use.